communications earth & environment

Article

https://doi.org/10.1038/s43247-024-01930-6

Widespread outdoor exposure to uncompensable heat stress with warming

Check for updates

Yuanchao Fan [1,2] ✉ & Kaighin A. McColl [2,3] ✉

Previous studies projected an increasing risk of uncompensable heat stress indoors in a warming climate. However, little is known about the timing and extent of this risk for those engaged in essential outdoor activities, such as water collection and farming. Here, we employ a physically-based human energy balance model, which considers radiative, wind, and key physiological effects, to project global risk of uncompensable heat stress outdoors using bias-corrected climate model outputs. Focusing on farmers (approximately 850 million people), our model shows that an ensemble median 2.8% (15%) would be subject to several days of uncompensable heat stress yearly at 2 (4) °C of warming relative to preindustrial. Focusing on people who must walk outside to access drinking water (approximately 700 million people), 3.4% (23%) would be impacted at 2 (4) °C of warming. Outdoor work would need to be completed at night or in the early morning during these events.

Global warming is expected to amplify heatwaves and associated heat stress in a variety of different ways[1,2]. Heat stress occurs when the combined effects of temperature, humidity and other climate variables overwhelm the body's thermoregulation[3,4]. Recent studies highlight the role of humidity in heat stress and associated impacts on human mortality and morbidity and labor productivity under multiple warming scenarios[5–9]. A particular concern is the occurrence of 'uncompensable heat stress', in which the body is unable to achieve sufficient heat dissipation (via sensible, latent, or radiative pathways) to maintain stable core temperatures[10–12].

A growing number of empirical relationships[5,10,11,13,14] and diagnostic indices (e.g., wet-bulb globe temperature (WBGT)[15–18]) are used to link observed climatic conditions or index values from instruments to epidemiologic data on heat illness[3,4]. However, empirical methods like the WBGT inadequately mimic the human body's response to heat[15,19], particularly at higher heat stress levels[20,21] and in conditions that differ from those in which they were calibrated[4]. Sherwood[22] noted that "empirical measures like WBGT implicitly involve physiological adaptations, so applying them to significantly warmer global climates would require extrapolation way outside their range of calibration, potentially invalidating them." Several studies[11,12] have also cautioned that empirical thresholds determined from a limited number of subjects may not be representative of other regional or global populations, due to the influence of acclimatization.

These limitations of empirical methods motivate the use of physically-based models. In a pioneering study, Sherwood and Huber[1] used simple thermodynamics to propose an "adaptability limit"—that is, the upper tolerance limit of heat stress for a fit, unclothed, fully-hydrated, acclimated, resting person completely sheltered from solar radiation and subjected to gale-force winds—of 35 °C for wet-bulb temperature (T_W). This limit has since been widely adopted[6–8,23], but its simplicity comes with important limitations[10,12,24]. These limitations include ignoring biological limits on sweating rates[10,25]; ignoring limits to evaporative efficiency due to finite wind speeds[19]; ignoring metabolic heat generated by the body[24]; and ignoring the heat load from solar and longwave radiation[24,26–28]. Recent studies have demonstrated uncompensable heat stress occurring at T_W much lower than 35 °C due to effects of increased metabolic heat[24], finite wind speeds[10,24] and limited sweating capacity[10–12]. However, these studies all assumed complete darkness (what they called "shade" corresponded to zero solar radiation) whether indoors or outdoors. Although humans can partially avoid direct sunlight by sheltering indoors or in the shade, a proportion of solar radiation, in the form of diffuse radiation and transmitted and reflected direct radiation, will inevitably reach indoors (~20–80% transmitted through a glass window)[27] or pass through shading objects (~30–70% under plastic shading nets[29,30] and 5–27% under tree canopies in the summer[31,32]) as long as they are not in complete darkness. A recent study[33] examined an outdoor "sun" scenario using approximated midday radiation under partly cloudy conditions, assuming radiant temperature was always 15 °C higher than air temperature (T_a). This assumption ignores diurnal weather variability and the plasticity in human behavioral responses to heat (see more details in the "Discussion"). To accurately assess the impact of solar radiation on uncompensable heat stress, it is crucial to use dynamic radiation inputs and constrain uncertainties in radiation exposure due to human behavioral modifications. One approach is to calculate the diurnally varying and daytime average impact of heat stress on specific subpopulations who must conduct essential daily activities outdoors and cannot seek shelter

[1]Shenzhen Key Laboratory of Ecological Remediation and Carbon Sequestration, Institute of Environment and Ecology, Tsinghua Shenzhen International Graduate School, Tsinghua University, Shenzhen, China. [2]Department of Earth and Planetary Sciences, Harvard University, Cambridge, MA, USA. [3]School of Engineering and Applied Sciences, Harvard University, Cambridge, MA, USA. ✉e-mail: yuanchao.fan@sz.tsinghua.edu.cn; kmccoll@seas.harvard.edu

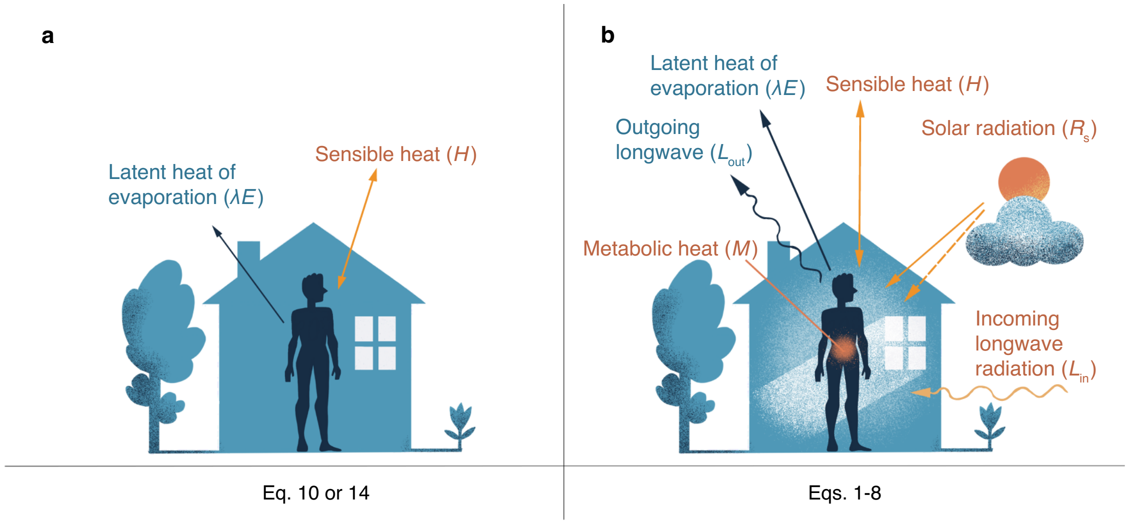

Fig. 1 | Schematic illustrating the human energy balance model with different assumptions. a Assumptions embedded in previous studies using moist heat stress metrics that focus on latent (λE) and sensible (H) heat fluxes (neglecting all radiation and metabolic activity). **b** Assumptions in this study based on an intermediate complexity human energy balance model considering λE, H, and additionally solar radiation (R_s), incoming (L_{in}) and outgoing (L_{out}) longwave radiation, and metabolic heat (M) for a resting person (see the "Methods" section).

indefinitely: for example, there are ~850 million agricultural workers who work long hours under direct sunlight[34,35], and more than 700 million people in low-income and middle-income countries who must walk more than 30 min outside per day just to access water[36,37]. What effect does the inclusion of varying radiation have on the prevalence of uncompensable heat stress among these susceptible populations? And how does their inclusion impact heat stress projections this century? The urgency of addressing these research questions is clear, as researchers have advocated for improved measures of heat stress from direct sunlight and the optimization of public shade infrastructure as a strategy to adapt to hotter urban climates[38].

To answer these questions, we take a physically-based energy balance approach, informed by energy balance modeling in the fields of climatology[39] and thermophysiology[4] to calculate heat exchange between a person and their environment (Fig. 1). The rate of heat storage in the body, denoted as G in Eq. (1), is used to identify uncompensable heat stress. When G is positive ($G > 0$), it indicates a net heat gain (uncompensable heat) that results in an increase in the body's core temperature. Noting the current gap between the climate and health research communities and limited integration of human heat stress models into climate projections[33,40] due to model complexity and computational costs[4], our model (Eqs. (1)–(8) parsimoniously extends the implicit model of Sherwood and Huber[1] (Eq. (14)) to include the effects of radiation, wind, and basic human physiology in addition to temperature and humidity while remaining much simpler than existing human thermophysiological models[33,41–43] (Fig. 1 and the "Methods" section).

We validate the model against the PSU-HEAT experimental data from Wolf et al.[25] in a similar way to the validation conducted in recent studies[33,44] (see the "Methods" subsection "Model validation and cross-comparison"). Figure 2 demonstrates that our model (Eqs. (1)–(8) is accurate in predicting the uncompensable heat stress threshold ($G = 0$) for multiple human subjects involved in the MinAct and LightAmb trials with different levels of metabolic heat, across a range of critical conditions represented by twelve combinations of air temperature and vapor pressure. The model is then used to calculate G using bias- and variance-corrected three-hourly near-surface climate variables of 12 climate models for the 21st century from the Coupled Model Intercomparison Project Phase 6 (CMIP6)[45] (see Supplementary Methods 1 and 3 for details on model data and bias correction). We use daytime mean G (G^{day}) to estimate the impact of uncompensable heat stress ($G^{day} > 0$ W m^{-2}), focusing on the subpopulations of 850 million rural agricultural workers[35] and 700 million people who must walk outside to access drinking water[37] (see Supplementary Method 2 "Population distribution data"). A grid cell is considered impacted by uncompensable heat stress when its G^{day} exceeds zero for at least one day per year. We conduct a warming of emergence (WoE) analysis at each grid cell (similar to the temperature of emergence concept[2]) to estimate the future risk of

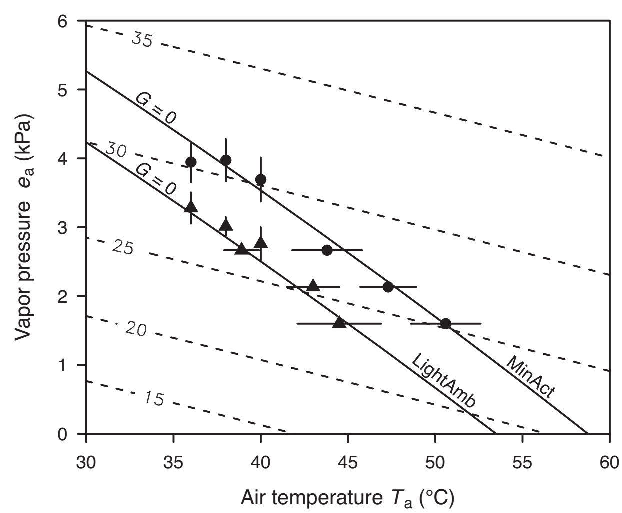

Fig. 2 | Model validation using chamber experimental data. The solid points and triangles represent two sets of experiments from the PSU-HEAT project[25]: MinAct (mean $M = 83$ W m^{-2}) and LightAmb (mean $M = 133$ W m^{-2}), respectively. Each experiment includes six trials with either (1) constant T_a and progressively increasing vapor pressure (e_a) or (2) constant e_a and increasing T_a until the core temperature (T_c) inflection point was observed. These twelve combinations of critical T_a and e_a and two levels of metabolic heat (83 and 133 W m^{-2}) are used as inputs to our energy balance model ((Eqs. (1)–(8), model parameters are summarized in Supplementary Table 1), which accurately predicts G around zero for all experiments. The solid lines denote the $G = 0$ isopleths, indicating the T_c inflection point and the uncompensable heat stress threshold from our model for each level of M in the MinAct and LightAmb experiments. Each point or triangle symbol represents the mean of multiple human subjects, and the error bar represents the standard deviation (vertical bars for fixed T_a trials, horizontal bars for fixed e_a trials). Dashed contours are the isopleths of wet-bulb temperature. See Supplementary Fig. 9 for relative humidity (RH) on the Y-axis. More details are provided in the "Methods" subsection "Model validation and cross-comparison".

Table 1 | Modeling scenarios used in this study

Scenario	Radiation ($R_{in} + L_{in}$, W m^{-2})	Metabolic heat (M, W m^{-2})	Maximum sweat rate (λE_{max}, W m^{-2})
Sun	Modeled L_{in} and sun scenario for R_{in} (Eq. (3))	176 (moderate work)	500 (400) for acclimated (non-acclimated) persons
Shade	Modeled L_{in} and shade scenario for R_{in} (Eq. (3))	176	500 (400)
Dark	Modeled L_{in} ($R_{in} = 0$)	176	500 (400)
Dark*	Modeled L_{in} ($R_{in} = 0$)	176	No limit
Dark**	Modeled L_{in} ($R_{in} = 0$)	59 (complete rest)	No limit

The outdoor sun and shade scenarios are the key contribution of this study, while the dark scenarios are used to compare with prior studies (see the "Discussion" section). In all scenarios, modeled wind speed (U) is used.
R_{in} and L_{in} denote input shortwave and longwave radiation, respectively. See the "Methods" section and Supplementary Table 1 for definitions of all terms.

uncompensable heat stress. We also analyze the frequency and duration of uncompensable heat stress events using both G^{day} and 3-h G. We consider outdoor sun and shade scenarios with varying degrees of radiation exposure relevant to people collecting water or working on farms (see the "Methods" subsection "Heat stress scenario"). We also consider additional scenarios in which metabolic heat and sweating limits are varied (dark, dark*, dark**, Table 1). These scenarios correspond to recent studies that have built on thermophysiological theories but excluded solar radiation[1,10–12,24]. Finally, we normalize the projected impacts by global warming amounts[46] (see the "Methods" subsection "Normalizing by global warming amount").

Results

A physically-based measure of heat stress, G

Comparison of G under five scenarios with the conventional metric T_W and its equivalent energy flux (G_{TW}; Eq. (10) or (14) in the "Methods" section) reveals that the T_W metric with the 35 °C threshold systematically underestimates the future risk of uncompensable heat stress (Fig. 3). This is consistent with recent studies[10,33] that have identified critical wet-bulb temperature thresholds considerably lower than 35 °C. We quantify the individual effects of finite wind speed, metabolic heat, sweating limits, and solar radiation on body energy balance that are ignored by the T_W metric. The effect of finite wind speed is illustrated by the difference between G^{day} (dark**) and $T_W{}^{day}$ ($G_{TW}{}^{day}$; the superscript 'day' indicates daytime mean) (Fig. 3 and Supplementary Fig. 10f). A large proportion of the underestimation of body heat storage rate by the T_W metric is due to its assumption of gale-force winds[1], whereas our data show that heat stress is often associated with finite wind speeds (Supplementary Fig. 22d). The effect of increased metabolic heat required for outdoor activities in the dark* scenario, which is similar to ref. 24, results in a constant increase relative to the dark** scenario with resting metabolic heat (Supplementary Fig. 10e). The effect of imposing a limit to sweating capacity ($\lambda E_{max} = 500$ W m^{-2}, Eq. (8)) on G increases with increased warming (Fig. 3). Supplementary Fig. 10d shows that the heat gains due to the sweating limit are most pronounced in Northern Africa, the Persian Gulf, and Central Australia where wind speeds are high and relative humidities are low during the hottest days (Supplementary Figs. 19–21), which result in an extremely high free evaporative flux (λE_o, Eq. (7)) exceeding λE_{max}. However, among the hottest 1% of land grid cells ranked by annual maximum G^{day} (dark), many are located in tropical humid regions (Supplementary Fig. 10a) where wind speeds are low and relative humidities are high (Supplementary Fig. 21) and λE_o rarely exceeds λE_{max} (Supplementary Fig. 10d); thus, the contribution of heat gains due to limited sweating to the overall heat stress in the dark scenario is relatively small (Fig. 3). This is consistent with another study[33] that showed pronounced effects of sweating limits in hot and dry conditions but minimal effects in high humidities.

When the effects of solar radiation are included, the average intensity of heat stress (annual maximum G^{day}) under the sun (shade) scenario for the hottest 1% of land grid cells is roughly 155 (80) W m^{-2}, or 2(1) °C T_W-equivalent, higher than the estimates under the dark scenario (Fig. 3; a nonlinear conversion between the energy flux on the left Y-axis and T_W on the right Y-axis is obtained using Eq. (10) or Eq. (14)). We conservatively use daytime averaged, sun-angle corrected solar radiation (Eq. (3) for the sun

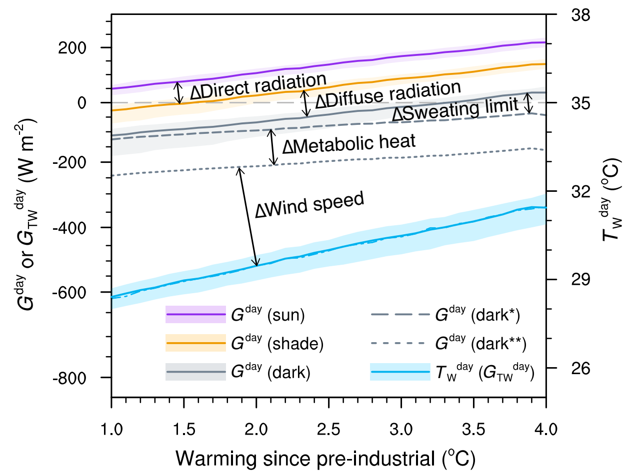

Fig. 3 | Area-weighted average of annual maximum G^{day} and $T_W{}^{day}$ ($G_{TW}{}^{day}$) of the hottest 1% of land grid cells as a function of global warming amounts. For wet-bulb temperature, the left Y-axis shows the value of $G_{TW}{}^{day}$ (blue dot-dashed line) corresponding to each value of $T_W{}^{day}$ on the right Y-axis; slight differences are due to the temporal and spatial variations in wind speed considered by $G_{TW}{}^{day}$ but not considered by the $T_W{}^{day}$ metric (instantaneous wind speeds concurrent with $T_W{}^{day}$ are used to compute $G_{TW}{}^{day}$ using Eq. (14)). The difference between $T_W{}^{day}$ ($G_{TW}{}^{day}$) and G^{day} (dark**) indicates the underestimation of body heat storage rate by the T_W metric mainly due to its assumption of gale-force winds. The other differences, G^{day} (dark*)−G^{day} (dark**), G^{day} (dark*)−G^{day} (dark), G^{day} (shade)−G^{day} (dark), and G^{day} (sun)−G^{day} (shade) indicate the effect of increased metabolic heat for outdoor activities, the effect of imposing the sweating limit, the effect of diffuse radiation under shade, and the effect of additional direct beam radiation, respectively. Details on the sun, shade, and three dark scenarios are summarized in Table 1. All solid lines denote the ensemble median, and the shaded areas indicate the 25th–75th percentile interval across 12 CMIP6 models.

scenario) to accommodate variability in radiation exposure during outdoor activities, which results in much lower radiative heat load (mostly <150 W m^{-2}, Supplementary Fig. 10c) than using daily maximum or mid-day radiation under the same weather condition (Supplementary Fig. 16d). Nevertheless, the daytime average radiation, under full sun or shade, substantially increases the prevalence, frequency, and duration of uncompensable heat stress (see next sections). Our model demonstrates why even relatively low daytime average radiation has a strong effect. As wind speeds decline, there is a nonlinear decrease in the convective heat transfer coefficient (h_c) and evaporative cooling flux (λE, Eq. (7)), thereby magnifying the risk of G exceeding zero when R_n is positive (Eqs. (1) and (2)). Thus, when combined with the effects of low wind speeds in the tropics, the absorbed radiation plays a major role in exceeding the uncompensable heat stress threshold in the hottest parts of the world (Fig. 3).

Emergence of uncompensable heat stress

Our WoE analysis shows that uncompensable heat stress (at least one day per year with $G^{day} > 0$ W m^{-2}) is projected to emerge in some limited areas in

Fig. 4 | Warming of emergence (WoE) for uncompensable heat stress. WoE is defined as the lowest global warming amount (relative to 1850–1900) for which uncompensable heat stress emerges ($G^{day} > 0$ W m^{-2}) at each grid cell according to the CMIP6 ensemble median G^{day} (see the "Methods" subsection "Normalizing by global warming amount"). WoE is estimated for the dark (**a**), shade (**b**), and sun (**c**) scenarios (defined in Table 1). Uncolored land areas are where fewer than six of the twelve models project a WoE <4 °C by 2099. WoE maps for individual models are shown in Supplementary Figs. 17 and 18. The background grayscale population map in **a** is for illustration purposes: by overlapping the WoE with the distribution of specific populations engaged in outdoor activities, such as those who perform agricultural work, we can determine the impact of uncompensable heat stress on these populations (see Fig. 5 and color population maps in Supplementary Fig. 2).

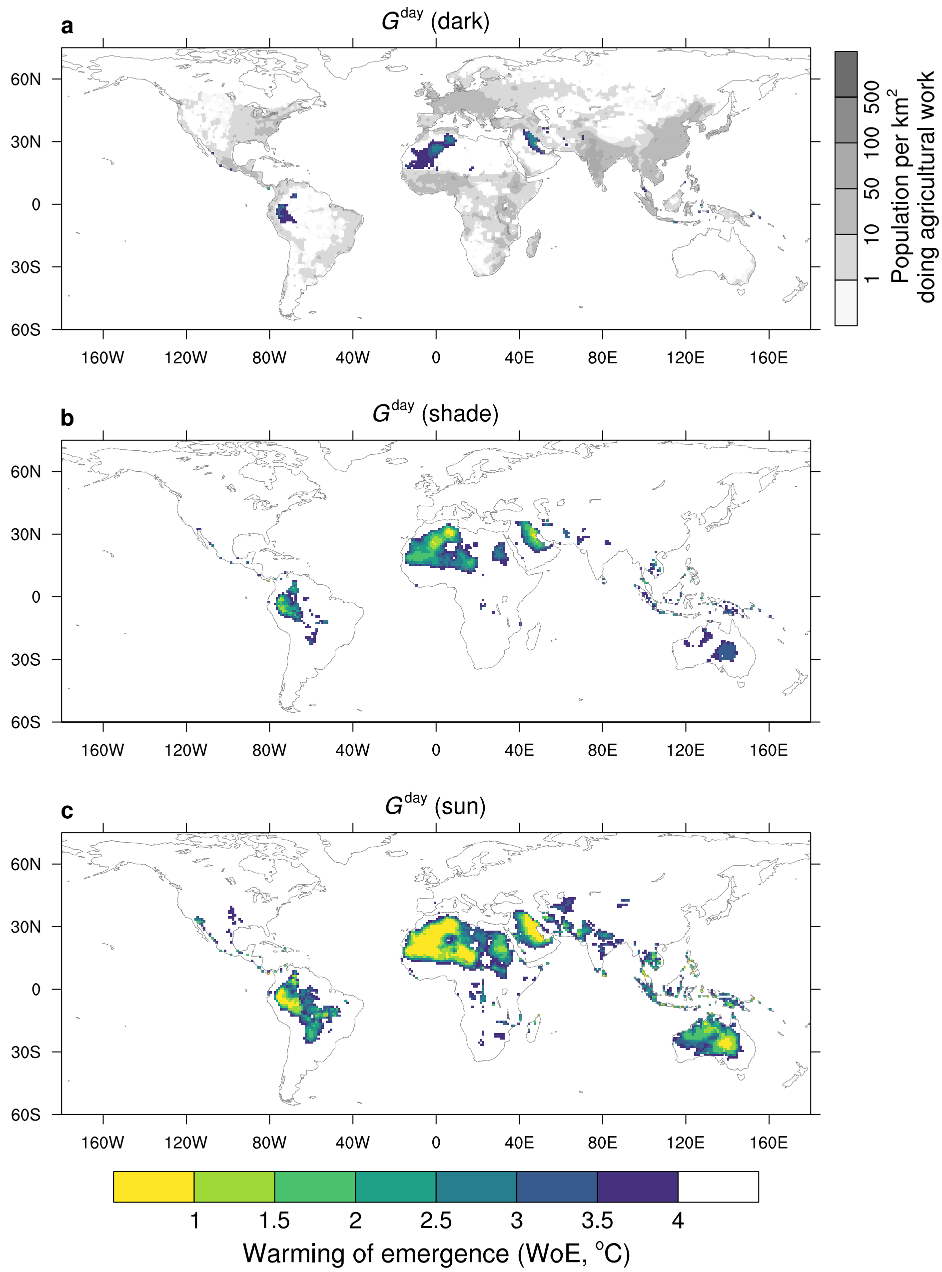

the Amazon, Northern Africa, and the Persian Gulf when global warming surpasses 2.5 °C and approaches 4 °C under the dark scenario (Fig. 4a). When considering diffuse solar radiation under shade (Fig. 4b and Supplementary Fig. 17 for individual models), the projected uncompensable heat stress emerges earlier in the above locations (<2 °C) and expands to more areas in the Sahel, Northern India/Pakistan, Southeast Asia, and Australia with more than 2–3 °C of warming. When the effects of full solar radiation are included, the risk of uncompensable heat stress is projected to expand to more regions of South America, Northern and Central Africa, India, Southeast Asia, Australia, and the Southern United States, at or after 1.5 °C of warming (Fig. 4c and Supplementary Fig. 18 for individual models). Regions such as Northern Africa, the Arabian Peninsula, and Central Australia are subject to the strongest solar radiation effects (Supplementary Fig. 10c), resulting in many of these regions already experiencing projected uncompensable heat (WoE <1 °C) under the sun scenario. But, the Sahara region and Central Australia have a very limited population engaged in water collection or farming (Supplementary Fig. 2), and thus the impact on outdoor activities is limited in these regions. Regions across tropical humid areas are subject to slightly weaker solar radiation effects but overall high G^{day} (Supplementary Fig. 10b, c, f) due to low wind speeds in these regions (Supplementary Fig. 19h). The tropical regions also have a larger fraction of populations engaged in outdoor activities such as drinking water collection or farming (see Supplementary Fig. 2), making them especially vulnerable to additional heat stress from solar radiation (discussed in further detail in the next section).

Impact of uncompensable heat on outdoor activities

While the most similar previous studies have largely ignored the effects of radiation[10–12,24,47], those engaged in outdoor water collection or farming do not necessarily have the luxury of sheltering indoors for extended periods. What is the impact of solar radiation on uncompensable heat stress in these communities? Fig. 5a, c shows that under the sun (shade) scenario, around 480 (100) million hectares (Mha), or 7% (1.5%) of the land area masked by water access data or agricultural population data (Supplementary Fig. 2), is projected to be at risk of uncompensable heat stress ($G^{day} > 0$ W m^{-2}) at 2 °C of warming. The impacted areas increase rapidly with higher global

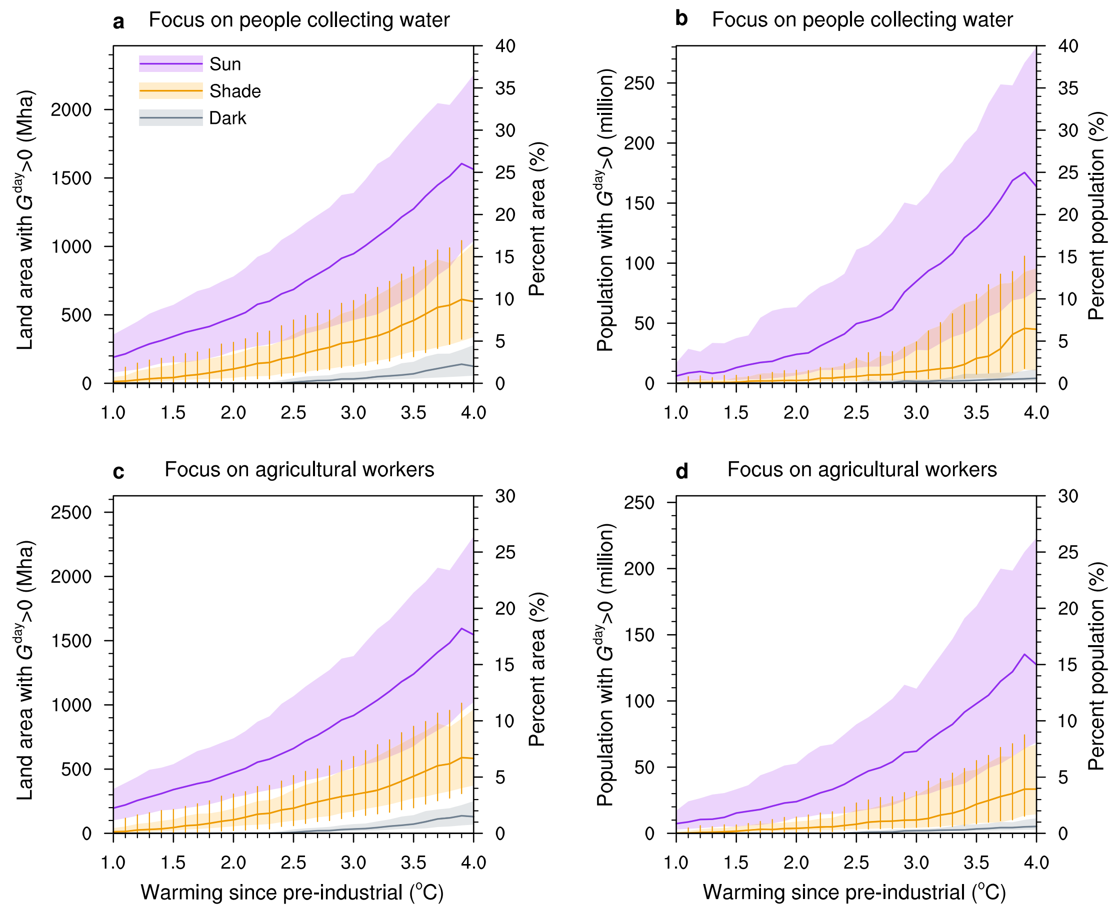

Fig. 5 | Projected exposure to uncompensable heat stress ($G^{day} > 0$ W m^{-2}) for subpopulations engaged in outdoor water collection and farming. Land area (**a**, **c**) and population (**b**, **d**) at risk, shown separately for those engaged in water collection (**a**, **b**) and farming (**c**, **d**) under sun, shade, and dark scenarios. Percentage estimates are restricted to the specified subpopulation: for example, in **a**, the "Percent area (%)" refers to the percent of the land area currently inhabited by people who must walk outside to collect water that is projected to experience uncompensable heat stress. Spatially resolved water access data and agricultural population data are described in Supplementary Method 2 and presented in Supplementary Fig. 2. Lines denote the ensemble median, and the shaded areas indicate the 25th–75th percentile interval. In the shade scenario, the orange line indicates the average radiation exposure under shade and the error bars indicate the uncertainty (±50% of R_{in}; Eq. (3) for the shade scenario) under various shading objects. Uncompensable heat stress impacts are determined using the average data of a 10-year period matching each global warming amount most closely (tolerance of ±0.05 °C). There are only ten models that provide 10-year data corresponding to the warming amount of 4 °C, which contributes to a slight drop in the ensemble median at 4 °C.

warming amounts and increase at a higher rate with more radiation exposure. In comparison, the projected areal impact assuming zero solar radiation (dark) remains much lower across different levels of warming. The projected impacted population engaged in water collection (Fig. 5b) increases from 24.1 to 163.8 million (3.4–23%) under the sun scenario, about 40 times that projected under the dark scenario (from 0 to 4 million or 0–0.6%) when global warming increases from 2 to 4 °C. The projected impacted population engaged in farming (Fig. 5d) also increases rapidly from 23.9 to 127.4 million (2.8–15%) under the sun scenario, about 25 times that projected under the dark scenario (from 0 to 5 million or 0–0.6%), when global warming increases from 2 to 4 °C.

The presence of shade mitigates the effect of solar radiation on outdoor activities but does not eliminate it. In average shade conditions (orange lines in Fig. 5), the projected population engaged in water collection or farming at risk of uncompensable heat stress reduces to about one-fourth of that projected under the sun scenario but is still more than six times higher than under the dark scenario. We also consider a range of radiation exposure from ~16% of total solar radiation under dense tree canopies in the summer[31] to ~50% under plastic shading nets[29,30] (see the "Methods" subsection "Heat stress scenario"). The corresponding projected impacted population who collect water outside ranges from 11 to 99 million, consistently higher than the 4 million under the dark scenario, at 4 °C warming. The same is true for agricultural workers on farms.

The prevalence and frequency of uncompensable heat are both projected to increase with radiation exposure and further warming (Fig. 6, Supplementary Fig. 13). The area-weighted mean annual number of days with $G^{day} > 0$ W m^{-2} is projected to be about 8 (4) days for populations engaged in water collection or farming under the sun (shade) scenario at 2 °C warming (Fig. 6). At 4 °C warming, it increases to about 14 (10) days for the sun (shade) scenario, about 3 (2) times that predicted under the dark scenario. The annual cumulative hours with $G > 0$ are even longer and impact more regions if using 3-h values (Supplementary Fig. 14) instead of daytime means (G^{day}). In some hotspot regions such as the Sahel, Amazon, the Persian Gulf, and Northern India/Pakistan, outdoor workers from the two subpopulations may experience a cumulative total of more than two weeks or 168 h of uncompensable heat stress per year at 4 °C warming (Supplementary Figs. 13 and 14).

On days in which $G^{day} > 0$ W m^{-2}, outdoor activities (including water collection and farming) will need to occur at night or in the very early morning, even when shaded. Figure 7 shows that across grid cells and days

Fig. 6 | Projected occurrence frequency of uncompensable heat stress for subpopulations engaged in outdoor water collection and farming. Area-weighted mean annual number of days with $G^{day} > 0$ W m^{-2} for those engaged in water collection (**a**) and farming (**b**) under sun, shade, and dark scenarios. Lines denote the ensemble median and the shaded areas indicate the 25th–75th percentile interval. The statistics consider only those grid cells where people must spend more than 30 min per day outside to collect drinking water (**a**) or where agricultural workers live in rural areas (**b**). A minimum of three grid cells with ensemble median $G^{day} > 0$ under the dark scenario are used to compute the area-weighted mean annual number of days.

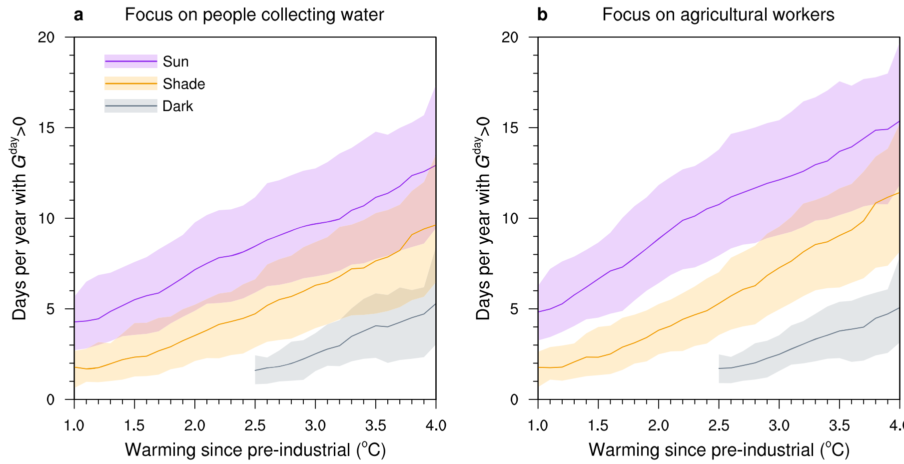

Fig. 7 | Mean diel cycle of G for the subpopulation engaged in outdoor water collection. Mean 3-h G under 1–4 °C (**a**–**d**, respectively) of global warming. Statistics for sun, shade, and dark scenarios across warming levels are based on a common set of grid cells (see the “Methods” subsection “Normalizing by global warming amount”). The hour of day is the local time at each grid cell according to the solar zenith angle and 12 indicates local solar noon. All solid lines denote the ensemble median, and the shaded areas indicate the 25th–75th percentile interval across 12 CMIP6 models. The equivalent plot for the subpopulation engaged in farming is similar and shown in Supplementary Fig. 11.

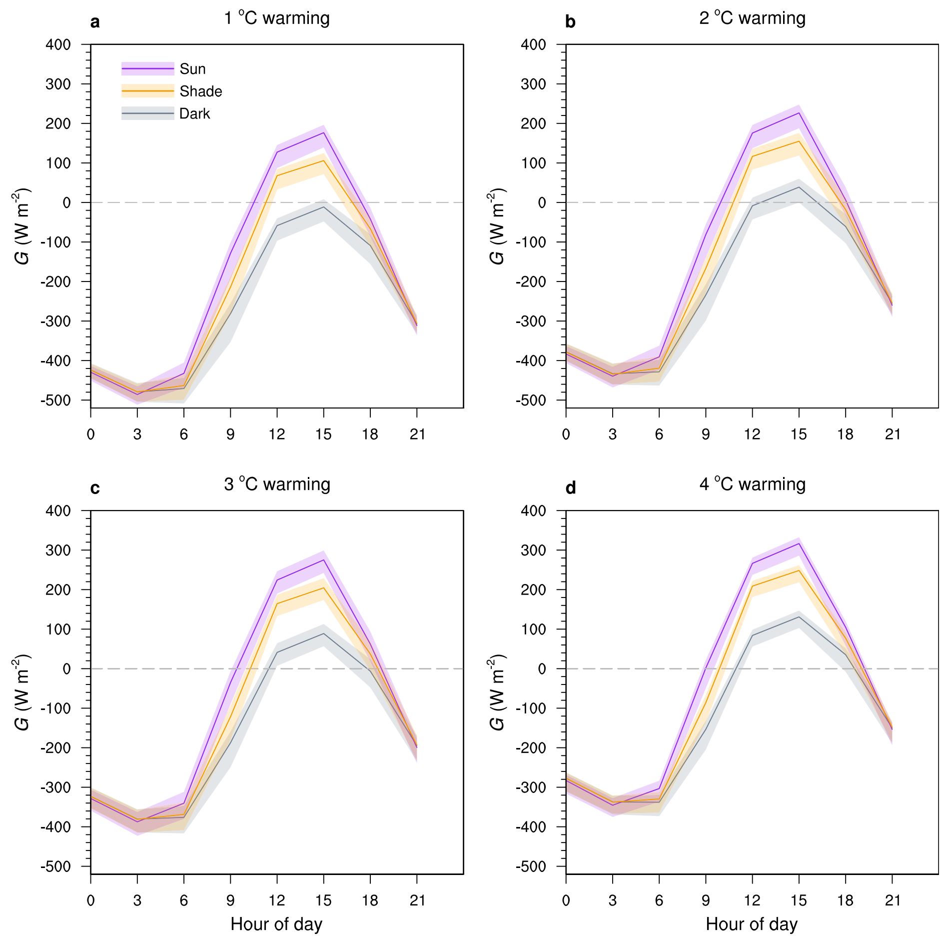

in which $G^{day} > 0$ W m^{-2}, the mean 3-h value of G is projected to exceed zero during most daytime hours (9:00–18:00) but stay below zero in the early morning (6:00–9:00) and during the night (18:00–6:00) under the sun scenario. The 3-h G is projected to exceed zero at slightly later hours and at higher warming levels under the shade scenario compared to the sun scenario. In either case, the extent (Fig. 4), frequency (Fig. 6), and duration (Fig. 7) of uncompensable heat in the daytime are all projected to increase with increased warming. The 3-hourly G is also projected to exceed zero at later hours, but in very limited numbers of grid cells and days, under the dark scenario at 3-4 °C warming.

The above results focus on fit, well-acclimated people with a maximum sweat capacity of 500 W m^{-2} (ref. 48). For non-acclimated people whose maximum sweat capacity reduces to 400 W m^{-2} (ref. 48), the projected risk of uncompensable heat stress among those engaged in water collection or farming is about twice as large compared to those who are acclimated (Supplementary Fig. 12).

Discussion

Our study underscores the importance of including radiative heat loads in heat stress projections. Our intermediate-complexity physically based human energy balance model with parsimonious physiological parameters offers a climate model-friendly approach for assessing global risks of uncompensable heat stress under any climate regime and radiative condition. The model proves accurate in predicting the body core temperature inflection points under uncompensable heat conditions in laboratory heat stress experiments (Fig. 2). Using bias-corrected climate data, our model consistently projects higher intensity (Fig. 3), frequency (Fig. 6), duration (Fig. 7), and land area and specific population impacts (Fig. 5) of uncompensable heat stress concerning outdoor activities compared to that measured without radiative effects; such risks are projected to emerge widely in hot-dry and hot-humid regions with increasing warming levels (Fig. 4). We also decompose the contributions of climatic (temperature, humidity, radiation, wind speed) and physiological (metabolic heat, sweating capacity) variables to the body's energy balance, and show strong radiative effects on uncompensable heat stress co-regulated by evaporative efficiency and sweating capacity.

A raft of recent studies[10,24,25] has demonstrated that the conventional adaptability threshold of 35 °C T_W insufficiently captures the effect of human thermophysiological limitations on the occurrence of uncompensable heat stress. This motivated the adoption of empirically determined uncompensable heat stress thresholds[11,12,47] or the application of human energy balance models with physiological considerations[42,49] in recent studies[24,33]. However, most of these studies unrealistically assume zero solar radiation and constant wind speeds for outdoor conditions[11,12,24,47]. A few studies that attempted to model solar radiation effects on uncompensable heat stress relied on oversimplified radiation inputs[17,33]. For example, the partitional calorimetry model[49] requires mean radiant temperature (T_r) as a key input to assess radiative effects, but T_r is not an output variable from global climate models and is not commonly measured by weather stations. T_r itself requires detailed modeling of radiative fluxes absorbed by a human body[50]. Thus, Vanos et al.[33] approximated midday radiant temperature, T_r, by assuming it was always 15 °C higher than T_a under partly cloudy conditions (blue shaded region in Supplementary Fig. 16c) for their "sun" scenario. They ignored the diurnal cycle and tight correlation between radiation and variables such as temperature[51] and atmospheric clearness (K_t), which substantially underestimates the solar radiation heat load on the hottest (most often clear) days (orange shaded region in Supplementary Fig. 16b; more details below). Additionally, they assumed an arbitrary wind speed of 1 m s^{-1} for a moving person, which fails to capture the crucial nonlinear effect of wind speed on the body's energy balance.

Our study fills this gap by explicitly modeling the diurnal cycle of radiation absorbed by people outdoors under various weather conditions using sun-angle and view-angle corrected downwelling and upwelling radiative fluxes (Eqs. (3) and (4)). Our analysis of the ERA5 reanalysis data shows that more than 75% of warm weather ($T_a > 25$ °C) has relatively clear sky conditions ($K_t > 0.5$, Supplementary Fig. 16a) and more than 66% of the hottest 1% heat stress events (when G^{day} (dark) exceeds the 99th percentile) occur under clear and sunny conditions ($K_t > 0.7$, Supplementary Fig. 16b), which implies a strong radiative heat load (Supplementary Fig. 16d) and impact on outdoor activities, even when averaged over daytime (Figs. 4–6). Even under cloudy conditions ($K_t < 0.25$, Supplementary Fig. 16d), the heat load from solar radiation (mostly diffuse) remains substantial, with values (~80 W m^{-2}) comparable to those attained while sheltering in the shade, which we have shown still substantially contribute to uncompensable heat stress (Figs. 4–7). Furthermore, the efficiency of heat dissipation via sweating can be lower due to lower convective heat transfer with diminished wind in confined spaces or under shading objects[28], which, in turn, can increase the sensitivity of the body's energy budget to radiation and metabolic heat (Supplementary Fig. 6).

Our study specifically focuses on subpopulations engaged in essential outdoor activities, with especially limited capacity for sheltering indoors for extended periods without compromising labor productivity and livelihood. By focusing on two specific subpopulations, each representing nearly 1 billion people, our results imply that unavoidable outdoor activities, including drinking water collection and farming, may increasingly have to become nocturnal or limited to the very early morning for millions of people. In many cases, such as in urban slums, water demand is already so high that reducing the accessible window will likely preclude some from accessing it at all[52,53]. Farming usually requires long hours of outdoor labor and is closely tied to seasonal growing cycles and market demand[34,54]; these constraints appear largely incompatible with timing constraints imposed by our heat stress projections (Figs. 6and 7, Supplementary Fig. 14). Even if direct health impacts can be avoided by major behavioral changes, those changes will incur major social, economic and political consequences that are, themselves, fundamental aspects of heat stress impacts[34,54–56].

Many studies used daily maximum heat stress metrics[2,6,11,23,24,57] and some considered rarer extremes (such as 1-in-30-year events[2,6,23]), which are not directly comparable to our WoE and impact analysis based on daytime mean values and annual events. Among recent studies that have similar thermophysiological considerations to ours[11,33,47], Vecellio et al.[47] used 3-h data from twelve CMIP6 models comparable to ours. They applied empirical critical T_W thresholds[10] determined from experimental chambers[25] to climate data assuming zero solar radiation exposure and minimal wind speed. An indoor scenario simulated by our model with the same assumptions finds very similar global distributions of annual cumulative hours of uncompensable heat stress ($G > 0$) at different warming levels, especially for the hotspot regions of Northern India and Pakistan, the Persian Gulf, Eastern China, Northern Africa, Amazon and Northern Australia (Supplementary Fig. 15e–h, comparable to Fig. 1a–d in ref. 47). However, as noted by Powis et al.[11] who used the same critical T_W thresholds, these thresholds were most representative for mid-latitude populations from which participants in the trials were selected[25], which probably explains some remaining differences from the projection of our physically based model. These empirical thresholds assumed higher than resting metabolic heat (mean $M = 83$ W m^{-2}) for subjects doing light activity in the experimental chamber[25]. Given the close correspondence between our dark scenario and others[11,47] (Table 1), we also take the opportunity to extend our results to show uncompensable heat stress during complete rest. This represents the most conservative scenario in terms of metabolic heat generation ($M = 59$ W m^{-2}) and is particularly relevant for older adults, as recently investigated[58]. We find that the global average annual hours of uncompensable heat stress under the resting scenario are approximately one-fourth (one-third) of those projected under the light activity scenario at 2 °C (4 °C) of warming, when all other assumptions are identical (Supplementary Fig. 15a–d). Although the difference in M is only 24 W m^{-2}, the body's energy balance (or critical T_W threshold) is particularly sensitive to extra heat in indoor conditions with no wind. This is also the case when extra solar radiation (sun or shade) is considered together with finite wind speeds, which substantially increase the duration (Supplementary Fig. 14) and impact (Figs. 4–7) of uncompensable heat stress compared to the dark scenarios. The interplay between radiative or metabolic heat load and the convective heat transfer coefficient h_c determined by wind speed is clearly illustrated by our model, which should be considered in future assessments of heat stress impacts. Assuming fixed wind speeds for outdoor activities, as in prior studies[24,33], overlooks this important mechanism.

The impacts of solar radiation on uncompensable heat stress are especially large when realistic sweating capacity limits are included. This is particularly true for hot-dry regions, where hot temperatures, strong solar radiation, dry air and often high wind speeds (Supplementary Fig. 19) induce high demand for sweat evaporation. Such evaporative demand often exceeds the sweating capacity even for an idealized fit and acclimated person. This is consistent with recent studies[10,25,33,47] that found wider discrepancies between the physical 35 °C T_W adaptability limit and the physiological critical T_W thresholds in hot-dry conditions than in humid conditions. Our attribution analysis (Fig. 3) shows the additional radiative heat load under the sun or shade scenario, compared to the dark scenario, contributes even more than sweating capacity limits to the occurrence of uncompensable heat stress. This further demonstrates the importance of providing improved measures of the human heat burden caused by direct sunlight and diffuse radiation under shading objects.

Some caveats are warranted. Model projections of near-surface quantities are subject to considerable model uncertainty, even after bias correction, as conducted here (Supplementary Method 3). G may be overestimated for densely forested tropical regions, particularly the Amazon, due to the underestimation of near-surface wind speed in South America by most CMIP6 models[59]. The bias appears to stem from the models' rules for converting land-use input data into land-cover dynamics, which tend to overestimate both forest cover and biomass density in the Amazon[60]. The problem could be further compounded by uncertainties in the input land-use data's representation of deforestation[61], including both large-scale clearing and fine-scale disturbances, for both current and projected scenarios. We partly address uncertainties in our analysis through two approaches: first, by applying bias and variance corrections to all near-surface climate variables (Supplementary Method 3), and second, by conducting sensitivity analyses on key variables and parameters (Supplementary Method 4) and comparing scenarios of low and high radiation exposure. Those sensitivity analyses confirm that our presented results are rather conservative. We ignored the effect of protective clothing on outdoor workers[51]. On the one hand, clothes can reduce absorbed solar radiation, which reduces heat stress; on the other hand, clothes reduce the effective wind speed at the skin surface and trap heat and moisture, which increases it. Regardless, in one set of experiments, solar radiation consistently reduced the physical work capacity of subjects with either low or high clothing coverage especially in hot conditions[51]. Future work can extend our intermediate-complexity model to assess the additional effects of clothing and other personal factors on the uncompensable heat stress threshold[62]. By using daytime mean G our estimated impacts are more conservative than using the daytime maximum G because simply sheltering for the hottest part of the day will not be sufficient to avoid these effects. Our modeling results cannot be used to infer mortality and morbidity impacts, which often occur well below the uncompensable limit due to various health and complicating factors, as shown in past[5,13] and recent[63] heatwave-mortality records. Such risks under compensable heat should be estimated by approaches that incorporate physiological vulnerabilities or mortality data[14,33]. Despite these limitations, the uncompensable heat stress threshold identified by our model can serve as an important upper bound for adaptability, although tighter than in most previous studies[1,10,24,25,47]. Our results help quantify the extra sensitivity of uncompensable heat stress to warming due to the inclusion of radiative, wind and metabolic effects that will impact millions of people whose essential daily activities must be completed outdoors.

Methods

Any physically based study of heat stress must stipulate: (A) a detailed scenario describing the human experiencing heat stress and their environment; (B) a physical model for calculating heat stress for that human; and (C) forcing data for the heat stress model. These aspects are detailed in the following subsections.

Heat stress scenario

Our model applies to the case of an idealized fit, unclothed, and fully hydrated person, consistent with previous studies[1,6,7,9,23,24]. In addition, we have included basic physiological considerations as in recent studies[10,11,24,33], while keeping the model as simple as possible. The three physiological parameters included in our model are mean skin surface temperature, metabolic heat generation associated with outdoor activities and sweat capacity limits for acclimated and non-acclimated persons, respectively[48]. Our model specifically quantifies the daytime mean radiative and wind effects under three clearly defined scenarios (below), focusing on subpopulations engaged in outdoor drinking water collection and agricultural work (see Supplementary Method 2 "Population distribution data"). The reason to use daytime mean values and these two subpopulations are to ensure that uncertainties in radiation exposure associated with human behavioral modification are strongly constrained.

We consider three radiative scenarios in which (1) full solar radiation is included (sun); (2) only diffuse radiation is included (shade); (3) no solar radiation is included (dark, Table 1). In the shade scenario, the model-simulated diffuse radiation is used as a proxy for radiation in the shade. In the climate models analyzed, the global land mean ratio of diffuse to full solar radiation (K_d) concurrent with annual maximum G^{day} under the shade scenario varies from 27% to 34% (Supplementary Table 2). The ensemble average K_d is 31% for all land grid cells and 27% for the hottest 1% of land grid cells, which are within the observed range of a fraction of solar radiation that is able to transmit through various shading objects (30-70%, mean ~50% under plastic shading nets[29,30], ~45% under discontinuous canopy[32], and ~16% under dense tree canopies in the summer[31]). The amount of unavoidable radiation in outdoor shade conditions depends on the actual environment (the type of and the position under shading objects and the albedo of surrounding surfaces). To further account for this uncertainty, we varied the amount of radiation input under shade (Eq. 3 for shade) by ±50%, which results in the radiation input closely matching the mean fraction of solar radiation transmitted below shading nets and below tree canopies.

The dark scenario is intended to compare with recent studies that have similar assumptions to ours but ignore radiation[10–12]. We also consider two additional scenarios in which metabolic heat and sweating limits are varied (dark*, dark**, Table 1) to compare with other studies[1,24,44]. No single scenario will be sufficient to capture the full complexity of human behavior in a catastrophic heatwave. However, since our model is physically based, it can be readily extended to study additional scenarios.

Energy balance model of heat stress

We use an intermediate complexity energy balance model of the human body to estimate heat stress (Eqs. (1)–(8)). Our model is simpler than full complexity human thermophysiological models[26,41–43,64,65] and the partitional calorimetry model of human heat balance and survivability[33,49], but more complex than the implied model in previous studies based on the wet-bulb temperature (see Eqs. (9)–(14)). Intermediate complexity models are widely recognized as essential for developing a fundamental understanding of climate science[66,67]. In the following, we describe the basic model (Eqs. (1)–(8)) and its derivatives (Eqs. (9)–(15)) that focus on identifying the uncompensable heat stress limit for the above scenarios.

In our model, the outer skin surface forms the boundary of a control volume. For this control volume, the first law of thermodynamics requires that

$$G = R_n - H - \lambda E + M \tag{1}$$

where G is the rate of storage of heat in the body (positive values imply a net gain [W m^{-2}]), R_n is the net radiant heat exchange across the skin surface (incoming minus outgoing radiation; Eqs. (2)–(5), H is the rate of convective heat exchange across the skin surface (positive values imply a net loss; Eq. (6)), λE is the rate of latent heat exchange through evaporation across the skin surface (positive values imply a net loss (Eqs. (7) and (8)), and M is the rate of metabolic heat production inside the body (always greater than zero and dependent on levels of activity). Other fluxes exist[3]—for example, heat conduction and respiration—but they are typically negligible compared to the other fluxes listed here and are ignored in our model. For humans (and endothermic animals), the energy inputs and outputs at the skin surface typically balance to maintain a stable core temperature. Uncompensable heat stress occurs when $G > 0$, which will eventually increase the body's core temperature above dangerous levels (sooner for larger G).

In Eq. (1), the net rate of radiant heat exchange, R_n, across the skin surface is modeled as

$$R_n = f_s(R_{in} + L_{in} - L_{out}) \tag{2}$$

where f_s is the fraction of total skin area effectively involved in radiant heat exchange (taken as a constant 0.8 from refs. 41,42), R_{in} is the incident sun-angle corrected solar radiation absorbed by the skin surface, L_{in} is incident and absorbed longwave radiation, and L_{out} is outgoing longwave radiation emitted by the body. R_{in} can be estimated for both sun and shade scenarios as follows if all input variables are available (see Supplementary Table 2):

$$R_{in} = \begin{cases} (1-\alpha)\left[\varphi R_b' + 0.5\left(R_d + R_g\right)\right], & \text{for sun scenario} \\ (1-\alpha)0.5\left(R_d + R_g\right), & \text{for shade scenario} \end{cases} \quad (3)$$

where α is the mean body reflectance of shortwave radiation ($\alpha = 0.3$ from refs. 26,68), φ is the human body's projected area factor for direct beam as a function of sun zenith angle (μ) according to ref. 26, R_b' is the incoming direct radiation received on a surface perpendicular to the beam which is converted from the direct beam radiation (R_b) incident on a horizontal surface by $R_b' = \frac{R_b}{\cos(\mu)}$, R_d is diffuse radiation, and R_g is reflected solar radiation from the ground. The outdoor shade scenario is a special case of R_{in} with R_b' equal to zero. Climate models usually provide total solar radiation (R_s) incident on a horizontal surface ($R_s = R_b + R_d$). Only six models provide R_d, for which direct beam incident on a horizontal surface is calculated by $R_b = R_s – R_d$. For the other models, we use the decomposition method from ref. 69 to estimate the diffuse fraction for each grid cell and each time step using solar constant, μ, and R_s as inputs. Sun zenith angle μ is calculated for each grid cell and each time step following a procedure from the Community Atmosphere Model (https://ncar.github.io/CAM/doc/build/html/cam5_scientific_guide/). See Supplementary Method 1 for details on sun angle correction and diffuse radiation calculation.

Absorbed incident longwave radiation (L_{in}) is calculated by

$$L_{in} = \varepsilon_s 0.5\left(L_d + L_g\right) \quad (4)$$

where L_d is the downwelling longwave flux from the atmosphere, L_g is upwelling longwave flux from the ground, ε_s is the emissivity (absorptivity) of the skin surface ($\varepsilon_s = 0.97$, refs. 42,68), and the number 0.5 is a view factor applied to the isotropic fluxes R_d, R_g, L_d, and L_g following refs. 70,71.

L_{out} can be estimated by the Stefan–Boltzmann Law:

$$L_{out} = \varepsilon_s \sigma \left(T_s + 273.15\right)^4 \quad (5)$$

where σ is the Stefan–Boltzmann constant (5.67×10^{-8} W m^{-2} K^{-4}), and T_s is skin surface temperature in °C. In order to maintain a healthy body core temperature of roughly 37 °C for acclimated and fit individuals[72], skin temperature is typically a little lower to maintain a positive energy gradient between the body's core and skin surface, allowing the body to dissipate heat[1,73]. Here T_s is treated as a constant value of 36 °C in the model because this value is often observed in people at rest in hot conditions[10] and prior to core body temperature rises[74]. A value of $T_s = 36$ °C gives a core-to-skin temperature gradient of 1 °C which is considered the minimum gradient to allow the body to dissipate heat in severe heat conditions[4,73] and is recommended for assessing heat stress and required sweating rates[75]. We investigate the sensitivity of our results to this assumption in Supplementary Method 4.

Sensible heat flux in and out of the body via convection depends on the temperature difference between the skin surface (T_s) and the surrounding air (T_a) and the skin surface convective heat transfer coefficient. Thus, H can be expressed as

$$H = h_c(T_s - T_a) \quad (6)$$

where h_c is the convective heat transfer coefficient [W m^{-2} K^{-1}], which is a non-linear function of wind speed (U). We use the relation $h_c = 14.1\, U^{0.5}$ for forced convection as in ref. 41. We have conducted a thorough literature review on the convective heat transfer coefficient for the human body (Supplementary Fig. 7) and conducted extensive sensitivity tests on our results by varying the h_c function and U (Supplementary Method 4). The choice of the h_c function from Fiala's model[41] is conservative as shown in Supplementary Fig. 8. Furthermore, we conservatively impose a minimum threshold on wind speed ($U_{min} = 0.1$ m s^{-1}) when calculating h_c for forced convection, as is common in parameterizations of boundary layer conductance and convection over land or ocean surfaces[76]. For wind speed below 0.1 m s^{-1} that may occur in indoor environments[28] or in tropical humid regions (e.g., the Amazon), we use the mean observed $h_c = 3.3$ W m^{-2} K^{-1} for natural convection (Supplementary Fig. 7).

The latent heat flux (λE_o) from a freely evaporating skin surface is calculated as follows:

$$\lambda E_o = \frac{\lambda h_c}{c_p}\left[q_s(T_s) - q_a\right] = \frac{h_c}{\gamma}\left[e_s(T_s) - e_a\right] \quad (7)$$

where λ is the latent heat of vaporization as a function of sweat temperature on the skin surface (assumed equal to T_s), h_c is defined above, c_p is the specific heat capacity of the air at constant pressure, $q_s(T_s)$ denotes saturation specific humidity (of sweat) evaluated at skin temperature, q_a is specific humidity of the air, $e_s(T_s)$ is saturation vapor pressure evaluated at skin temperature, e_a is air vapor pressure, and γ is the psychrometric constant ($\gamma = \frac{Pc_p}{\varepsilon\lambda}$, where P is surface air pressure and ε is the ratio of the molecular weight of water vapor to that of dry air). In practice, skin latent heat flux is limited by physiological constraints on sweat capacity. To account for this, actual evaporative heat flux from sweat (λE) is limited by the maximum sweating capacity (λE_{max}):

$$\lambda E = \begin{cases} \lambda E_{max}, & \text{if } \lambda E_o > \lambda E_{max} \\ \lambda E_o, & \text{if } \lambda E_o \le \lambda E_{max} \end{cases} \quad (8)$$

where λE_{max} is set to 500 W m^{-2} (corresponding to 1.25 l of sweat production per hour) for acclimated adults or 400 W m^{-2} (1 l per hour) for non-acclimated adults, according to the latest ISO 7933:2023 standard[48]. Here, our focus is on uncompensable heat stress, so we assume a completely saturated skin surface fully covered by sweat[48]. Default parameter values used in the above equations are provided in Supplementary Table 1.

The critical threshold for uncompensable heat stress is when G becomes positive, and is the focus of our analysis. When radiation, air temperature and relative humidity are at comfortable levels, H and λE are both positive and more than sufficient to counterbalance R_n and M; as a result, the body will cool ($G < 0$). Heat stress occurs when T_a approaches or surpasses T_s, so that H becomes negative (implying that convective heat fluxes are working to increase the body's temperature rather than decrease it), and λE becomes the primary channel to remove extra heat. If specific humidity (q_a) also rises sufficiently, λE may be unable to provide the required cooling; in this case, uncompensable heat stress occurs ($G > 0$ W m^{-2}).

To compare our results with those of previous studies based on wet-bulb temperature (T_W), we now explain how to convert between the two measures of heat stress (G [W m^{-2}] and T_W [°C or K]). The wet-bulb temperature is defined as the temperature of a parcel of air after it is cooled at constant pressure to saturation solely by evaporation of water into it using its own latent energy. An implicit equation for T_W is

$$c_p\left(T_a - T_W\right) = \lambda\left[q_s\left(T_W\right) - q_a\right] \quad (9)$$

Prior studies based on wet-bulb temperatures do not impose limits on sweating from the skin surface ($\lambda E = \lambda E_o$), and neglect radiative and metabolic heat loads ($R_n = M = 0$). Combining these assumptions with Eqs.

(1), (6), (7), and (9) yields:

$$-H-\lambda E_{\rm o}=-h_{\rm c}(T_{\rm s}-T_{\rm W})-\frac{\lambda h_{\rm c}}{c_{\rm p}}[q_{\rm s}(T_{\rm s})-q_{\rm s}(T_{\rm W})]=G_{\rm TW} \quad (10)$$

where $q_s(T_W)$ is saturation-specific humidity evaluated at T_W. G_{TW} is referred to as the T_W-equivalent energy flux (W m^{-2}), which is essentially the same as Eqs. (1), (6), and (7) without radiation and metabolic terms.

Sherwood and Huber[1] derived an effective energy flux F from T_W, where $F=k(T_s-T_W)$ (Eq. S2 in their Supporting Information). This relation is not obviously equivalent to Eq. (10); here, we reconcile this apparent discrepancy by deriving a similar equation in the context of our energy balance model. In addition to the assumptions made in the previous section (R_n and M are zero), assume a moderate difference between T_s and T_W. Then $q_s(T_s)$ and $q_s(T_W)$ can be linearized around the mean of T_W and T_s using the first-order Taylor approximations:

$$q_{\rm s}(T_{\rm s})\approx q_{\rm s}\left(\frac{T_{\rm W}+T_{\rm s}}{2}\right)+\Delta(T_{\rm s}-\frac{T_{\rm W}+T_{\rm s}}{2}) \quad (11)$$

$$q_{\rm s}(T_{\rm W})\approx q_{\rm s}\left(\frac{T_{\rm W}+T_{\rm s}}{2}\right)+\Delta(T_{\rm W}-\frac{T_{\rm W}+T_{\rm s}}{2}) \quad (12)$$

where $\Delta=\frac{{\rm d}q_s}{{\rm d}T}(\frac{T_W+T_s}{2})$ (i.e., the slope or first derivative of saturation-specific humidity with respect to temperature, evaluated at $T=\frac{T_W+T_s}{2}$). Subtracting Eq. (12) from Eq.(11) gives

$$q_{\rm s}(T_{\rm s})-q_{\rm s}(T_{\rm W})\approx\Delta(T_{\rm s}-T_{\rm W}), \text{where } \Delta=\frac{{\rm d}q_{\rm s}}{{\rm d}T}\left(\frac{T_{\rm W}+T_{\rm s}}{2}\right) \quad (13)$$

This linearization is a reasonable approximation of $q_s(T_s)-q_s(T_W)$ when T_s–T_W is not too large (Supplementary Fig. 27). Substituting Eq. (13) into Eq. (10) gives

$$-H-\lambda E_{\rm o}=-h_{\rm c}(1+\frac{\lambda}{c_{\rm p}}\Delta)(T_{\rm s}-T_{\rm W})=G_{\rm TW} \quad (14)$$

If we define $k=-h_c(1+\frac{\lambda}{C_p}\Delta)$, then Eq. (14) becomes $k(T_s-T_W)=G_{TW}$ (k is a negative value and positive G_{TW} means energy enters the body), which has the same form as equation S2 in ref. 1. Note that k is not constant but changes with wind speed, h_c, and $\frac{T_W+T_s}{2}$ (since Δ is a function of $\frac{T_W+T_s}{2}$).

The above derivation shows that G_{TW} (Eq. (10) or Eq. (14)) is a special case of our G model (Eqs. (1)–(8)) in which radiative and metabolic heat sources are ignored (Fig. 1a), along with limits to sweat capacity (Eq. 8). Thus, our energy balance model (Fig. 1b) generalizes previous work based on wet-bulb temperature by relaxing those assumptions. We note that Sherwood and Huber[1] used the value T_s = 35 °C (rather than the value of T_s = 36 °C used in our G model; see description of Eq. (5)) when deriving the adaptability limit of T_W = 35 °C. Equation (10) or (14) shows that when $T_W=T_s$ = 35 °C, G_{TW} = 0, which implies dissipation of metabolic heat (M is about 59 W m^{-2} for a resting person) is not possible. However, according to observations T_s routinely rises above 35 °C in hot conditions before core temperature rises[74]. Using T_s = 36 °C in Eqs. (10) or (14) would give G_{TW} = −58 W m^{-2} when T_W = 35 °C and U = 1 m s^{-1}, which is nearly equivalent to G = 0 calculated by our model (Eqs. 1–8) if adding unavoidable metabolic heat (M = 59 W m^{-2}) to G_{TW} while assuming no solar and longwave radiative heating as in Sherwood and Huber[1]. The choice of any fixed value of T_s is an approximation to the physiological response of skin to heat and depends on whether considering M or not. Our validation with experimental data shows that using T_s = 36 °C in our model (Eqs. (1)–(8)) gives accurate predictions of G = 0 and core temperature inflection points (Fig. 2), whereas using T_s = 35 °C would overestimate G (Supplementary Method 4). Nevertheless, we use T_s = 35 °C when converting T_W to G_{TW} (Eq. (10) or (14)) to be consistent with Sherwood and Huber[1] and to enable a cross-comparison (Fig. 3).

Model validation and cross-comparison

We validate the above model (Eqs. (1)–(8)) using chamber experimental data from the PSU-HEAT project[25] in a similar way to validation conducted in recent studies[33,44,77]. The dataset includes two sets of experiments, one on subjects cycling an ergometer (MinAct, mean M = 83 W m^{-2}), and another on subjects walking on a treadmill (LightAmb, mean M = 133 W m^{-2}). Each set of experiments included six trials: the first three had fixed T_a of about 36, 38, and 40 °C while the vapor pressure (e_a) was gradually increased until the core temperature (T_c) inflecion point was observed; the other three had fixed e_a of about 2.7, 2.1, and 1.6 kPa while T_a was gradually increased until the T_c inflection point was observed. These 12 combinations of critical T_a and e_a (or RH) and two levels of metabolic heat (83 and 133 W m^{-2}) are used as inputs to the model to predict G (G = 0 indicates T_c inflection point). The 25 subjects involved in the experiments were healthy, young adults, consistent with our model assumption. Their light clothing is ignored in our model. Solar radiation is set to zero and only longwave radiation exchange is considered using the skin (T_s) and air (T_a) temperatures. Since the experiments were conducted in closed environmental chambers without forced air movement, we set the convective heat transfer coefficient h_c to 3.3 W m^{-2} K^{-1}, representing natural convection, which is determined from a thorough literature review (Supplementary Fig. 7). Due to the lack of forced convection, model predicted sweat evaporation rates in all experiments are well below the maximum sweat capacity set in Eq. (8) for both non-acclimated and acclimated adults. The model predicted G and standard deviations for the twelve combinations of T_a and e_a are presented in Fig. 2 (see Supplementary Fig. 9 for RH on the Y-axis), which accurately reflects the observed T_c inflection points across the range of critical environmental conditions.

To enable cross-comparison with other studies, we also analyze the sky condition (cloudy or sunny) and mean radiant temperature (T_r) when heat stress occurs. The sky condition is measured by atmospheric clearness (K_t) which is calculated as the ratio of downwelling shortwave radiation at the surface (R_s) to the extra-terrestrial irradiance on a horizontal surface[69], where the latter is a function of solar constant and sun zenith angle (see Supplementary Method 1 and Supplementary Fig. 1). T_r is converted from the sum of sun-angle and view-angle corrected shortwave radiation and longwave radiation absorbed by the body (R_{in} and L_{in} from Eqs. (3) and (4)) according to the following equation[68]:

$$T_{\rm r}=\sqrt[4]{\frac{R_{\rm in}+L_{\rm in}}{\varepsilon_{\rm s}\sigma}}-273.15 \quad (15)$$

In Supplementary Fig. 16, K_t, T_r and R_{in} are computed from 3-h data from the ERA5 reanalysis for one example year (2009). Their midday values are selected according to local sun zenith angle to compare with ref. 33.

Forcing data and data processing

We use 3-h climate data from 1980 to 2099 from twelve CMIP6 models (Supplementary Table 2). We first regrid the nine input variables (T_a, RH, R_s, R_d, R_g, L_d, L_g, U, P) of these models to a common 360 × 180 longitude/latitude grid (using bilinear interpolation) and then conduct bias and variance correction on these variables from twelve models with reference to 30 years of ERA5 (WFDE5 v2.1) reanalysis data over land (see Supplementary Method 3 "Bias correction and evaluation"). We calculate G and T_W using bias-corrected three-hourly data and then calculate daytime mean values (G^{day}, $T_W{}^{day}$), where daytime is determined by solar zenith angle less than 90°. Ensemble statistics (median, and 25–75th percentiles) are derived at each grid cell and then summarized spatially to quantify the global aggregate impact of uncompensable heat stress on land area and population.

We use outdoor estimates of forcing variables, as we focus on specific subpopulations engaged in key outdoor activities (water collection and farming work, see Supplementary Method 2 "Population distribution data"). Although we consider different sources of radiation and conduct incidence angle corrections to incoming solar and longwave radiation (Eqs. (3) and (4)) as present in some full-complexity human energy balance models, further studies are warranted to fully understand radiative effects by considering additional scenarios of shortwave and longwave radiation within different surroundings (e.g., urban street canyons).

Normalizing by global warming amount

To remove the dependence of our results on a specific climate projection, we normalize all the results by specific global warming amounts relative to preindustrial in a similar way to ref. 46. The normalized results represent the sensitivity of heat stress severity and impact on global warming. For each of the twelve CMIP6 models in our ensemble, global warming amounts since the preindustrial are determined by (i) calculating the model-simulated difference of 30-year running means of global (area-weighted) mean temperature relative to the 1980–2009 mean and (ii) adding the observed warming experienced in 1980–2009 relative to 1850–1900 to this amount. The observed mean warming in 1980–2009 (0.69 °C) is calculated as the ensemble median of HadCRUT5[78], BerkeleyEarth[79], NOAAGlobalTemp[80] global mean air temperature analysis datasets. We focus on the warming amounts from 1 to 4 °C projected by most models within the range of our data (fewer than five models predict warming amounts higher than 4.5 °C by 2099). We use the global warming amounts to estimate the warming of emergence (WoE) for uncompensable heat stress, defined as the lowest warming amount needed such that $G^{day} > 0$ W m^{-2} occurs for at least one day per year. The WoE is determined for each grid cell by finding the first 10-year running mean G^{day} exceeding zero and recording the global warming amount corresponding most closely to the 10-year period (matched within a tolerance of ±0.05 °C) as the WoE (Fig. 4). We also present the impacts of uncompensable heat stress associated with a given warming amount (Fig. 7) or along a warming gradient (Figs. 3–6) using the average G^{day} sampled for the 10-year period matching each specific warming amount most closely (within a tolerance of ±0.05 °C) for each model to be included in the ensemble statistics (median and 25–75th percentiles). To demonstrate how uncompensable heat stress extends throughout the day with increased warming, we also show the mean diel profiles of 3-h G using a common set of grid cells in Fig. 7. These cells are selected based on where $G^{day} > 0$ first appears at 1 °C of warming under the sun scenario for each subpopulation.

Data availability

The original CMIP6 climate data for the 12 models[81–92] used in this study are available through the Earth System Grid Federation (ESGF) nodes (https://esgf-node.llnl.gov/search/cmip6/)[45]. The HadCRUT5[78], BerkeleyEarth[79], and NOAAGlobalTemp[80] global air temperature series can be sourced from https://crudata.uea.ac.uk/cru/data/temperature/, https://berkeleyearth.org/data/, https://psl.noaa.gov/data/gridded/data.noaaglobaltemp.html, respectively. The post-processed data that support the findings of this study are available via the Harvard Dataverse (https://doi.org/10.7910/DVN/XFV1GE)[93].

Code availability

The model code was developed using the NCAR Command Language (NCL version 6.6.2). Code for replicating the figures and analyses was written in NCL (version 6.6.2) or R (version 4.3.2). Code for the model and for the figures and analyses has been deposited in the Harvard Dataverse at https://doi.org/10.7910/DVN/XFV1GE.

Received: 14 August 2024; Accepted: 25 November 2024;
Published online: 12 December 2024

References

1. Sherwood, S. C. & Huber, M. An adaptability limit to climate change due to heat stress. *Proc. Natl Acad. Sci. USA* **107**, 9552–9555 (2010).
2. Raymond, C., Matthews, T. & Horton, R. M. The emergence of heat and humidity too severe for human tolerance. *Sci. Adv.* **6**, eaaw1838 (2020).
3. Buzan, J. R. & Huber, M. Moist Heat Stress on a Hotter Earth. *Annu. Rev. Earth Planet. Sci.* **48**, 623–655 (2020).
4. Havenith, G. & Fiala, D. Thermal indices and thermophysiological modeling for heat stress. In *Comprehensive Physiology* Vol. 6 255–302 (John Wiley & Sons, Ltd, 2016).
5. Mora, C. et al. Global risk of deadly heat. *Nat. Clim. Change* **7**, 501–506 (2017).
6. Im, E.-S., Pal, J. S. & Eltahir, E. A. B. Deadly heat waves projected in the densely populated agricultural regions of South Asia. *Sci. Adv.* **3**, e1603322 (2017).
7. Zhang, Y., Held, I. & Fueglistaler, S. Projections of tropical heat stress constrained by atmospheric dynamics. *Nat. Geosci.* **14**, 133–137 (2021).
8. Kang, S. & Eltahir, E. A. B. North China Plain threatened by deadly heatwaves due to climate change and irrigation. *Nat. Commun.* **9**, 1–9 (2018).
9. Mishra, V. et al. Moist heat stress extremes in India enhanced by irrigation. *Nat. Geosci.* **13**, 722–728 (2020).
10. Vecellio, D. J., Wolf, S. T., Cottle, R. M. & Kenney, W. L. Evaluating the 35 °C wet-bulb temperature adaptability threshold for young, healthy subjects (PSU HEAT Project). *J. Appl. Physiol.* **132**, 340–345 (2022).
11. Powis, C. M. et al. Observational and model evidence together support wide-spread exposure to noncompensable heat under continued global warming. *Sci. Adv.* **9**, eadg9297 (2023).
12. Justine, J., Monteiro, J. M., Shah, H. & Rao, N. The diurnal variation of wet bulb temperatures and exceedance of physiological thresholds relevant to human health in South Asia. *Commun. Earth Environ.* **4**, 1–11 (2023).
13. Vicedo-Cabrera, A. M. et al. The burden of heat-related mortality attributable to recent human-induced climate change. *Nat. Clim. Change* **11**, 492–500 (2021).
14. Lüthi, S. et al. Rapid increase in the risk of heat-related mortality. *Nat. Commun.* **14**, 4894 (2023).
15. Budd, G. M. Wet-bulb globe temperature (WBGT)—its history and its limitations. *J. Sci. Med. Sport* **11**, 20–32 (2008).
16. Lemke, B. & Kjellstrom, T. Calculating workplace WBGT from meteorological data: a tool for climate change assessment. *Ind. Health* **50**, 267–278 (2012).
17. Kong, Q. & Huber, M. Explicit calculations of wet-bulb globe temperature compared with approximations and why it matters for labor productivity. *Earth's Future* **10**, e2021EF002334 (2022).
18. Parsons, L. A. et al. Global labor loss due to humid heat exposure underestimated for outdoor workers. *Environ. Res. Lett.* **17**, 014050 (2022).
19. Foster, J. et al. Quantifying the impact of heat on human physical work capacity; part II: the observed interaction of air velocity with temperature, humidity, sweat rate, and clothing is not captured by most heat stress indices. *Int. J. Biometeorol.* **66**, 507–520 (2021).
20. Rastogi, S. K., Gupta, B. N. & Husain, T. Wet-bulb globe temperature index: a predictor of physiological strain in hot environments. *Occup. Med. (Lond.)* **42**, 93–97 (1992).
21. Afshari, D., Moradi, S., Angali, K. A. & Shirali, G.-A. Estimation of heat stress and maximum acceptable work time based on physiological and environmental response in hot-dry climate: a case study in traditional bakers. *Int. J. Occup. Environ. Med.* **10**, 194–202 (2019).
22. Sherwood, S. C. How important is humidity in heat stress? *J. Geophys. Res.: Atmos.* **123**, 11,808–11,810 (2018).
23. Pal, J. S. & Eltahir, E. A. B. Future temperature in southwest Asia projected to exceed a threshold for human adaptability. *Nat. Clim. Change* **6**, 197–200 (2016).

24. Lu, Y.-C. & Romps, D. M. Is a wet-bulb temperature of 35 °C the correct threshold for human survivability? *Environ. Res. Lett.* **18**, 094021 (2023).
25. Wolf, S. T., Cottle, R. M., Vecellio, D. J. & Kenney, W. L. Critical environmental limits for young, healthy adults (PSU HEAT Project). *J. Appl. Physiol.* **132**, 327–333 (2022).
26. Steadman, R. G. The assessment of sultriness. Part II: Effects of wind, extra radiation and barometric pressure on apparent temperature. *J. Appl. Meteor.* **18**, 874–885 (1979).
27. Chaiyapinunt, S. & Khamporn, N. Effect of solar radiation on human thermal comfort in a tropical climate. *Indoor Built Environ.* **30**, 391–410 (2020).
28. Huang, L. & Zhai, Z. J. Critical review and quantitative evaluation of indoor thermal comfort indices and models incorporating solar radiation effects. *Energy Build.* **224**, 110204 (2020).
29. Abdel-Ghany, A. M. & Al-Helal, I. M. Characterization of solar radiation transmission through plastic shading nets. *Sol. Energy Mater. Sol. Cells* **94**, 1371–1378 (2010).
30. Kotilainen, T., Robson, T. M. & Hernández, R. Light quality characterization under climate screens and shade nets for controlled-environment agriculture. *PLoS ONE* **13**, e0199628 (2018).
31. de Abreu-Harbich, L. V., Labaki, L. C. & Matzarakis, A. Effect of tree planting design and tree species on human thermal comfort in the tropics. *Landsc. Urban Plan.* **138**, 99–109 (2015).
32. Hardy, J. P. et al. Solar radiation transmission through conifer canopies. *Agric. For. Meteorol.* **126**, 257–270 (2004).
33. Vanos, J. et al. A physiological approach for assessing human survivability and liveability to heat in a changing climate. *Nat. Commun.* **14**, 7653 (2023).
34. Kjellstrom, T., Maître, N., Saget, C., Otto, M. & Karimova, T. *Working on a Warmer Planet: The Impact of Heat Stress on Labour Productivity and Decent Work* (International Labour Organization, Geneva, Switzerland, 2019).
35. European Commission. Joint Research Centre. *GHSL Data Package 2023*. (Publications Office of the European Union, LU, 2023).
36. UNICEF, WHO. *Progress on Household Drinking Water, Sanitation and Hygiene 2000–2022: A Focus on Gender* https://www.unicef.org/wca/media/9161/file/jmp-2023-wash-households-launch-version.pdf (2023).
37. Deshpande, A. et al. Mapping geographical inequalities in access to drinking water and sanitation facilities in low-income and middle-income countries, 2000–17. *Lancet Glob. Health* **8**, e1162–e1185 (2020).
38. Turner, V. K., Middel, A. & Vanos, J. K. Shade is an essential solution for hotter cities. *Nature* **619**, 694–697 (2023).
39. Bonan, G. *Ecological Climatology: Concepts and Applications* (Cambridge University Press, Cambridge, 2015).
40. Vanos, J. K., Baldwin, J. W., Jay, O. & Ebi, K. L. Simplicity lacks robustness when projecting heat-health outcomes in a changing climate. *Nat. Commun.* **11**, 6079 (2020).
41. Fiala, D., Lomas, K. J. & Stohrer, M. A computer model of human thermoregulation for a wide range of environmental conditions: the passive system. *J. Appl Physiol. (1985)* **87**, 1957–1972 (1999).
42. Steadman, R. G. The assessment of sultriness. Part I: a temperature-humidity index based on human physiology and clothing science. *J. Appl. Meteor.* **18**, 861–873 (1979).
43. Gagge, A. P., Fobelets, A. P. & Berglund, P. E. A standard predictive index of human response to the thermal environment. *ASHRAE Trans.* **92**, 709–731 (1986).
44. Lu, Y.-C. & Romps, D. M. Predicting fatal heat and humidity using the heat index model. *J. Appl. Physiol.* **134**, 649–656 (2023).
45. Eyring, V. et al. Overview of the Coupled Model Intercomparison Project Phase 6 (CMIP6) experimental design and organization. *Geosci. Model Dev.* **9**, 1937–1958 (2016).
46. Matthews, T. K. R., Wilby, R. L. & Murphy, C. Communicating the deadly consequences of global warming for human heat stress. *Proc. Natl Acad. Sci. USA* **114**, 3861–3866 (2017).
47. Vecellio, D. J., Kong, Q., Kenney, W. L. & Huber, M. Greatly enhanced risk to humans as a consequence of empirically determined lower moist heat stress tolerance. *Proc. Natl Acad. Sci.* **120**, e2305427120 (2023).
48. ISO 7933. *Ergonomics of the Thermal Environment—Analytical Determination and Interpretation of Heat Stress Using Calculation of the Predicted Heat Strain* (ISO, 2023).
49. Cramer, M. N. & Jay, O. Partitional calorimetry. *J. Appl. Physiol.* **126**, 267–277 (2018).
50. Gál, C. V. & Kántor, N. Modeling mean radiant temperature in outdoor spaces, a comparative numerical simulation and validation study. *Urban Clim.* **32**, 100571 (2020).
51. Foster, J. et al. Quantifying the impact of heat on human physical work capacity; part III: the impact of solar radiation varies with air temperature, humidity, and clothing coverage. *Int. J. Biometeorol.* **66**, 175–188 (2022).
52. Price, H., Adams, E. & Quilliam, R. S. The difference a day can make: the temporal dynamics of drinking water access and quality in urban slums. *Sci. Total Environ.* **671**, 818–826 (2019).
53. Khetan, A. K., Yakkali, S., Dholakia, H. H. & Hejjaji, V. Adaptation to heat stress: a qualitative study from Eastern India. *Environ. Res. Lett.* **19**, 044035 (2024).
54. Nelson, G. C. et al. Global reductions in manual agricultural work capacity due to climate change. *Glob. Change Biol.* **30**, e17142 (2024).
55. Kjellstrom, T., Lemke, B. & Otto, M. Mapping occupational heat exposure and effects in South-East Asia: ongoing time trends 1980−2011 and future estimates to 2050. *Ind. Health* **12**, 56−67 (2013).
56. Habibi, P. et al. Climate change and heat stress resilient outdoor workers: findings from systematic literature review. *BMC Public Health* **24**, 1711 (2024).
57. Falchetta, G., De Cian, E., Sue Wing, I. & Carr, D. Global projections of heat exposure of older adults. *Nat. Commun.* **15**, 3678 (2024).
58. Tony Wolf, S., Cottle, R. M., Fisher, K. G., Vecellio, D. J. & Larry Kenney, W. Heat stress vulnerability and critical environmental limits for older adults. *Commun. Earth Environ.* **4**, 1–10 (2023).
59. Shen, C. et al. Evaluation of global terrestrial near-surface wind speed simulated by CMIP6 models and their future projections. *Ann. N. Y. Acad. Sci.* **1518**, 249–263 (2022).
60. Ma, L. et al. Global rules for translating land-use change (LUH2) to land-cover change for CMIP6 using GLM2. *Geosci. Model Dev.* **13**, 3203–3220 (2020).
61. Hurtt, G. C. et al. Harmonization of global land use change and management for the period 850–2100 (LUH2) for CMIP6. *Geosci. Model Dev.* **13**, 5425–5464 (2020).
62. Bernard, T. E., Wolf, S. T. & Kenney, W. L. A novel conceptual model for human heat tolerance. *Exerc. Sport Sci. Rev.* **52**, 39–46 (2024).
63. Ballester, J. et al. Heat-related mortality in Europe during the summer of 2022. *Nat. Med* **29**, 1857–1866 (2023).
64. Lu, Y.-C. & Romps, D. M. Extending the heat index. *J. Appl. Meteorol. Climatol.* **61**, 1367–1383 (2022).
65. Ou, Y., Wang, F., Zhao, J. & Deng, Q. Risk of heatstroke in healthy elderly during heatwaves: a thermoregulatory modeling study. *Build. Environ.* **237**, 110324 (2023).
66. Held, I. M. The gap between simulation and understanding in climate modeling. *Bull. Am. Meteor. Soc.* **86**, 1609–1614 (2005).
67. Maher, P. et al. Model hierarchies for understanding atmospheric circulation. *Rev. Geophys.* **57**, 250–280 (2019).
68. Di Napoli, C., Hogan, R. J. & Pappenberger, F. Mean radiant temperature from global-scale numerical weather prediction models. *Int. J. Biometeorol.* **64**, 1233–1245 (2020).

69. Erbs, D. G., Klein, S. A. & Duffie, J. A. Estimation of the diffuse radiation fraction for hourly, daily and monthly-average global radiation. *Sol. Energy* **28**, 293–302 (1982).
70. Kenny, N. A., Warland, J. S., Brown, R. D. & Gillespie, T. G. Estimating the radiation absorbed by a human. *Int. J. Biometeorol.* **52**, 491–503 (2008).
71. Kubaha, K., Fiala, D., Toftum, J. & Taki, A. H. Human projected area factors for detailed direct and diffuse solar radiation analysis. *Int. J. Biometeorol.* **49**, 113–129 (2004).
72. Hanna, E. G. & Tait, P. W. Limitations to thermoregulation and acclimatization challenge human adaptation to global warming. *Int. J. Environ. Res. Public Health* **12**, 8034–8074 (2015).
73. Cuddy, J. S., Hailes, W. S. & Ruby, B. C. A reduced core to skin temperature gradient, not a critical core temperature, affects aerobic capacity in the heat. *J. Therm. Biol.* **43**, 7–12 (2014).
74. Fiala, D., Lomas, K. J. & Stohrer, M. Computer prediction of human thermoregulatory and temperature responses to a wide range of environmental conditions. *Int. J. Biometeorol.* **45**, 143–159 (2001).
75. Parsons, K. C. International standards for the assessment of the risk of thermal strain on clothed workers in hot environments. *Ann. Occup. Hyg.* **43**, 297–308 (1999).
76. Mol, W. B., van Heerwaarden, C. C. & Schlemmer, L. Surface moisture exchange under vanishing wind in simulations of idealized tropical convection. *Geophys. Res. Lett.* **46**, 13602–13609 (2019).
77. Vecellio, D. J., Wolf, S. T., Cottle, R. M. & Kenney, W. L. Utility of the Heat Index in defining the upper limits of thermal balance during light physical activity (PSU HEAT Project). *Int. J. Biometeorol.* **66**, 1759–1769 (2022).
78. Morice, C. P. et al. An updated assessment of near-surface temperature change from 1850: the HadCRUT5 data set. *J. Geophys. Res.: Atmos.* **126**, e2019JD032361 (2021).
79. Rohde, R. A. & Hausfather, Z. The Berkeley earth land/ocean temperature record. *Earth Syst. Sci. Data* **12**, 3469–3479 (2020).
80. Vose, R. S. et al. Implementing full spatial coverage in NOAA's global temperature analysis. *Geophys. Res. Lett.* **48**, e2020GL090873 (2021).
81. Dix, M. et al. CSIRO-ARCCSS ACCESS-CM2 model output prepared for CMIP6 ScenarioMIP ssp585 (Earth System Grid Federation, 2019).
82. Semmler, T. et al. *AWI AWI-CM1.1MR Model Output Prepared for CMIP6 ScenarioMIP ssp585* (Earth System Grid Federation, 2019).
83. Xin, X. et al. *BCC BCC-CSM2MR Model Output Prepared for CMIP6 ScenarioMIP ssp585* (Earth System Grid Federation, 2019).
84. Lovato, T. & Peano, D. *CMCC CMCC-CM2-SR5 Model Output Prepared for CMIP6 ScenarioMIP ssp585* (Earth System Grid Federation, 2020).
85. Consortium (EC-Earth), E.-E. *EC-Earth-Consortium EC-Earth3 Model Output Prepared for CMIP6 ScenarioMIP ssp585* (Earth System Grid Federation, 2019).
86. John, J. G. et al. *NOAA-GFDL GFDL-ESM4 Model Output Prepared for CMIP6 ScenarioMIP ssp585* (Earth System Grid Federation, 2018).
87. Panickal, S. et al. *CCCR-IITM IITM-ESM Model Output Prepared for CMIP6 ScenarioMIP ssp585* (Earth System Grid Federation, 2020).
88. Kim, Y. et al. *KIOST KIOST-ESM Model Output Prepared for CMIP6 ScenarioMIP ssp585* (Earth System Grid Federation, 2019).
89. Shiogama, H., Abe, M. & Tatebe, H. *MIROC MIROC6 Model Output Prepared for CMIP6 ScenarioMIP ssp585* (Earth System Grid Federation, 2019).
90. Tachiiri, K. et al. *MIROC MIROC-ES2L Model Output Prepared for CMIP6 ScenarioMIP ssp585* (Earth System Grid Federation, 2019).
91. Wieners, K.-H. et al. *MPI-M MPI-ESM1.2-LR Model Output Prepared for CMIP6 ScenarioMIP ssp585* (Earth System Grid Federation, 2019).
92. Yukimoto, S. et al. MRI MRI-ESM2.0 model output prepared for CMIP6 ScenarioMIP ssp585 (Earth System Grid Federation, 2019).
93. Fan, Y. & McColl, K. Model Code and Source Data for: Widespread outdoor exposure to uncompensable heat stress with warming. *Harvard Dataverse* https://doi.org/10.7910/DVN/XFV1GE (2024).

Acknowledgements

Y.F. acknowledges funding from the Shenzhen Science and Technology Program (No. ZDSYS20220606100806014), Scientific Research Start-up Funds (QD2023021C) from Tsinghua Shenzhen International Graduate School, and Harvard University's Solar Geoengineering Research Program fellowship. K.A.M. acknowledges funding from a Sloan Research Fellowship and the Dean's Competitive Fund for Promising Scholarship from Harvard University. We thank Sarah McColl for illustrating Fig. 1, Senyao Feng for postprocessing the water access and agricultural population data, and the CMIP6 community for making the three-hourly climate data available.

Author contributions

K.A.M. and Y.F. designed the study. Y.F. developed the model code, performed data analyses and drafted the manuscript. K.A.M. contributed to model development, interpretation of results, and manuscript editing. Both authors approved the final manuscript.

Competing interests

The authors declare no competing interests.

Additional information

Supplementary information The online version contains supplementary material available at https://doi.org/10.1038/s43247-024-01930-6.

Correspondence and requests for materials should be addressed to Yuanchao Fan or Kaighin A. McColl.

Peer review information *Communications Earth & Environment* thanks the anonymous reviewer(s) for their contribution to the peer review of this work. Primary handling editor: Martina Grecequet. A peer review file is available.

Supplementary Information for

Widespread outdoor exposure to uncompensable heat stress with warming

Yuanchao Fan[1,2*], Kaighin A. McColl[1,3*]

[1]Shenzhen Key Laboratory of Ecological Remediation and Carbon Sequestration, Institute of Environment and Ecology, Tsinghua Shenzhen International Graduate School, Tsinghua University, Shenzhen, China.

[2]Department of Earth and Planetary Sciences, Harvard University, Cambridge, MA, USA.

[3]School of Engineering and Applied Sciences, Harvard University, Cambridge, MA, USA.

*Corresponding authors: Yuanchao Fan (yuanchao.fan@sz.tsinghua.edu.cn) and Kaighin A. McColl (kmccoll@seas.harvard.edu)

This PDF file includes:

Supplementary Tables

Supplementary Table 1: Parameters and input variables used in the human energy balance model.

Parameters	Meaning	Default value [unit]	Reference
α	Body (skin) reflectance	0.3 [-]	1
ε_s	Emissivity of skin surface	0.97 [-]	2,3
σ	Stefan-Boltzmann constant	5.67×10^{-8} [W m^{-2} K^{-4}]	4
c_p	Specific heat capacity of air	1.01 [J g^{-1} K^{-1}]	4,5
λ	Latent heat of vaporization as a function of sweat or skin temperature (T_s)	$\approx 2.418 \times 10^3$ [J g^{-1}]	5,6
ε	Ratio of the mean molecular weight of water to that of dry air	0.622 [-]	4,7
φ	Body projected area factor for view angle correction of direct beam	a function of solar zenith angle (μ)	8
f_s	Effective radiant area ratio of the skin surface	0.8 [-]	2,9
T_s	Mean skin temperature	36 [°C]	10
M	Metabolic heat during complete rest/moderate work	59/176 [W m^{-2}] or 100/300 [W] divided by standard body surface area 1.7 m^2	11–14
λE_{max}	Maximum sweating capacity for acclimated/non-acclimated adults	500/400 [W m^{-2}] or 1.25/1 [litre h^{-1}]	15

Supplementary Table 2: List of CMIP6 models[16–27] and the data used in this study.

Model	Ensemble	Experiment	Period	Grid	Native 3-hourly variables	Global mean diffuse fraction
ACCESS-CM2[16]	r1i1p1f1	historical, ssp585	1980-2099	gn	tas, huss, ps, rsds, rsdsdiff, rsus, rlds, rlus, uas, vas	0.30 (provided)
AWI-CM-1-1-MR[17]	r1i1p1f1	historical, ssp585	1980-2099	gn	tas, hurs (6-hourly), ps, rsds, rsus, rlds, rlus, sfcWind	0.31 (estimated)
BCC-CSM2-MR[18]	r1i1p1f1	historical, ssp585	1980-2099	gn	tas, huss, ps, rsds, rsdsdiff, rsus, rlds, rlus, uas, vas	0.33 (provided)
CMCC-CM2-SR5[19]	r1i1p1f1	historical, ssp585	1980-2099	gn	tas, huss, ps, rsds, rsdsdiff, rsus, rlds, rlus, sfcWind	0.32 (provided)
EC-Earth3[20]	r1i1p1f1	historical, ssp585	1980-2099	gr	tas, huss, ps, rsds, rsus, rlds, rlus, sfcWind	0.32 (estimated)
GFDL-ESM4[21]	r1i1p1f1	historical, ssp585	1980-2099	gr1	tas, huss, ps, rsds, rsus, rlds, rlus, uas, vas	0.33 (estimated)
IITM-ESM[22]	r1i1p1f1	historical, ssp585	1980-2099	gn	tas, huss, ps (monthly), rsds, rsdsdiff, rsus, rlds, rlus, sfcWind	0.32 (provided)
KIOST-ESM[23]	r1i1p1f1	historical, ssp585	1980-2099	gr1	tas, huss, ps, rsds, rsus, rlds, rlus, uas, vas	0.31 (estimated)
MIROC6[24]	r1i1p1f1	historical, ssp585	1980-2099	gn	tas, huss, ps, rsds, rsus, rlds, rlus, sfcWind	0.27 (estimated)
MIROC-ES2L[25]	r1i1p1f2	historical, ssp585	1980-2099	gn	tas, huss, ps, rsds, rsus, rlds, rlus, uas, vas	0.28 (estimated)
MPI-ESM1-2-LR[26]	r1i1p1f1	historical, ssp585	1980-2099	gn	tas, huss, ps, rsds, rsus, rlds, rlus, sfcWind	0.31 (estimated)
MRI-ESM2-0[27]	r1i1p1f1	historical, ssp585	1980-2099	gn	tas, huss, ps, rsds, rsdsdiff, rsus, rlds, rlus, uas, vas	0.34 (provided)

Supplementary Methods

Supplementary Method 1: Description of input data and procedure to estimate diffuse radiation

Supplementary Table 2 summarizes the CMIP6 models and provided variables used in this study. We use the CMIP6 experiments 'historical' for the period 1980-2014 and 'ssp585' for the period 2015-2099 to calculate the global distribution and time trend of G and its statistics. Thirty years (1980-2009) of historical data is needed for bias correction of CMIP6 with reference to ERA5 (see Supplementary Method 3). The original variable names correspond to the variables used in this study as follows: 'tas' is near-surface air temperature (T_a), 'huss' is near-surface specific humidity (q_a), 'ps' is surface pressure (P), 'rsds' is surface total downwelling solar radiation (R_s, also called global radiation), 'rsdsdiff' is diffuse radiation (R_d), 'rsus' is upwelling shortwave radiation reflected from the ground (R_g), 'rlds' is downwelling longwave radiation from the atmosphere (L_d), 'rlus' is upwelling longwave from the ground (L_g), and 'sfcWind' is wind speed (U) simulated at 10 meter height. Some models do not provide 'sfcWind' but instead provide 'uas' for the eastward component of U and 'vas' for the northward component of U, which are converted to 'sfcWind'. Relative humidity (RH) is calculated for each model using q_a, T_a and P. While most models provide three-hourly data for all variables, there are a few exceptions: AWI-CM-1-1-MR and IITM-ESM provide 6-hourly 'hurs' (RH) and monthly P, respectively. In this case, we interpolate them bilinearly to three-hourly. All climate variables were simulated at 2-m reference height (T_a, q_a or RH) or near the surface (P, R_s, R_d, R_g, L_d and L_g which are not distinguishable from 2-m), except for wind speeds (sfcWind, uas, vas) which were simulated at 10 m. We estimate 2-m wind (U) by multiplying 10-m wind with a logarithmic wind profile factor 0.75 (ref.[7], similar to that used in Fiala et al.[28]). Actual wind experienced by a person could be lower than 2-m wind as the average height of body centre is smaller than 2 m, but we use all climate variables at 2 m for consistency.

Only six models originally provide 'rsdsdiff' (R_d) and the diffuse fraction ($K_d = R_d/R_s$, last column of Supplementary Table 2) is calculated directly for each model using the concurrent R_d and R_s values used to calculate G^{day} (daytime mean G). For the other six models the diffuse fraction and R_d are estimated using 3-hourly R_s, solar zenith angle (μ), and solar constant as inputs based on a well-established relationship between K_d and the atmospheric clearness index (K_t, the ratio of R_s to the extra-terrestrial irradiance on a horizontal surface, the latter is a function of solar constant and μ)[29]. We compared three decomposition methods – ERBS[29], BRL[30,31], and ABREU[32] – with radiation measurements from a flux tower during 2016-

2021 (Supplementary Fig. 1). The three methods all use solar constant, μ, and R_s as inputs and are suitable for hourly or 3-hourly data. The accuracy of estimated R_d is within ±2 W m^{-2} in the annual average compared to the observed R_d at the flux tower. The ERBS method gives the mean R_d closest to the measurements and the second lowest root mean squared error (16.7 W m^{-2}). Although the ABREU method has the lowest root mean squared error (15.8 W m^{-2}), it tends to overestimate the daily maximum R_d and it requires input of climate zone if used at the global scale. Although there are other more complex methods developed for estimating diffuse radiation at the minute time scale[33], we opt for the simpler ERBS method because our intention of using diffuse radiation is only to represent the scenario of relatively lower radiation exposure in outdoor shaded environments compared to full solar radiation under the sun, but not aimed to accurately reproduce the 3-hourly diffuse radiation for the CMIP6 models that do not provide this variable. The diffuse radiation and direct beam components are necessary for view angle correction of incoming solar radiation (Eq. 3). With the bias-corrected data, the mean K_d of all land grid cells concurrent with annual maximum G^{day} under the shade scenario is 0.31 (and 0.27 for the hottest 1% of land grid cells).

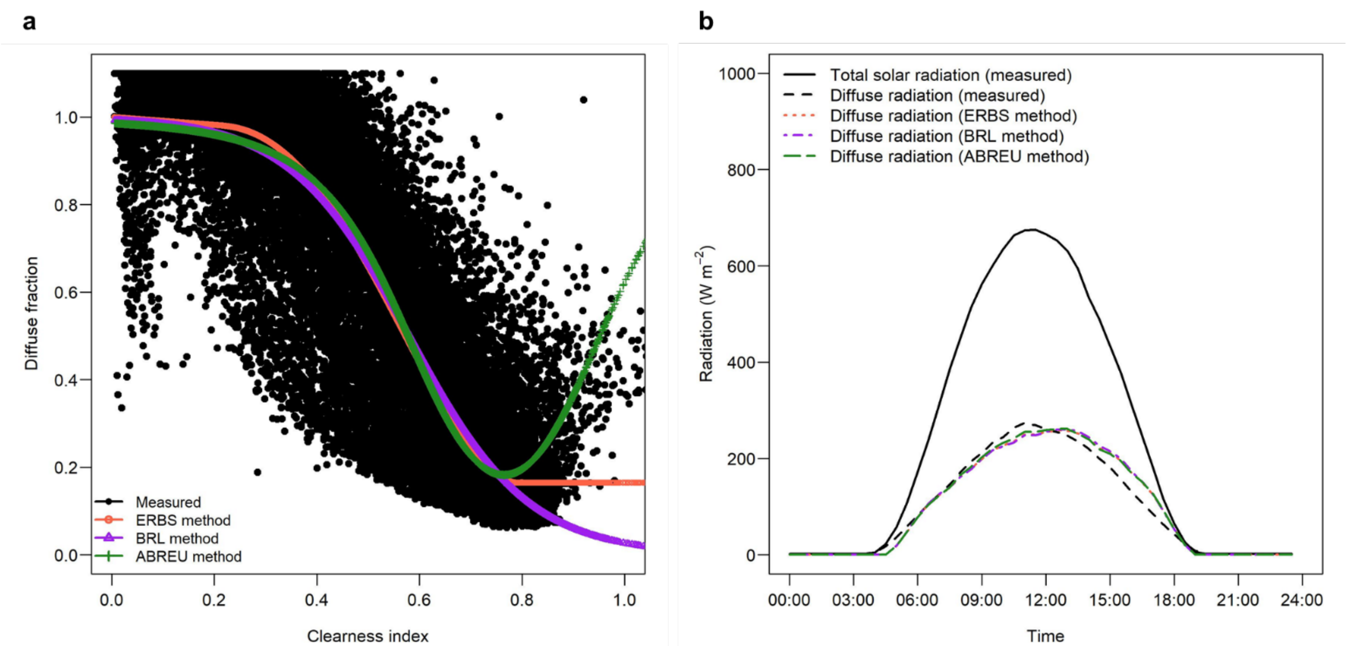

Supplementary Fig. 1: Comparison of three decomposition methods (ERBS, BRL, ABREU) for estimating diffuse fraction. **a** Empirical relationship between the atmospheric clearness index (K_t, the ratio of R_s to the extra-terrestrial irradiance on a horizontal surface) and the diffuse fraction (K_d, the ratio of R_d to R_s). **b** Comparison of estimated diffuse radiation (R_d) by three methods with measured values at a flux tower during 2016-2021 (NEON Bartlett Experimental Forest (US-xBR), Lon –71.29°, Lat 44.06°).

Supplementary Method 2: Population distribution data

We focus our analysis on populations engaged in two specific outdoor activities: water collection and farming. For water collection, we use a spatially-resolved dataset (0.041 degree resolution) of population distribution of four categories of drinking water access, including 1) piped water on or off premises, 2) other improved facilities (protected well/spring, rainwater, bottled water, tanker truck), 3) unimproved (unprotected well/spring), and 4) surface water (river, lake, canal, dam, surface water), created with data from more than 88 low-income and middle-income countries for the period of 2000-2017 (Deshpande et al. 2020[34], obtained from https://vizhub.healthdata.org/lbd/wash). The number of people without piped water access is about 2.88 billion in 2017 (including 2.13 billion in the category "other improved", 419 million in the category "unimproved", 336 million in the category "surface water"). This estimate is broadly consistent with the latest UNICEF, WHO report[35], which estimates approximately 2.2 billion people lacked safely managed drinking water on their premises in 2022. In this report, the definitions of unimproved and surface water are identical to those of the Deshpande et al. dataset, and the sum of basic services (improved source within 30 minutes round trip collection time) and limited services (improved source over 30 minutes round trip collection time) corresponds to the "other improved" category in the Deshpande et al. dataset. The number of people lacking safely managed drinking water on their premises is clearly decreasing over time due to progress in providing water services. Since Deshpande et al. is the only spatially resolved dataset we have found, we rescale its 2017 gridded data for each category (other improved, unimproved and surface water) so that their respective gross numbers match the 2022 UNICEF, WHO gross numbers for their corresponding categories (limited services, unimproved and surface water). The rescaled spatial data (Supplementary Fig. 2a) represents the subpopulations (total 703 million) who most likely spend more than 30 mins per day collecting water, which are the focus of our impact analysis. We apply the rescaled data to the whole century. Estimates of the precise number of people who must spend more than 30 mins per day to collect drinking water are subject to considerable uncertainty. Nevertheless, it is clear that many hundreds of millions of people must spend more than 30 minutes outdoors to access drinking water.

For farming, we use the spatially-resolved global distribution of urban and rural populations from the Global Human Settlement Layer (GHSL) project[36] (obtained from https://human-settlement.emergency.copernicus.eu/download.php), which was produced based on the GHS-POP R2023A population grid[37] and the GHS-SMOD R2023A settlement layers[38]. Among the population categories provided, we choose "Rural Cluster" (with 500-5000 inhabitants in the cluster and a density of > 300 inhabitants per km^2 of permanent land) and "Low Density Rural grid cells" (with a density of > 50 inhabitants per km^2 and not part of a Rural Cluster) to represent rural populations, which have a total of

1391 million people in 2020. According to the International Labour Organization (ILO) report[39], there are about 850 million agricultural workers worldwide in 2018, which is about 61% of the rural population of the GHSL dataset, matching closely with the 61.2% of employment in global rural areas represented by skilled agricultural, fishery and forestry workers from the 2020 ILO report[40]. Thus, we rescale the 2020 GHSL 1000-km resolution gridded dataset of rural populations by 61% so that its total population matches the gross number of agricultural workers from the ILO reports (850 million) but retains its spatial distribution (see Supplementary Fig. 2b). When estimating the impacts of uncompensable heat stress on these two subpopulations, we assume their most recent population data remain constant in future. Further studies are needed to estimate their future changes.

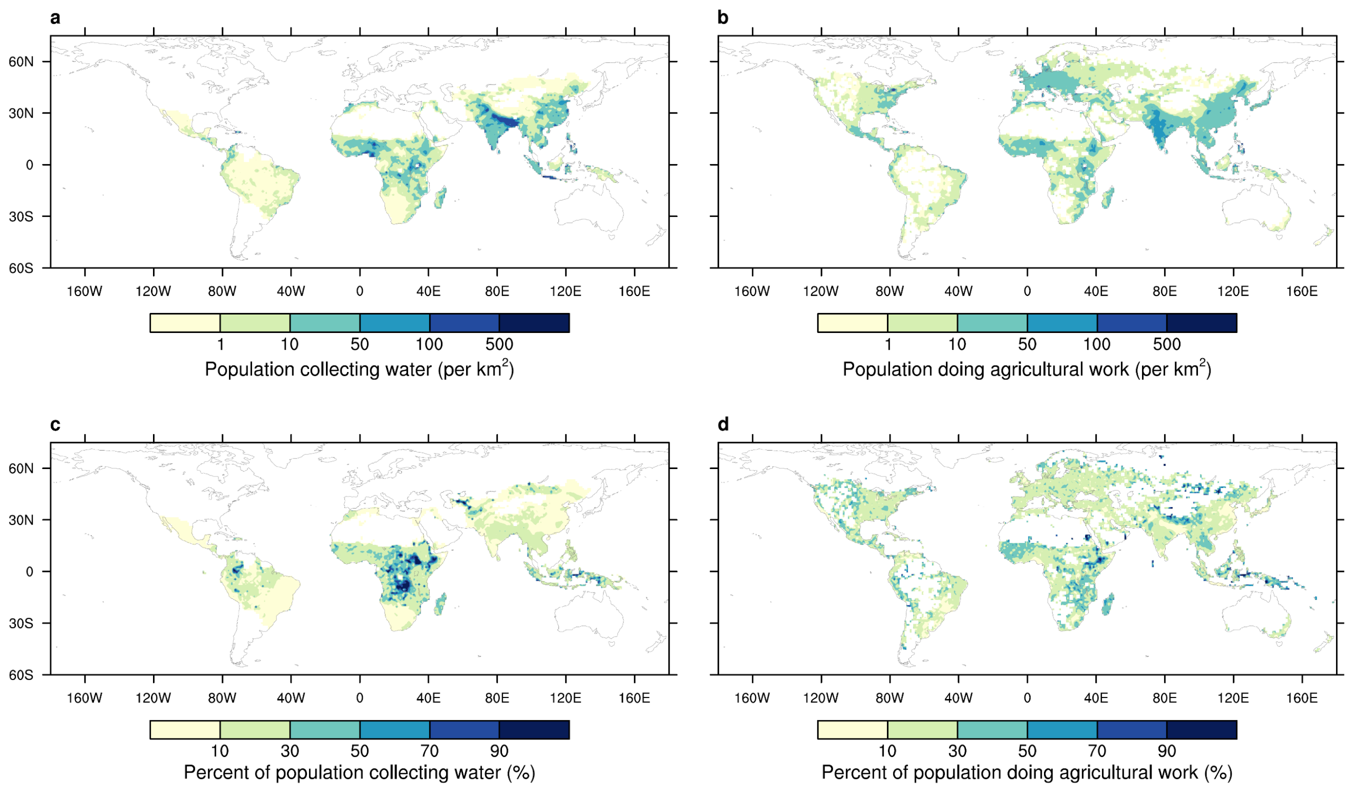

Supplementary Fig. 2: Distribution of subpopulations engaged in outdoor water collection and farming. The population (number of people per km^2) who spend more than 30 mins per day collecting water outdoors (**a**) and the population doing agricultural work in rural areas (**b**). The corresponding percentages of total population belonging to these subgroups are presented in (**c**) and (**d**).

Supplementary Method 3: Bias correction and evaluation

We use the European Centre for Medium-Range Weather Forecasts ERA5 reanalysis dataset from 1980 to 2009 as the reference for variance and bias adjustment of the CMIP6 dataset. The reference dataset includes six near surface meteorological variables from the latest bias-corrected ERA5 reanalysis (WFDE5 v2.1, generated using the WATCH Forcing Data methodology applied to ERA5 reanalysis data): Tair, Qair, PSurf, Wind, SWdown, and LWdown, corresponding to tas, huss, ps, sfcWind (or uas, vas), rsds, and rlds in Supplementary Table 2, and three ERA5 single-level radiation fields: mean surface diffuse short-wave radiation flux (rsdsdiff = rsds – rsdsdir (direct shortwave)), mean surface upwelling (reflected) short-wave radiation flux (rsus = rsds – rsns (net shortwave)), and mean surface upwelling long-wave radiation flux (rlus = rlds – rlns (net longwave)). These variables are provided at 0.5° × 0.5° spatial resolution and hourly temporal resolution, which are re-gridded to the same 1° × 1° grid as CMIP6 using bilinear interpolation and resampled to 3-hourly time steps. The ERA5 and WFDE5 v2.1 are considered the best available observational-based reference for bias adjustment of future climate projections for climate impact studies[41]. We take the bias and variance correction procedure from ref.[42] to correct the climatological mean and interannual variance biases in each of the above nine CMIP6 variables in the following steps:

1) Detrend the 3-hourly ERA5 reanalysis and CMIP6 time series ($\mathrm{CMIP6^H}$, the superscript H denoting the historical 30-year period) of 1980-2009 to yield anomalies ($\mathrm{ERA5_{anomaly}}$, $\mathrm{CMIP6^H_{anomaly}}$) and calculate their standard deviations, the ratio of which is the variance correction factor (f_{VC}):

$$f_{\mathrm{VC}} = \frac{std(\mathrm{ERA5} - \mathrm{ERA5_{HT}})}{std(\mathrm{CMIP6^H} - \mathrm{CMIP6_{HT}})} \qquad \text{Eq. S1}$$

   where $\mathrm{ERA5_{HT}}$ and $\mathrm{CMIP6_{HT}}$ are the historical linear trends in 1980-2009. Detrending is necessary to avoid the problems of overestimating the standard deviation and inappropriately modifying the long-term trend during the variance correction of future time series.

2) Compute CMIP6 anomalies of the future period ($\mathrm{CMIP6^F}$, 2010-2099) by subtracting the 30-year backward running trend:

$$\mathrm{CMIP6^F_{anomaly}} = \mathrm{CMIP6^F} - \mathrm{CMIP6_{RT}} \qquad \text{Eq. S2}$$

   where $\mathrm{CMIP6_{RT}}$ for a given year is calculated as the linear trend of the previous 30 years. Using backward running trend is commonly done[42] as it allows obtaining the anomalies until 2099, whereas using centred 30-year running trend would limit the bias correction up to the year 2076. For the historical period (1980-2009), the anomalies are calculated in step 1.

3) Multiplying the historical and future anomalies ($\mathrm{CMIP6^H_{anomaly}}$, $\mathrm{CMIP6^F_{anomaly}}$) by the variance correction factor f_{VC} and adding back the historical and running trends yields the variance-corrected time series for historical and future periods:

$$\begin{aligned} \mathrm{CMIP6^H_{vc}} &= f_{\mathrm{VC}}\mathrm{CMIP6^H_{anomaly}} + \mathrm{CMIP6_{HT}} \\ \mathrm{CMIP6^F_{vc}} &= f_{\mathrm{VC}}\mathrm{CMIP6^F_{anomaly}} + \mathrm{CMIP6_{RT}} \end{aligned} \qquad \text{Eq. S3}$$

4) Calculate the climatological bias (b_{clim}) between $\mathrm{CMIP6}_{\mathrm{vc}}^{\mathrm{H}}$ and ERA5:

$$b_{\mathrm{clim}} = \overline{\mathrm{CMIP6}_{\mathrm{vc}}^{\mathrm{H}}} - \overline{\mathrm{ERA5}} \qquad \text{Eq. S4}$$

where $\overline{\mathrm{CMIP6}_{\mathrm{vc}}^{\mathrm{H}}}$ is the climatological mean of variance-corrected CMIP6 data in 1980-2009 at each 3-hourly time step and $\overline{\mathrm{ERA5}}$ is the corresponding climatology of ERA5 in the same period.

5) Finally, the bias- and variance-corrected time series is computed for the historical ($\mathrm{CMIP6}_{\mathrm{vcbc}}^{\mathrm{H}}$) and future ($\mathrm{CMIP6}_{\mathrm{vcbc}}^{\mathrm{F}}$) periods by subtracting b_{clim} from the above variance-corrected data ($\mathrm{CMIP6}_{\mathrm{vc}}^{\mathrm{H}}$, $\mathrm{CMIP6}_{\mathrm{vc}}^{\mathrm{F}}$) at each 3-hourly time step of each year:

$$\begin{aligned} \mathrm{CMIP6}_{\mathrm{vcbc}}^{\mathrm{H}} &= \mathrm{CMIP6}_{\mathrm{vc}}^{\mathrm{H}} - b_{\mathrm{clim}} \\ \mathrm{CMIP6}_{\mathrm{vcbc}}^{\mathrm{F}} &= \mathrm{CMIP6}_{\mathrm{vc}}^{\mathrm{F}} - b_{\mathrm{clim}} \end{aligned} \qquad \text{Eq. S5}$$

The above procedure corrects for interannual variance and climatological mean bias in CMIP6 data with respect to ERA5 while it does not affect model simulated long-term trends from 1980 to 2099, which is an important feature of this trend-preserving bias correction method[42,43]. We use ensemble statistics to show the ensemble median trend and inter-model uncertainties and additionally take the normalization procedure (main Methods section "Normalizing by global warming amount") to remove the dependence of our results on a specific climate projection.

We apply the above variance and bias correction procedure to all CMIP6 model variables listed in Supplementary Table 2. Additionally, to better preserve the physical realism of relative humidity (RH), we calculate RH from original specific humidity, air temperature and pressure of each model and ERA5, and then apply this procedure to correct for the variance and mean bias in RH. We then use the bias- and variance-corrected 3-hourly climate variables to compute G and T_{W}. We note that some studies[44,45] directly applied a climatological mean bias correction to daily maximum T_{W}, but not to the constituent climate variables, which misses competing effects on T_{W} (e.g., dry bias of RH offsetting warm bias of T_{a}) or may lead to over-correction due to non-linear amplification effects between different climate variables.

We validate the performance of the above bias and variance correction by comparing the original and corrected CMIP6 data with ERA5 both spatially (Supplementary Fig. 3 for the difference in T_{a} between CMIP6 models and ERA5 at each grid cell) and temporally (Supplementary Fig. 4 for global average annual mean of each variable, Supplementary Fig. 5 for global average daily mean and daily maximum values). The global mean (standard deviation) of bias in T_{a} during 1980-2009 is reduced from 0.7 (3.3) °C in the original data to 0.00007 (0.0016) °C in the bias- and variance-corrected data.

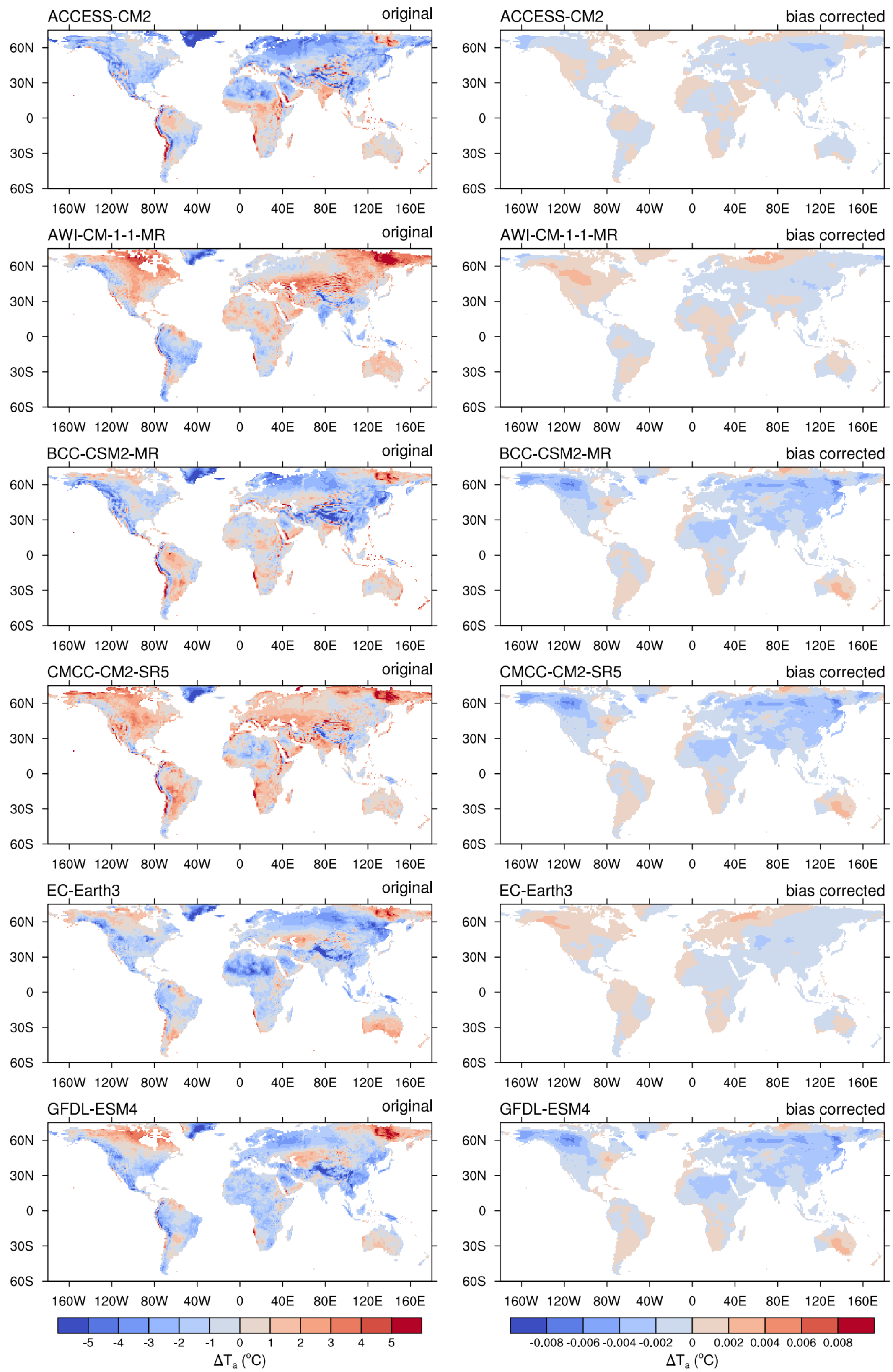

Supplementary Fig. 3: Thirty-year (1980-2009) mean difference in T_a between CMIP6 models (left column for original data, right column for bias- and variance-corrected data) and ERA5.

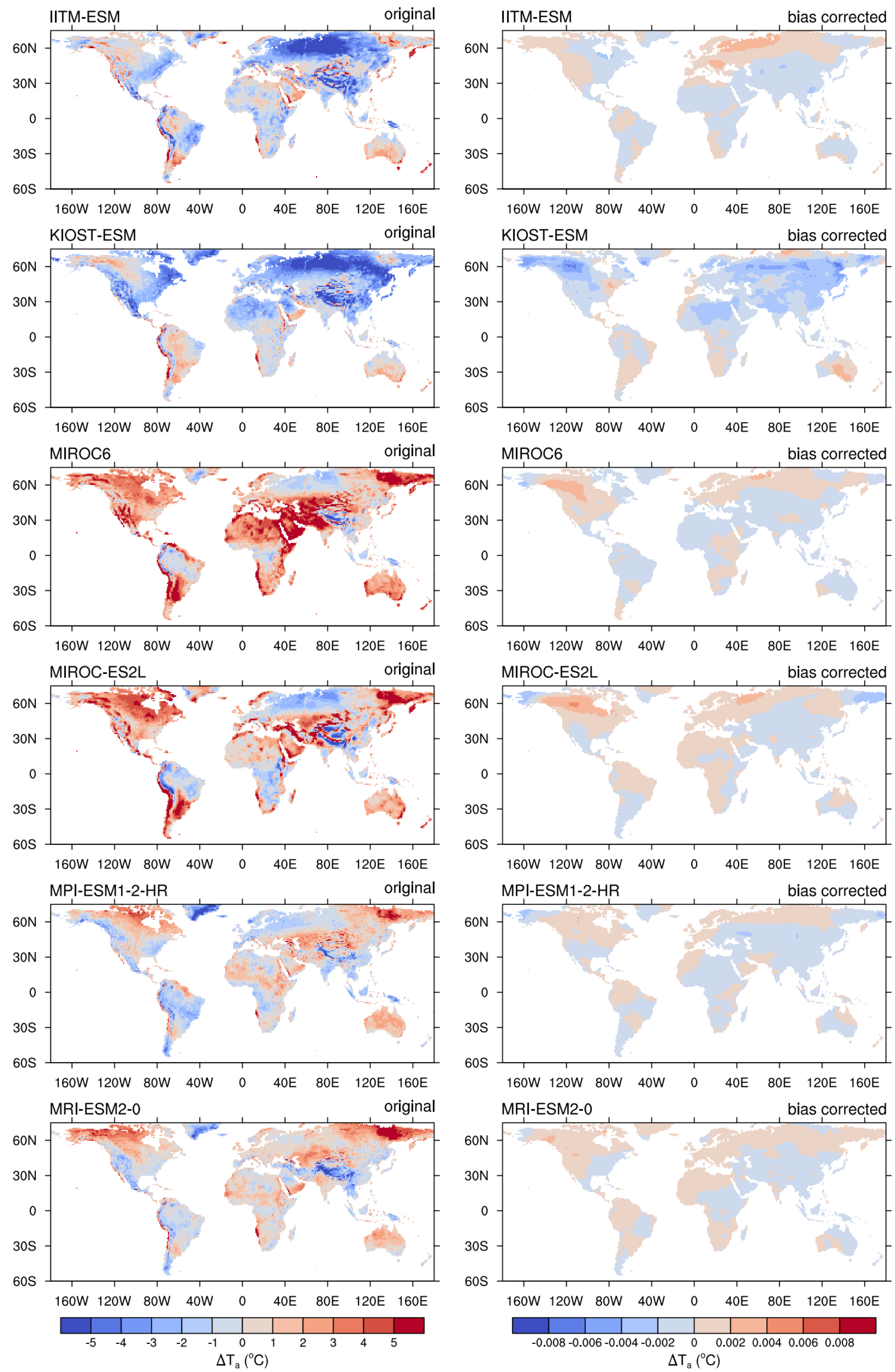

Supplementary Fig. 3: Continued for the rest of CMIP6 models listed in Supplementary Table 2. Bias is reduced to nearly zero for each model after bias and variance correction.

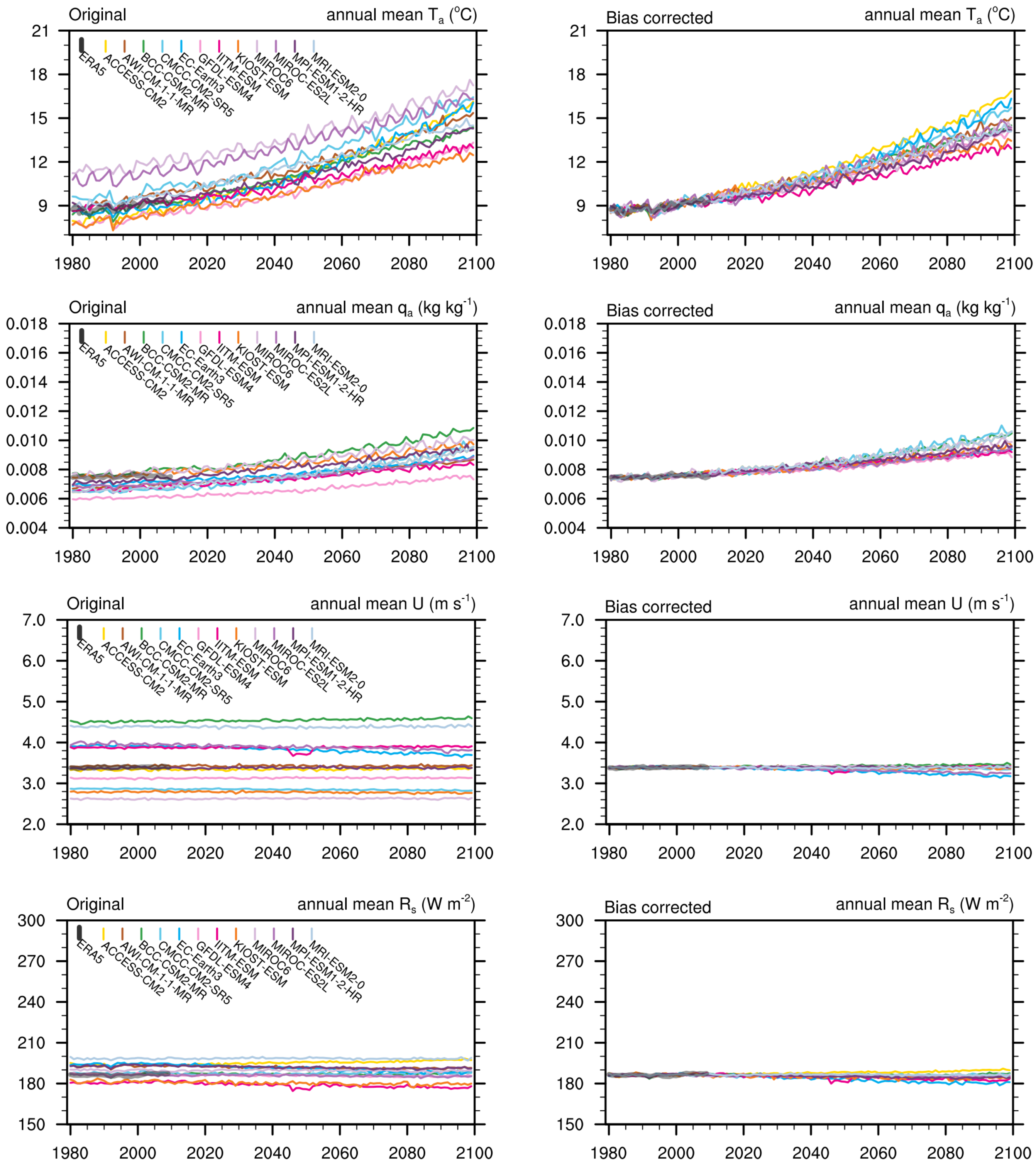

Supplementary Fig. 4: Comparison of global average annual mean CMIP6 variables before (left) and after (right) bias and variance correction with ERA5 (thick grey line) in the period of 1980-2099. This panel shows variables T_a, q_a, U, and R_s (see definition in Supplementary Method 1).

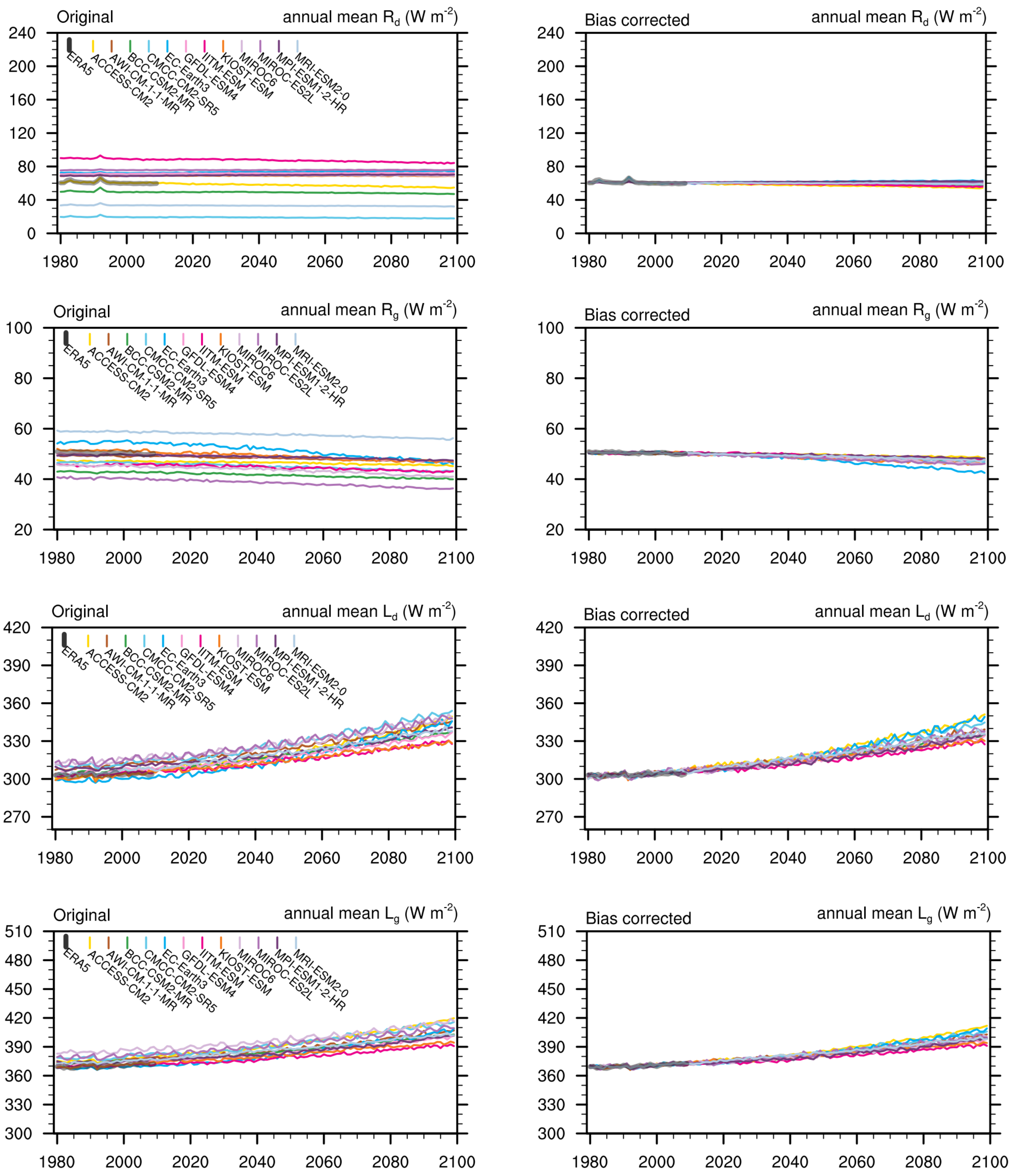

Supplementary Fig. 4: Continued for variables R_d, R_g, L_d, and L_g (annual mean).

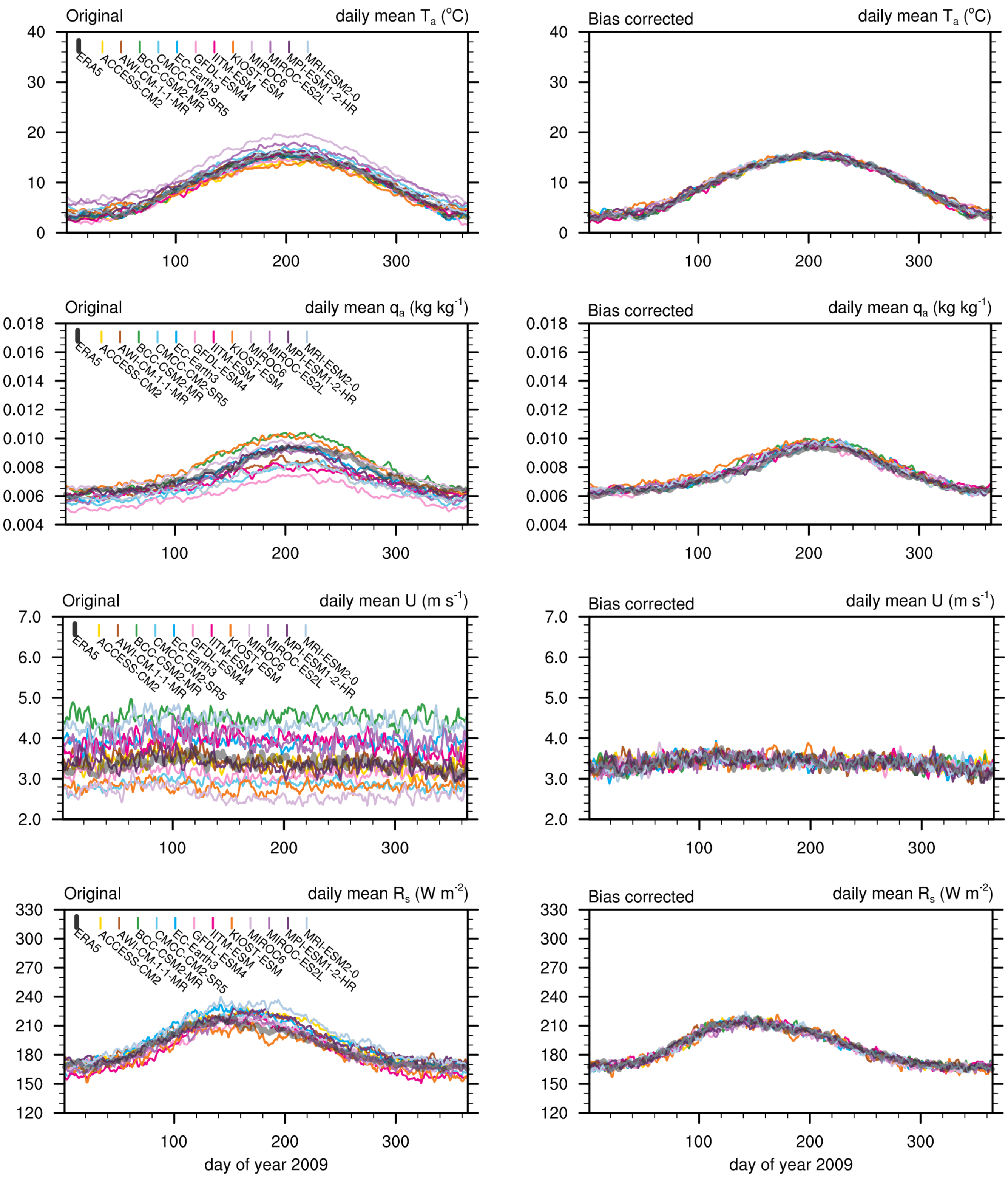

Supplementary Fig. 5: Comparison of global average daily mean values of CMIP6 variables before (left) and after (right) bias and variance correction with ERA5 in the year 2009 as an example. This panel shows the daily mean of variables T_a, q_a, U, and R_s.

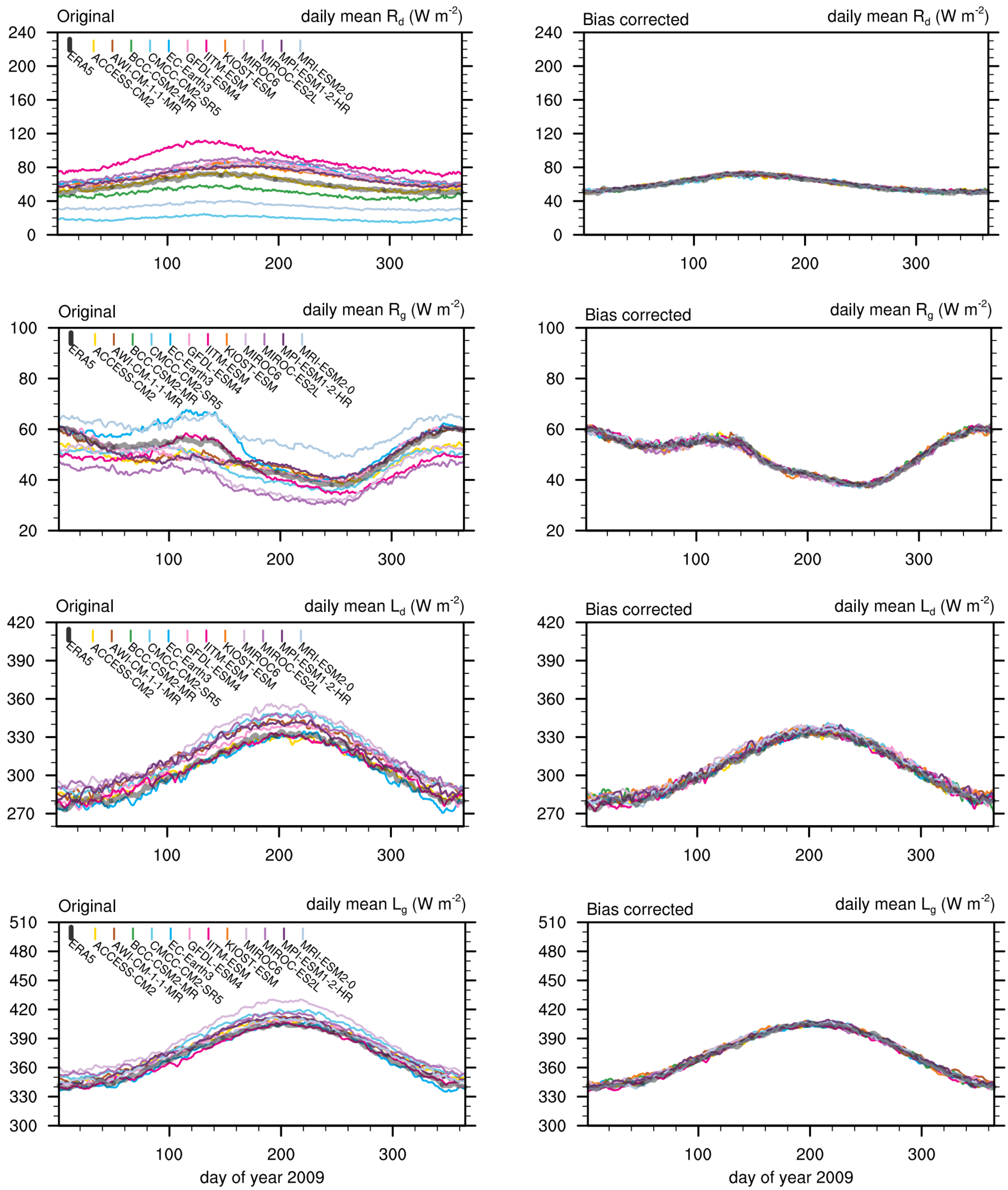

Supplementary Fig. 5: Continued for the daily mean of variables R_d, R_g, L_d, and L_g.

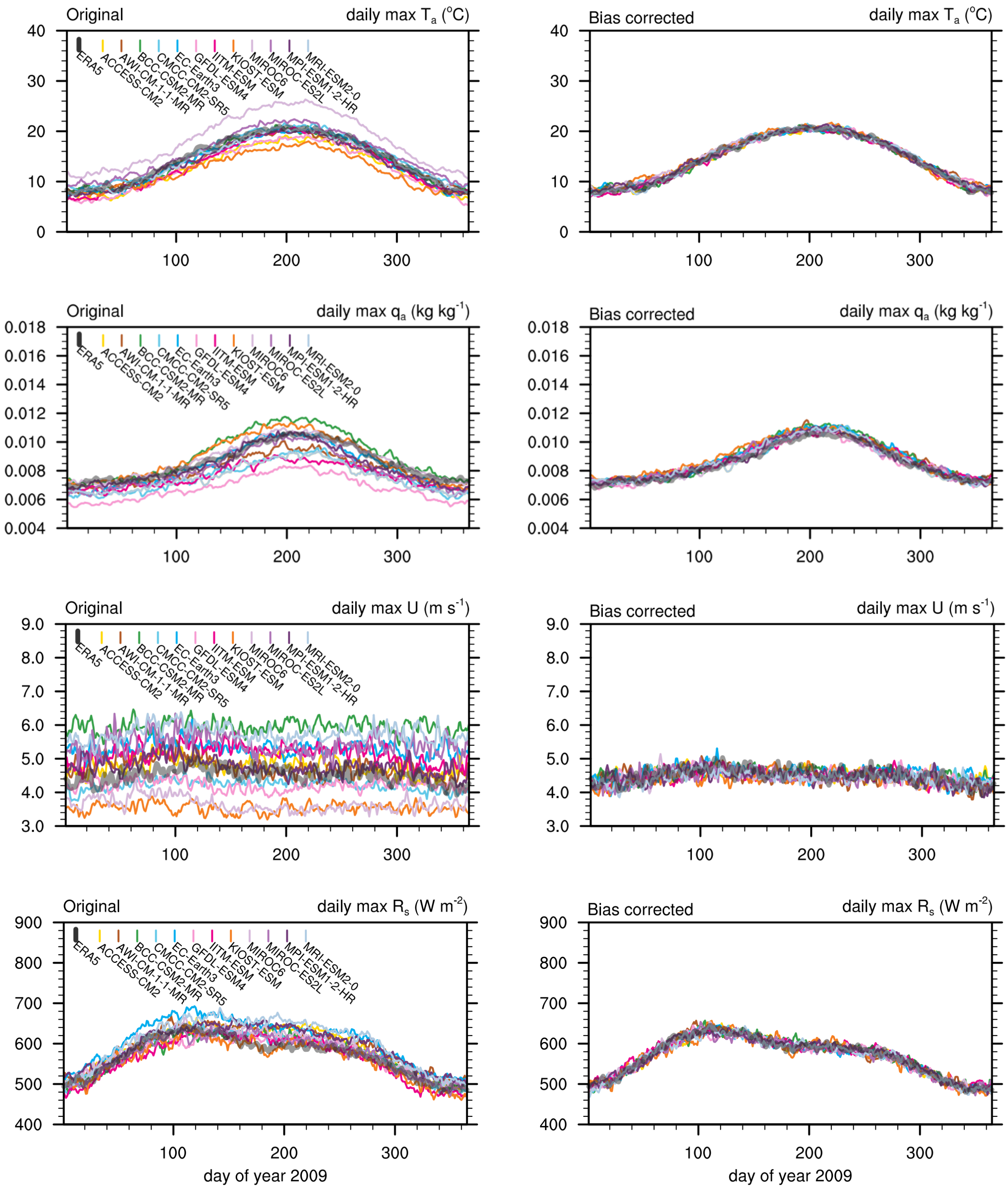

Supplementary Fig. 5: Continued for the daily maximum of variables T_a, q_a, U, and R_s.

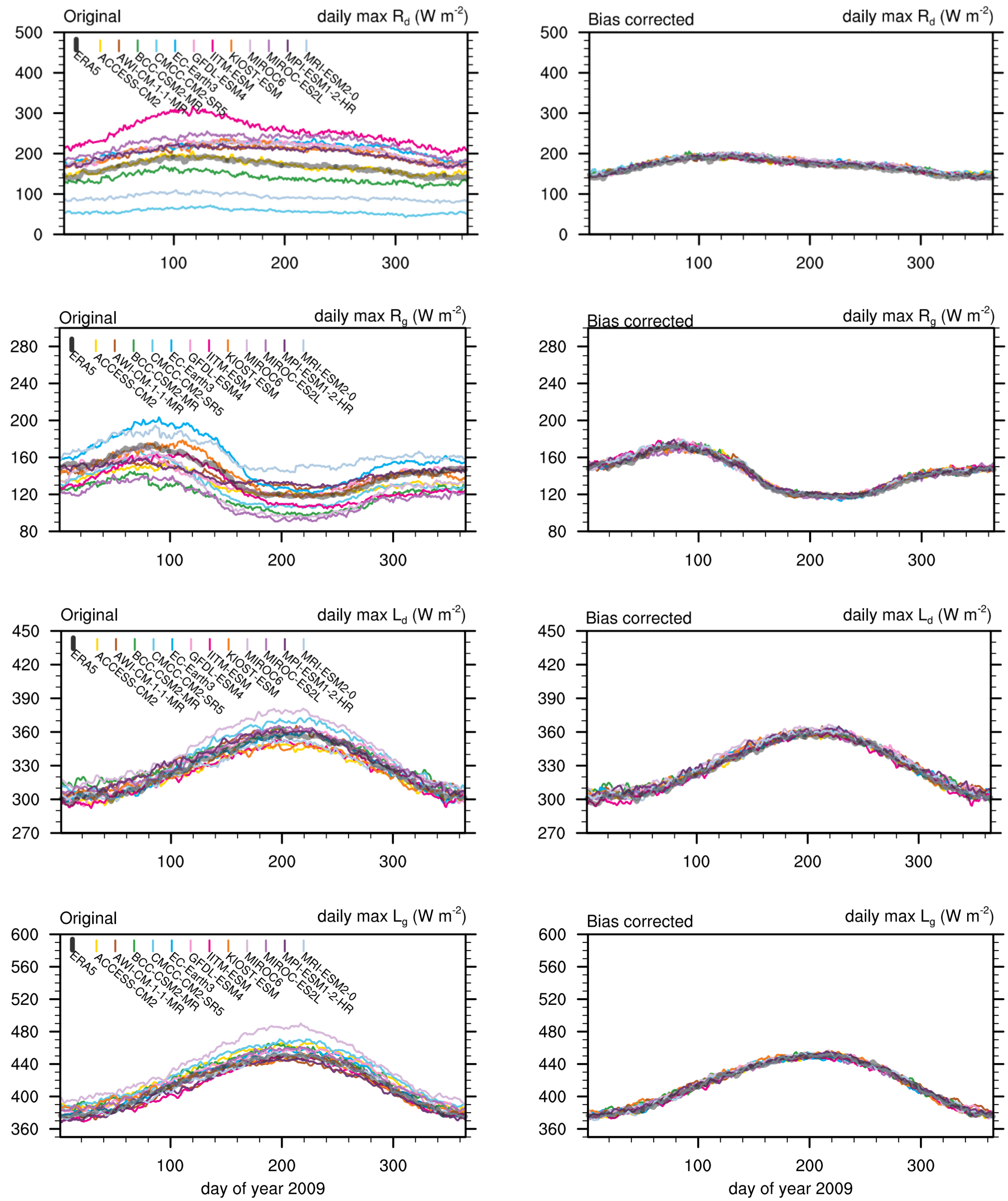

Supplementary Fig. 5: Continued for the daily maximum of variables R_d, R_g, L_d, and L_g.

Supplementary Method 4: Sensitivity analysis

We conduct sensitivity analyses on key input variables (R_s and U) and parameters (T_s, M and h_c) of the model (Eqs. 1-8) by varying one variable (parameter) at a time. Supplementary Fig. 6 shows the sensitivity of total land area projected to experience $G^{day} > 0$ to R_s, U, M, and T_s. To speed up calculations, the sensitivity tests use the concurrent 3-hourly values of the climate variables used to compute annual maximum G^{day} for each grid cell and each year from all twelve CMIP6 models. When testing R_s or U, its global mean is scaled to one value at a time along the gradient shown in the horizontalaxis of Supplementary Fig. 6. When testing M and T_s, constant values at fixed intervals are used. Ensemble statistics are shown for the global warming amount of 2 °C.

Although T_s is treated as a constant value of 36 °C for acclimated and fit individuals in the model, we investigate the sensitivity of our results to this assumption by varying T_s in the range of 33 to 38 °C. Supplementary Fig. 6d shows that the projected impacted area of uncompensable heat stress at 2 °C of global warming shrinks with increasing T_s and expands with decreasing T_s. When T_s = 35 °C is used as input to the model, the global land area projected to experience $G^{day} > 0$ increases by about 107% (63%) under the shade (sun) scenario compared to the default T_s = 36 °C. Under severe heat loads, T_s is often observed to rise above 35 °C before core temperature rises (e.g., when 36 °C $\leq T_a \leq$ 44 °C as shown in Fig. 17B of Fiala et al.[10]). Our validation with the PSU-HEAT experimental data shows that using T_s = 36 °C accurately predicts G around zero across the range of critical environmental conditions (main Fig. 2 and Supplementary Fig. 9). If using T_s = 35 °C, the predicted G would be about 62 W m^{-2} rather than zero. Thus, we use T_s = 36 °C in the model, which is both more accurate and more conservative. Should we use an even higher value for T_s in the model? The body core temperature begins to increase above 37 °C when T_s exceeds 36 °C after 1-h exposure (Fig. 17B of Fiala et al.[10]), which is not tolerable for long. Thus, increasing T_s further is not warranted.

The convective heat transfer coefficient (h_c) is crucial for estimating the sensible and latent heat components of the model (Eqs. 6-8). We conduct a thorough literature review on the h_c coefficient of both forced convection and natural convection for the human body (Supplementary Fig. 7). For forced convection, h_c is normally expressed as an exponential function of wind speed (U) in the form $h_c = bU^n$, where b is typically specified in the range of 7.5 to 15 and n in the range of 0.5 to 0.6 according to measurements on manikins[46–48]. Supplementary Fig. 7 summarizes forced convection functions for h_c from the following works: Bonan[4], Bach (cited in ref.[9]), Fiala[9], Kurazumi[47,49], Ichihara (cited in ref.[46]), Seppänen (cited in ref.[46]), deDear[46], Fanger (cited in ref.[46]), Colin (cited in ref.[9]), Parsons[14], Nishi & Gagge[48,50,51], Mitchell (cited in ref.[47,49]), Kerslake[52], Belding (cited in ref.[53]). A subset of eight studies (refs.[9,14,46,48,49]) also provide values of h_c measured independently for natural convection in the absence of noticeable wind (point marks in bottom left corner of Supplementary Fig. 7), which gives a mean h_c = 3.3 W m^{-2} K^{-1} that is used for natural convection in our model when $U \leq 0.1$ m s^{-1}. We perform an additional test on the sensitivity of our results to the choice of h_c function by recalculating the results using three alternative functions: Bonan (same as Bach), deDear, and Nishi & Gagge (Supplementary Fig. 8). The Bonan equation is derived from their original expression for aerodynamic conductance $g_{\mathrm{a}} = 1/(200(d/U)^{0.5})$ (ref.[4]) according to $h_{\mathrm{c}} = \rho c_{\mathrm{p}} g_{\mathrm{a}}$, where d = 0.15 (m) is the significant diameter of the entire body (ref.[2]), ρ is air density and c_{p} is defined in Supplementary Table 1. Supplementary Fig. 8 shows that using a h_c function with a steeper slope (e.g., Fiala's in Supplementary Fig. 7) results in lower G and smaller impacted area with $G^{\mathrm{day}} > 0$, whereas a flatter h_c function such as deDear's or Nishi & Gagge increases the projected risk of uncompensable heat stress. Our model uses Fiala's h_c function from figure 3 in ref.[9]. This choice gives a relatively conservative projection of uncompensable heat stress impacts as shown in Supplementary Fig. 8. Given that a large volume of thermophysiological studies we surveyed show a highly dispersed distribution of the h_c function (in relation to U) and G is sensitive to this function (imposing a sweating limit in Eq. 8 of the model has substantially reduced the sensitivity in Supplementary Fig. 8), further studies are warranted to constrain the convective heat transfer process around the human body.

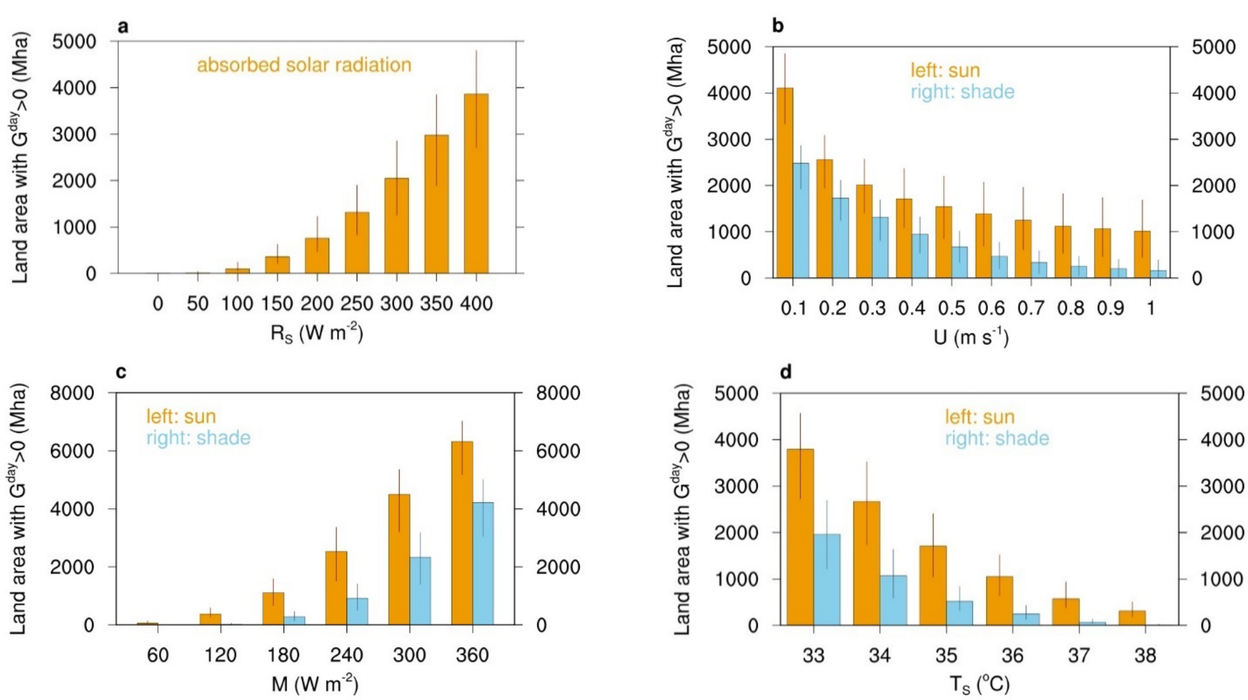

Supplementary Fig. 6: Sensitivity of land area projected to experience $G^{day} > 0$ at 2 °C of warming to key parameters or input variables in the energy balance model. a Solar radiation (R_s, here showing the absorbed R_s after sun angle correction); **b** Wind speed (U); **c** Metabolic heat (M); **d** Skin temperature (T_s). The bars denote ensemble averages, and the error bars indicate the 25th-75th percentile interval. Here the impacted land area is not masked by water collection or agricultural population data.

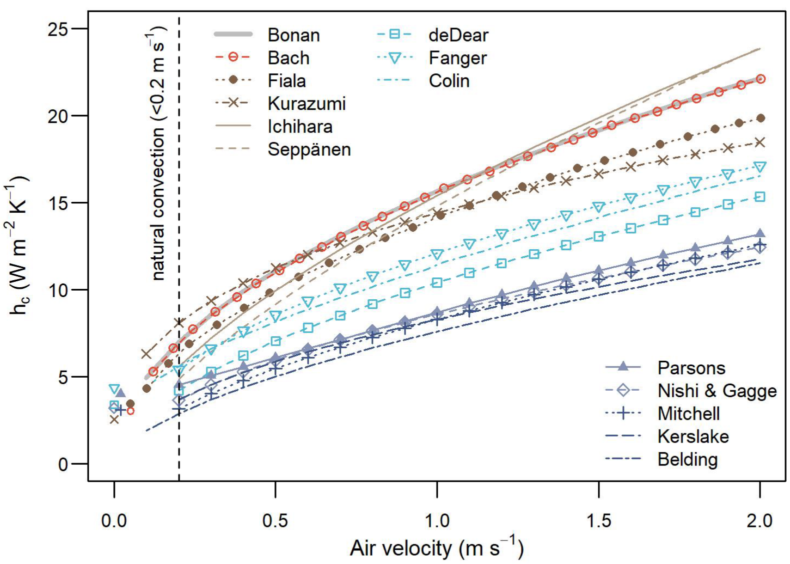

Supplementary Fig. 7: Summary of the convective heat transfer coefficient (h_c) for a human body as a function of air velocity from published literature. Lines indicate measured h_c for forced convection. Point marks in the left bottom indicate h_c for natural convection measured in the absence of noticeable wind from a subset of studies with the same point marks in the legend.

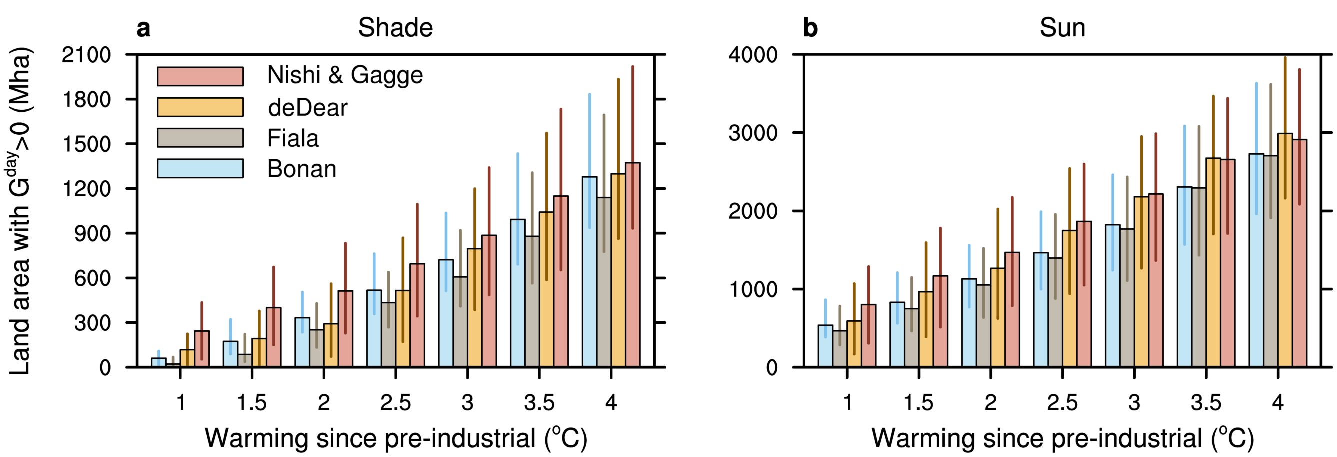

Supplementary Fig. 8: Sensitivity of land area projected to experience $G^{day} > 0$ at different warming levels to the choice of convective heat transfer coefficient (h_c) function. a Shade scenario; **b** Sun scenario. Four representative functions from Supplementary Fig. 7 are compared: Bonan ($h_c = 15.6U^{0.5}$), Fiala ($h_c = 14.1U^{0.5}$) as in Eq. 6, deDear ($h_c = 10.4U^{0.56}$), and Nishi & Gagge ($h_c = 8.6U^{0.531}$). The bars denote ensemble median, and the error bars indicate the 25-75th percentiles. Here the impacted land area is not masked by water collection or agricultural population data.

The following are supplementary figures cited in the main text.

Supplementary Figures 9-27

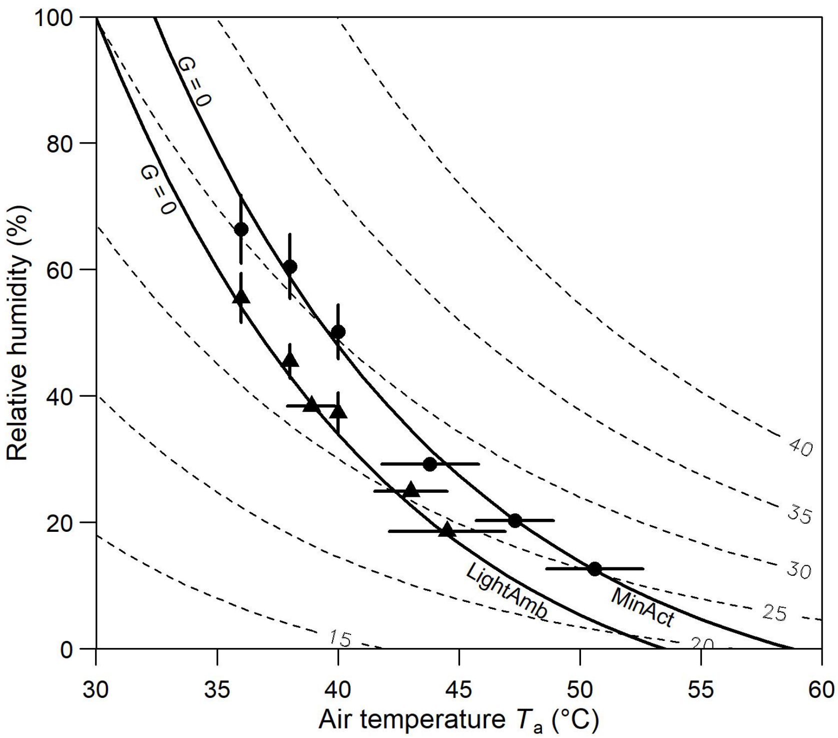

Supplementary Fig. 9: Same as the main Fig. 2 but with relative humidity (RH) on the Y-axis.

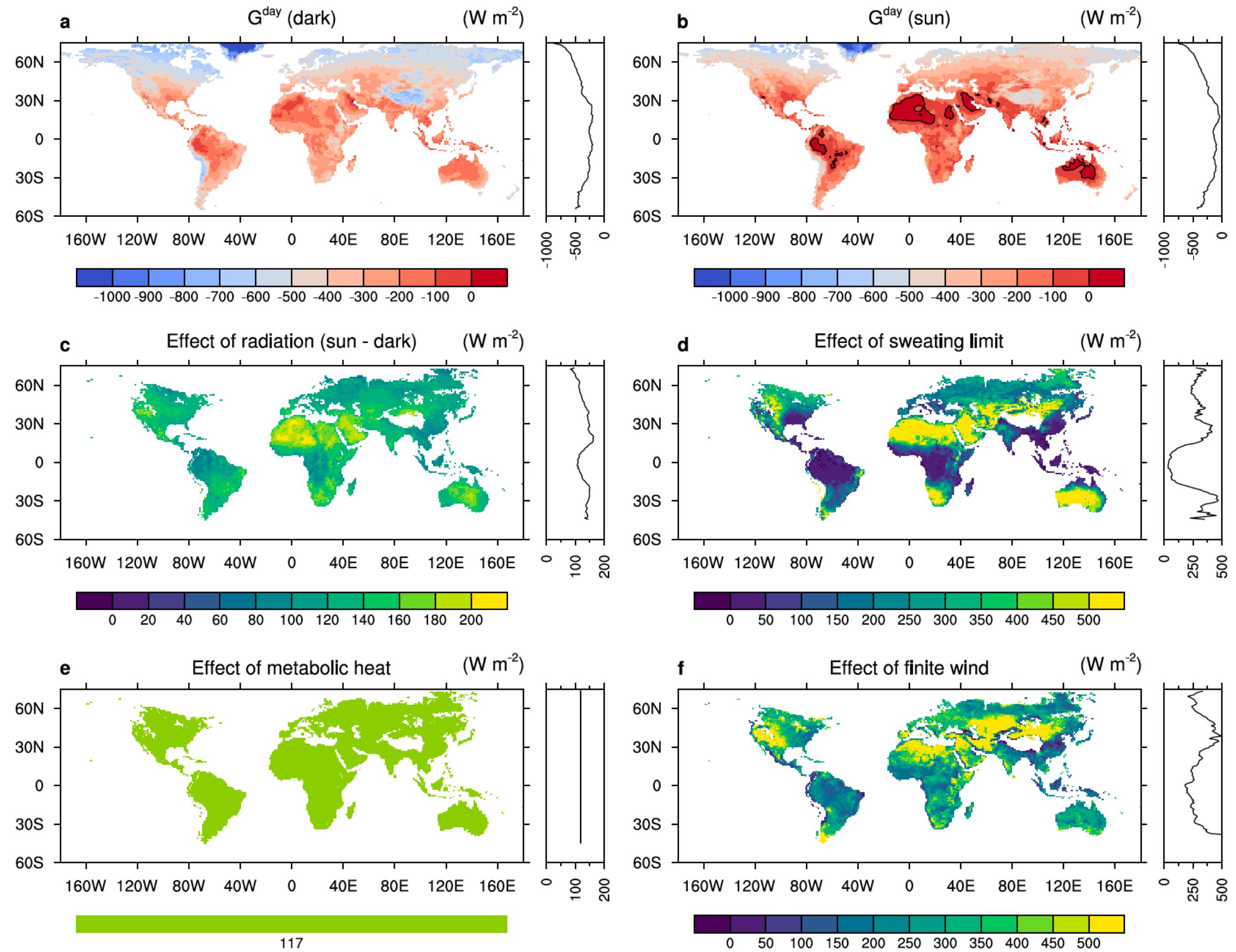

Supplementary Fig. 10: Spatial distribution of G^{day} under different radiation scenarios and decomposition of the effects of different factors on G^{day}. Multi-model ensemble median of annual maximum G^{day} under the dark (**a**) and sun (**b**) scenarios, and the individual effects of solar radiation (sun – dark scenario, **c**) sweating limit (dark – dark* scenario, **d**) extra metabolic heat (dark* – dark**, i.e., 176 – 59 W m^{-2}, **e**) and finite wind speed (dark** – $G_{\mathrm{TW}}{}^{\mathrm{day}}$, **f**) at 2 °C of global warming. Areas with daily mean T_{a} < 20 °C are masked out in **c-f** to focus on warm conditions.

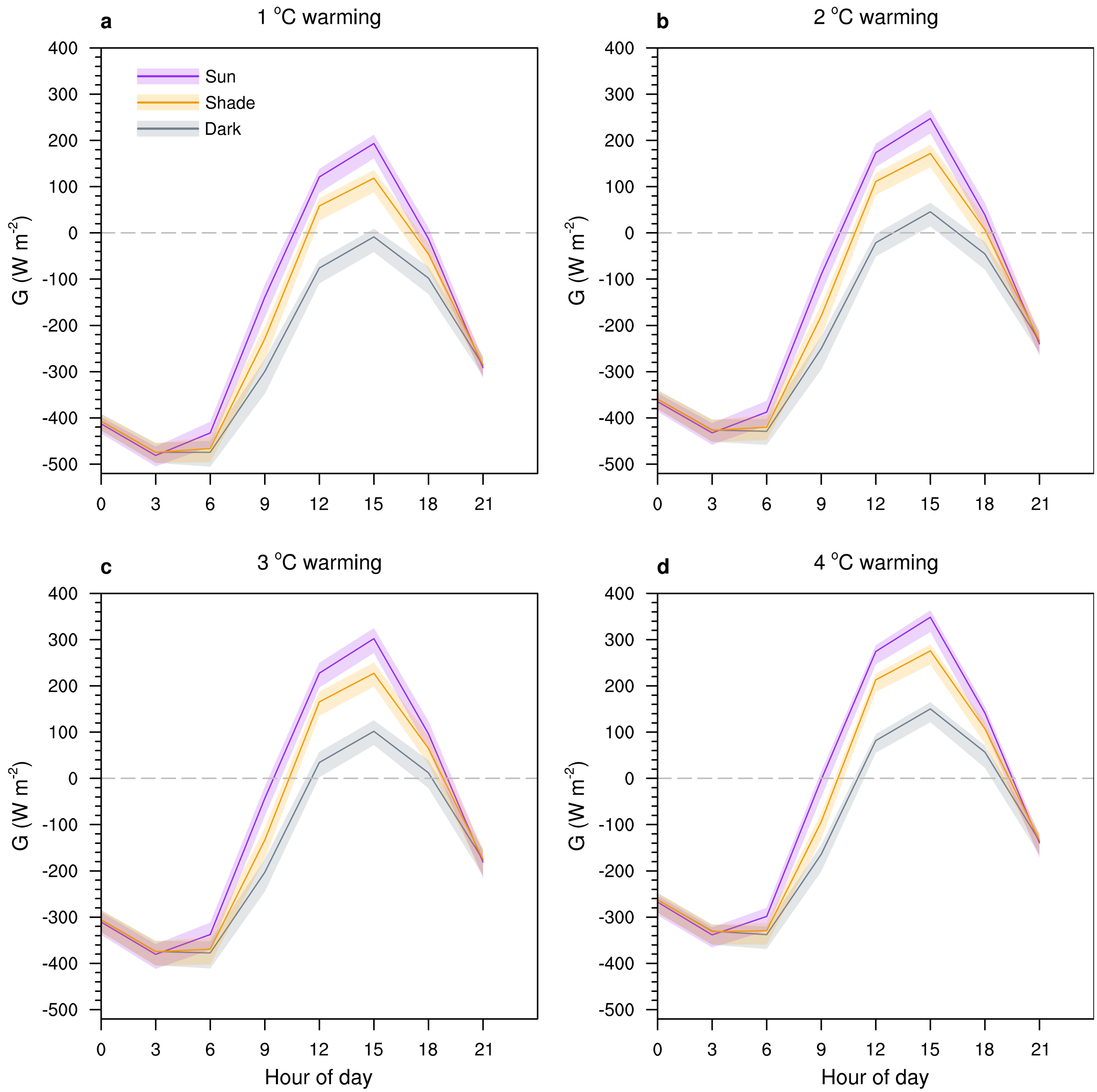

Supplementary Fig. 11: Same as main Fig. 7 but for the subpopulation engaged in farming.

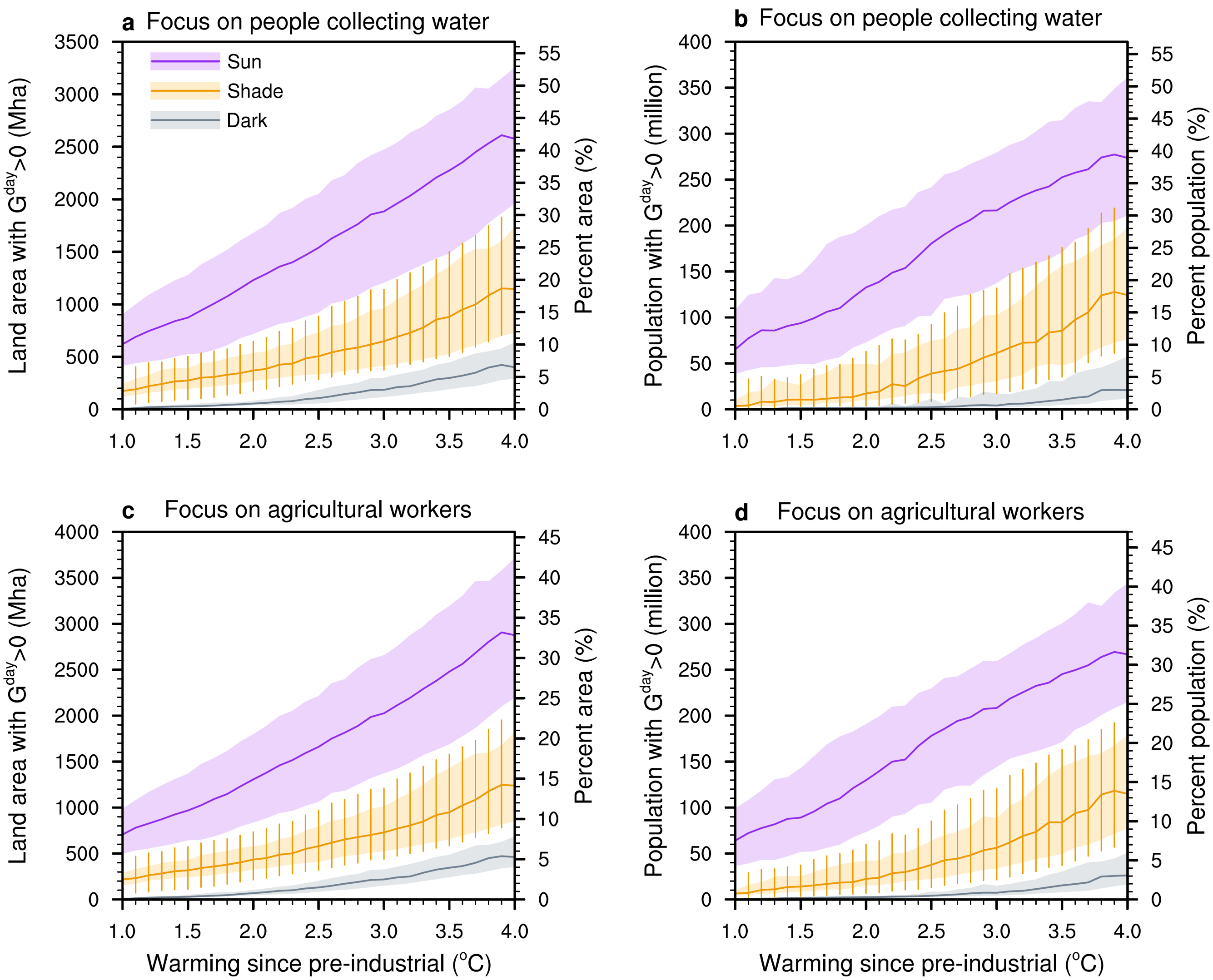

Supplementary Fig. 12: Same as main Fig. 5 but for non-acclimated persons. Non-acclimated persons are modelled with a maximum sweating capacity of 400 W m^{-2} (corresponding to 1 litre of sweat production per hour), according to the ISO 7933:2023 standard[15].

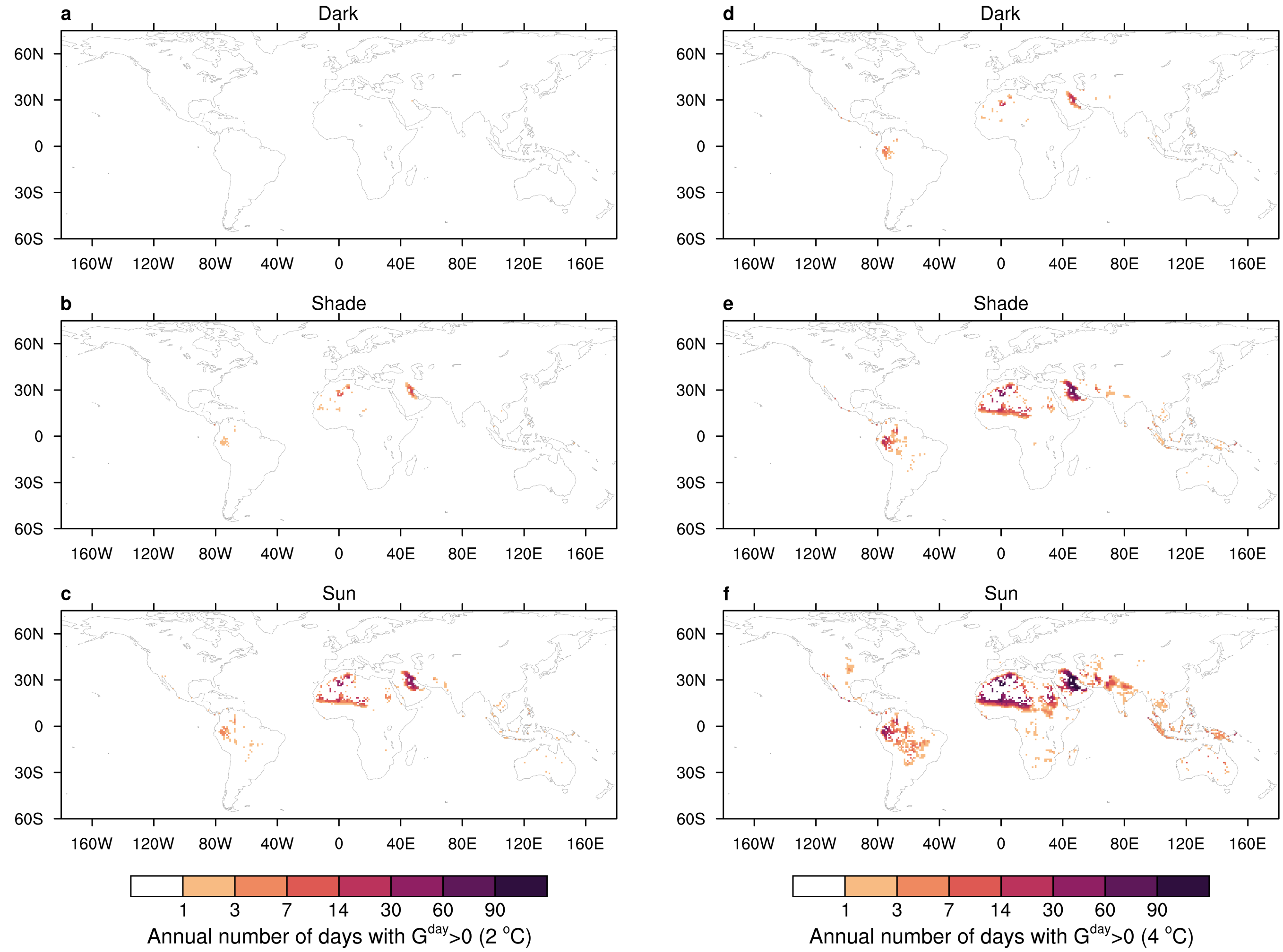

Supplementary Fig. 13: Projected occurrence frequency of uncompensable heat stress under different radiation and warming scenarios. Ensemble median projected annual number of days with $G^{\mathrm{day}} > 0$ W m^{-2} under dark (**a/d**), shade (**b/e**) and sun (**c/f**) scenarios. Panel **a-c** for 2 °C warming and **d-f** for 4 °C warming relative to preindustrial level. The plots are masked by the population distribution of agricultural workers shown in Supplementary Fig. 2b to focus on populated regions.

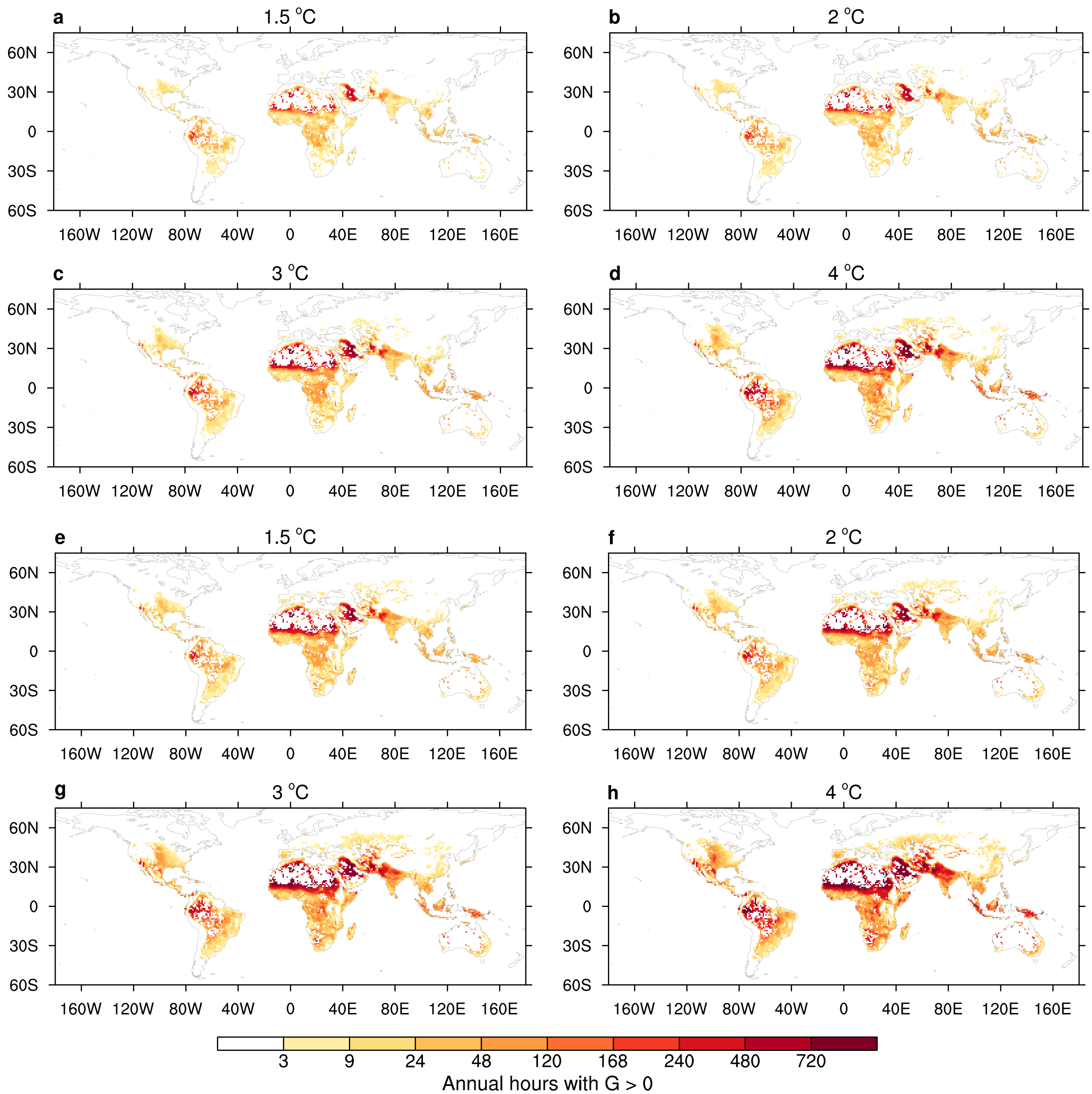

Supplementary Fig. 14: Projected annual hours of uncompensable heat stress outdoors under different radiation and warming scenarios. Annual cumulative hours with $G > 0$ under (**a/e**) 1.5 °C, (**b/f**) 2 °C, (**c/g**) 3 °C, and (**d/h**) 4 °C of warming for outdoor shade **(a-d)** and sun **(e-h)** scenarios. The outdoor scenarios consider people doing moderate work (M = 176 W m^{-2}), with maximum sweating capacity of 500 W m^{-2} and use dynamic wind speeds and other climate variables as inputs (main Table 1). This figure is masked by the population distribution of agricultural workers shown in Supplementary Fig. 2b to focus on populated regions.

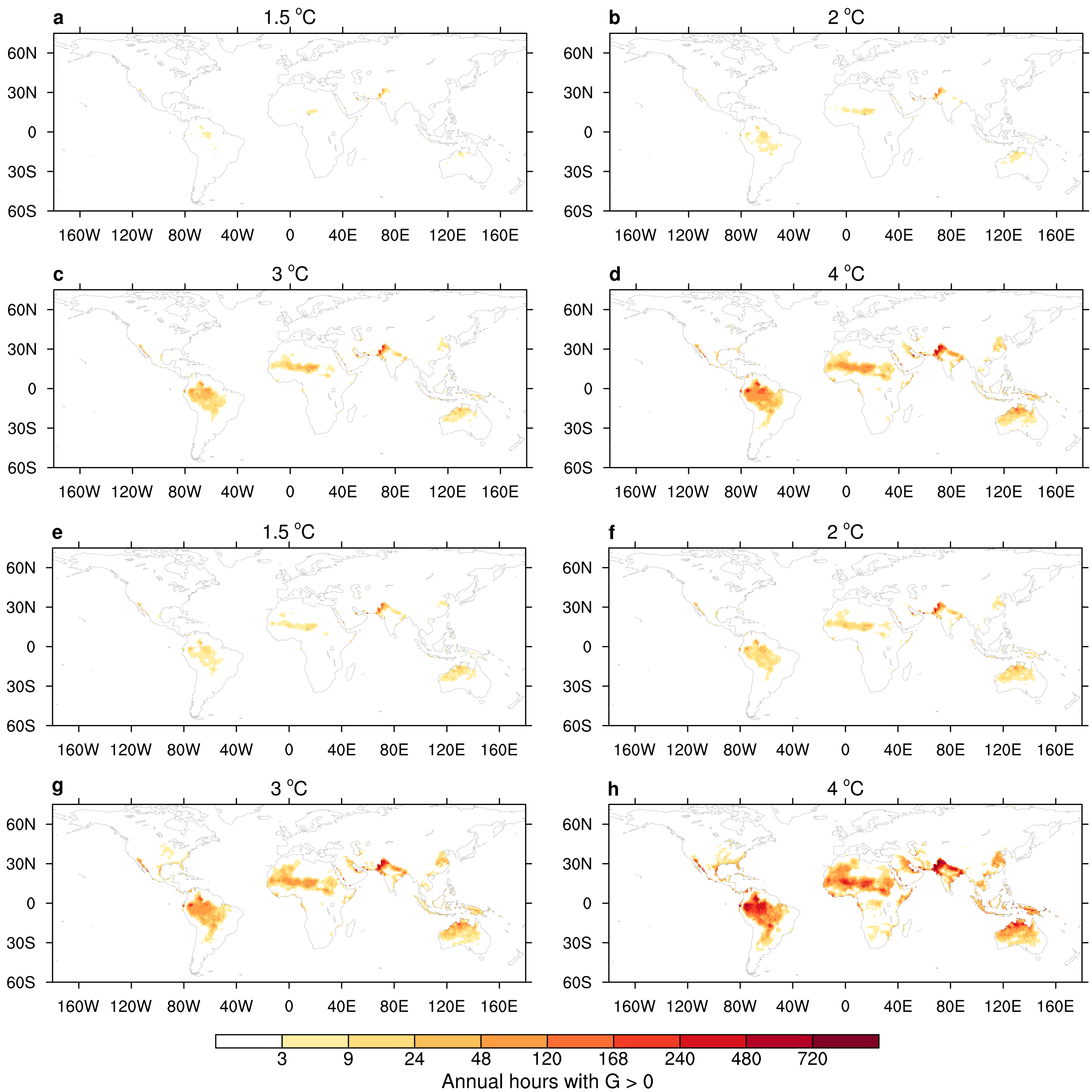

Supplementary Fig. 15: Projected annual hours of uncompensable heat stress indoors at different warming levels. Annual cumulative hours with $G > 0$ under (**a/e**) 1.5 °C, (**b/f**) 2 °C, (**c/g**) 3 °C, and (**d/h**) 4 °C of warming relative to preindustrial level. Panel **a-d** for people at rest ($M = 59$ W m^{-2}) indoors with zero solar radiation and minimal wind speed ($U = 0.1$ m s^{-1}); panel **e-h** for people cycling an ergometer with zero solar radiation but higher metabolic heat $M = 83$ W m^{-2} as in ref.[54,55].

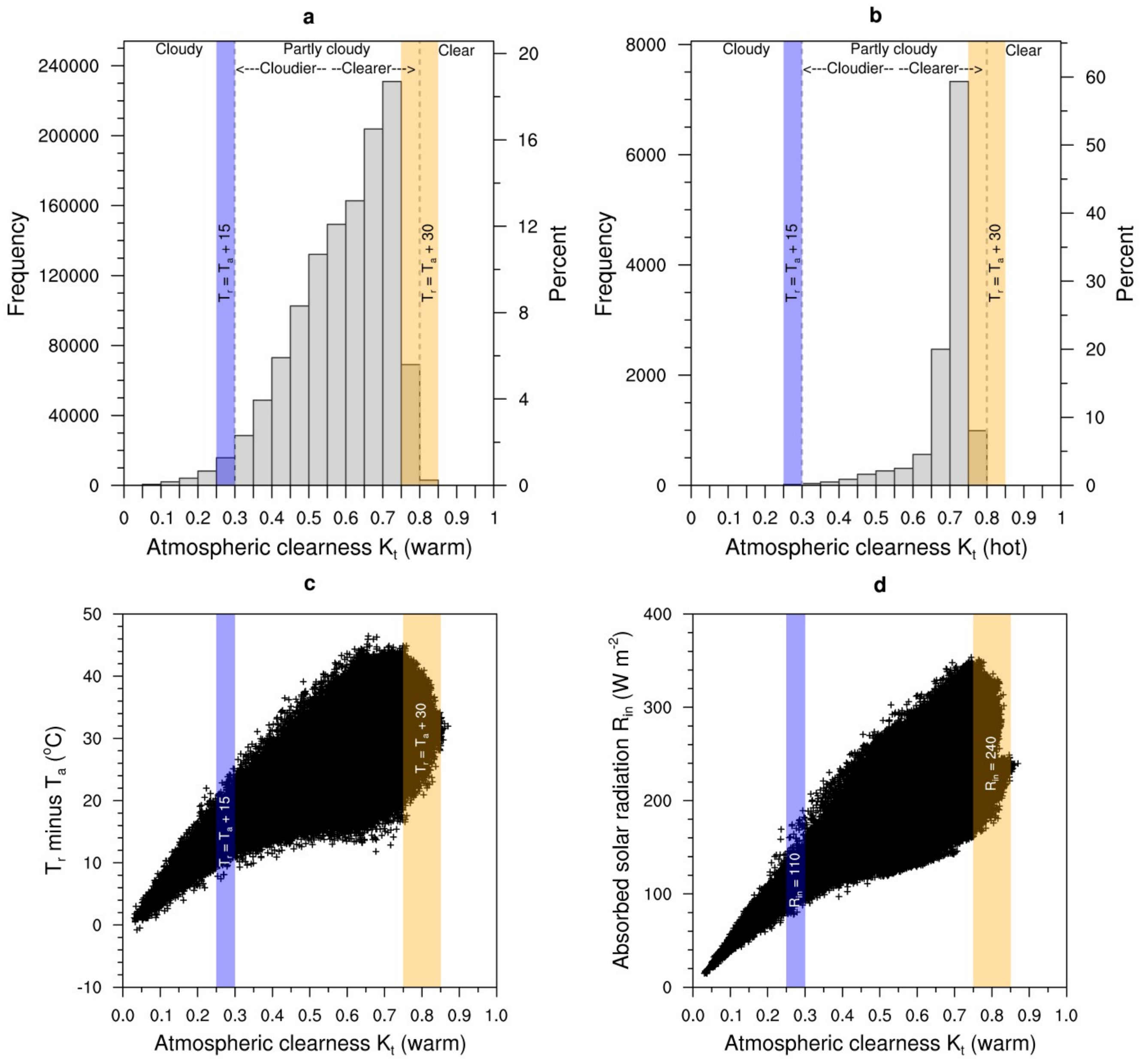

Supplementary Fig. 16: Distribution of midday atmospheric clearness index (K_t), mean radiant temperature (T_r) and absorbed incident solar radiation (R_{in}) by a person in warm and hot conditions according to 3-hourly ERA5 reanalysis data for an example year (2009). a-b Histograms of K_t in warm conditions with daily mean T_a > 25 °C (**a**) and in hot conditions represented by the top 1% of G^{day} (**b**; here G^{day} is computed without solar radiation to examine its distribution under any weather condition). **c-d** Scatterplots of the difference between T_r and T_a (**c**) and R_{in} (**d**) as a function of K_t in warm conditions. See main Methods section "Model validation and cross-comparison" for details about the calculation of K_t, R_{in} and T_r. The grey dashed lines in a-b divide sky conditions to cloudy ($K_t < 0.3$), partly cloudy ($0.3 \leq K_t \leq 0.8$) and clear ($K_t > 0.8$) according to the observed range of K_t under three sky conditions[29]. The blue shaded region in **a-d** denotes the sky conditions ($0.25 < K_t < 0.3$) under which the mean of $T_r - T_a$ is about 15 °C as shown in **c**, which was observed at midday under partly cloudy conditions from ref.[56] that was used for the "sun scenario" by ref.[57]. The orange shaded region in **a-d** denotes the sky conditions ($0.75 < K_t < 0.85$) corresponding closely to the observed $T_r - T_a = 30$ at midday under sunny conditions from ref.[56].

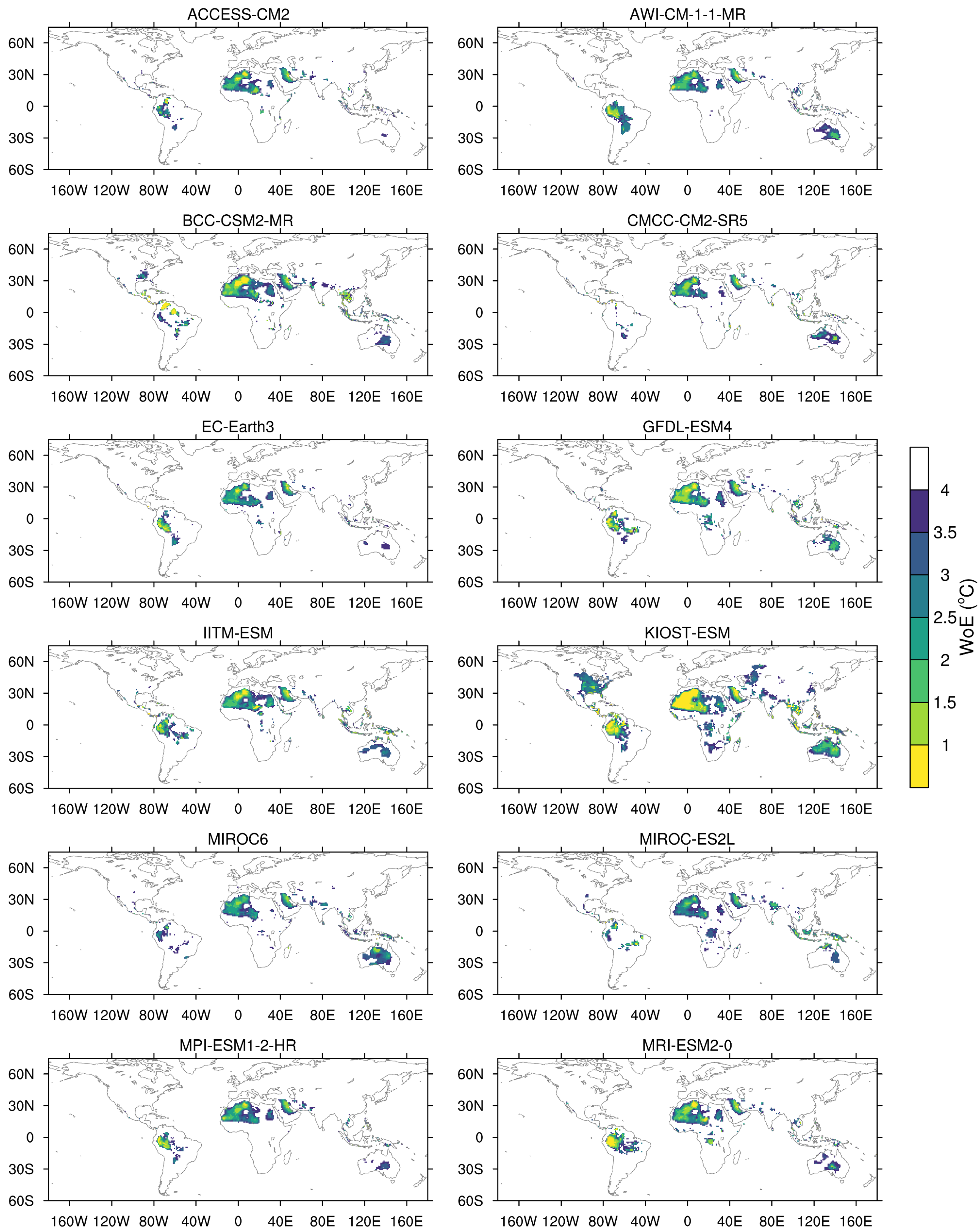

Supplementary Fig. 17: WoE under the shade scenario for each model used to compute the ensemble median in main Fig. 4b.

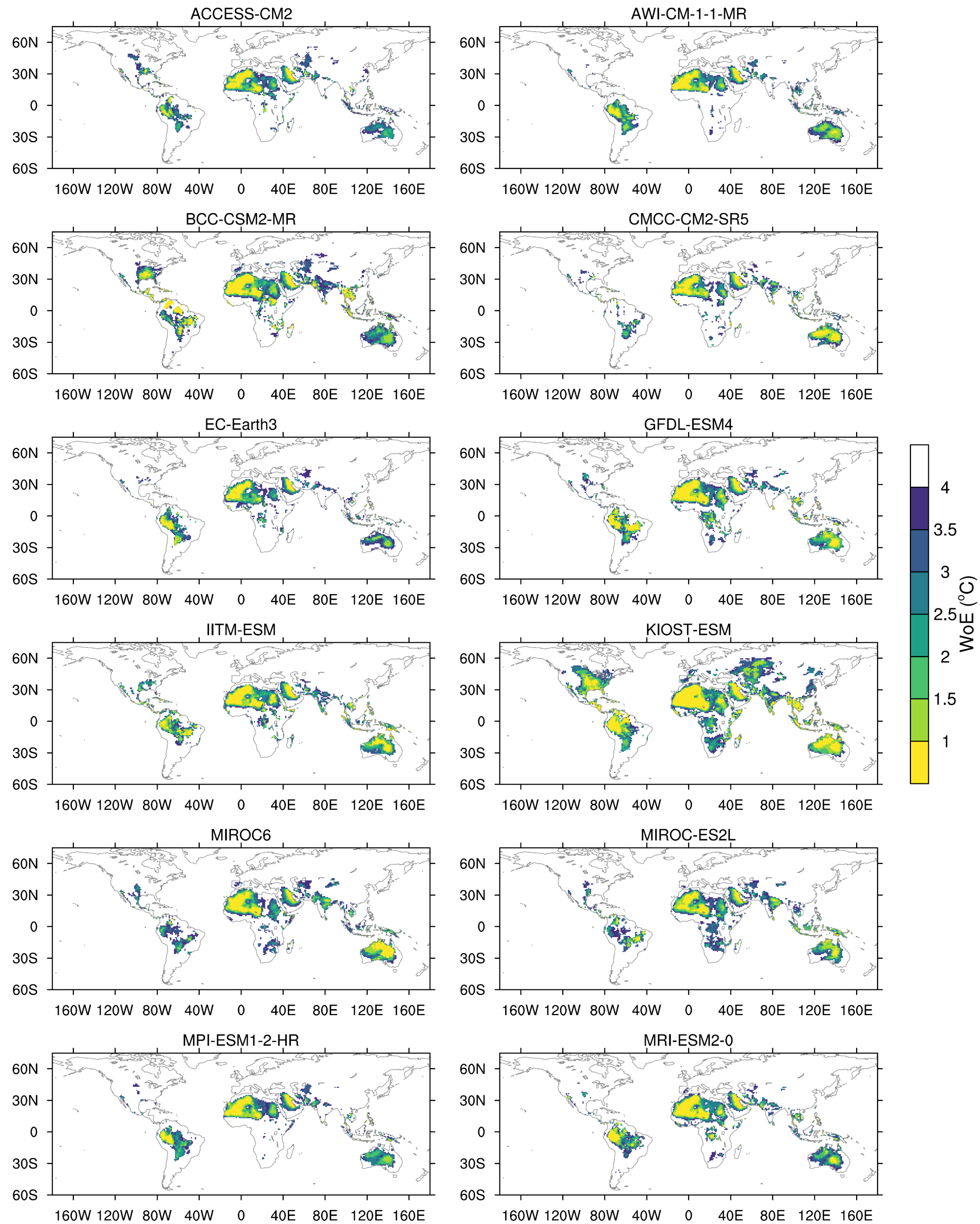

Supplementary Fig. 18: WoE under the sun scenario for each model used to compute the ensemble median in main Fig. 4c.

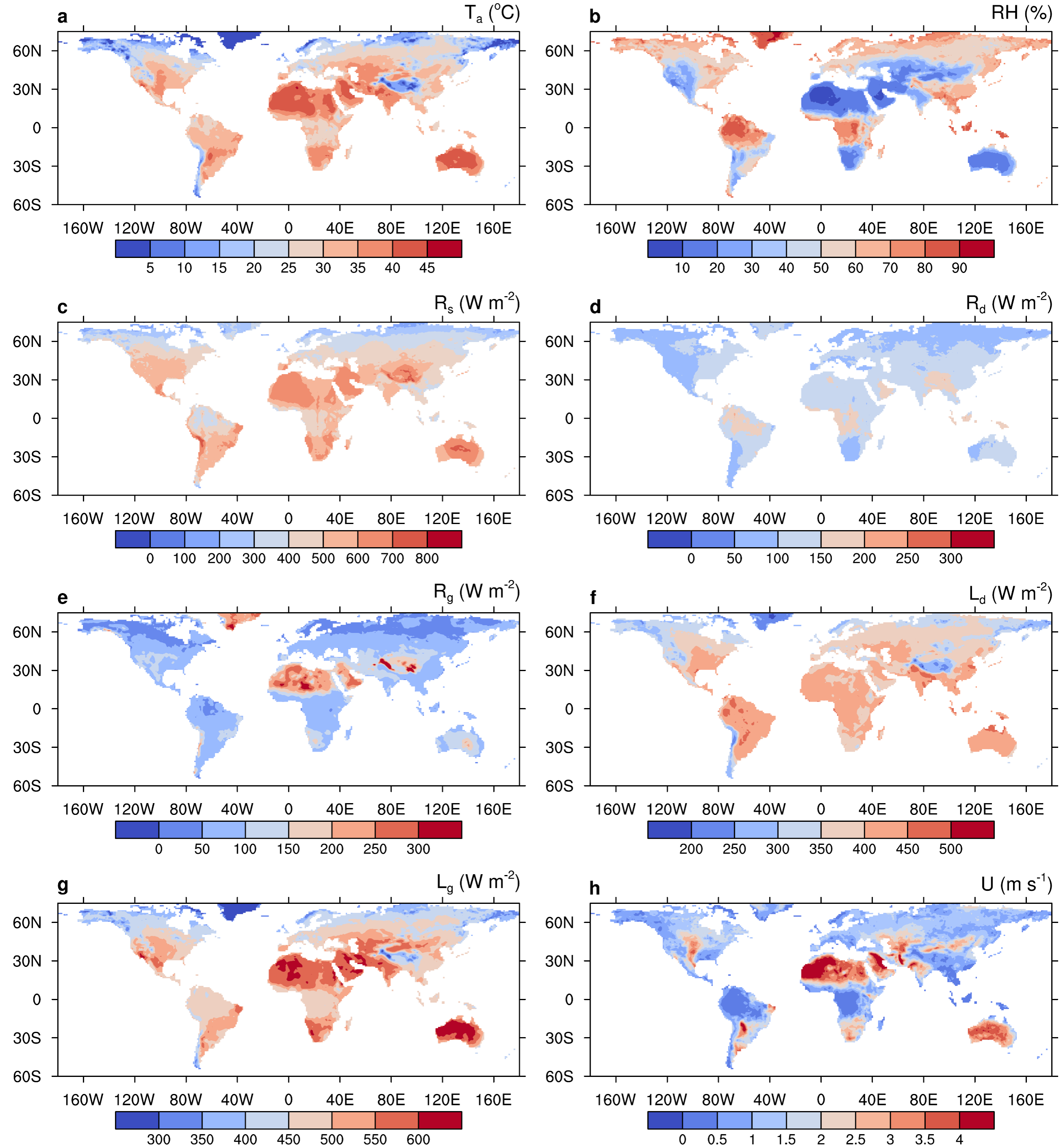

Supplementary Fig. 19: Concurrent daytime mean values of the climate variables used to calculate annual maximum G^{day} under the sun scenario at 2 °C warming. Surface air temperature (T_a; **a**), relative humidity (RH; **b**), full solar radiation (R_s; **c**), diffuse radiation (R_d; **d**), reflected solar radiation from the ground (R_g; **e**), atmosphere downwelling longwave radiation (L_d; **f**), upwelling longwave radiation from the ground (L_g; **g**), and wind speed (U; **h**). A reverse-search algorithm is used to find the concurrent values of these variables when annual maximum G^{day} is identified at each land grid cell. Only the ensemble median values are shown in the maps.

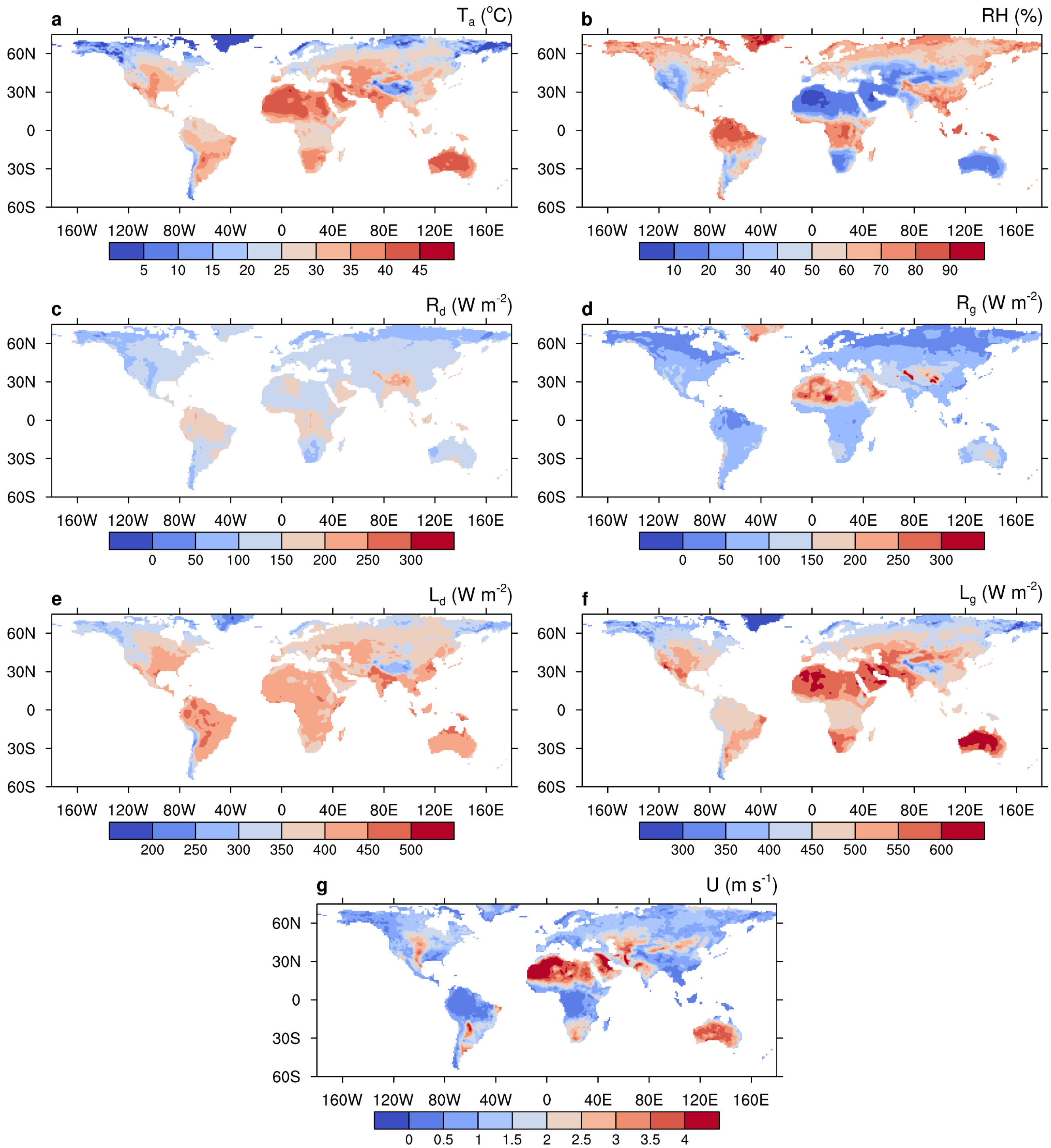

Supplementary Fig. 20: Same as Supplementary Fig. 19 but for the shade scenario, which uses only R_d, R_g, L_d, and L_g for radiation input. See main Table 1 for the definition of the shade scenario.

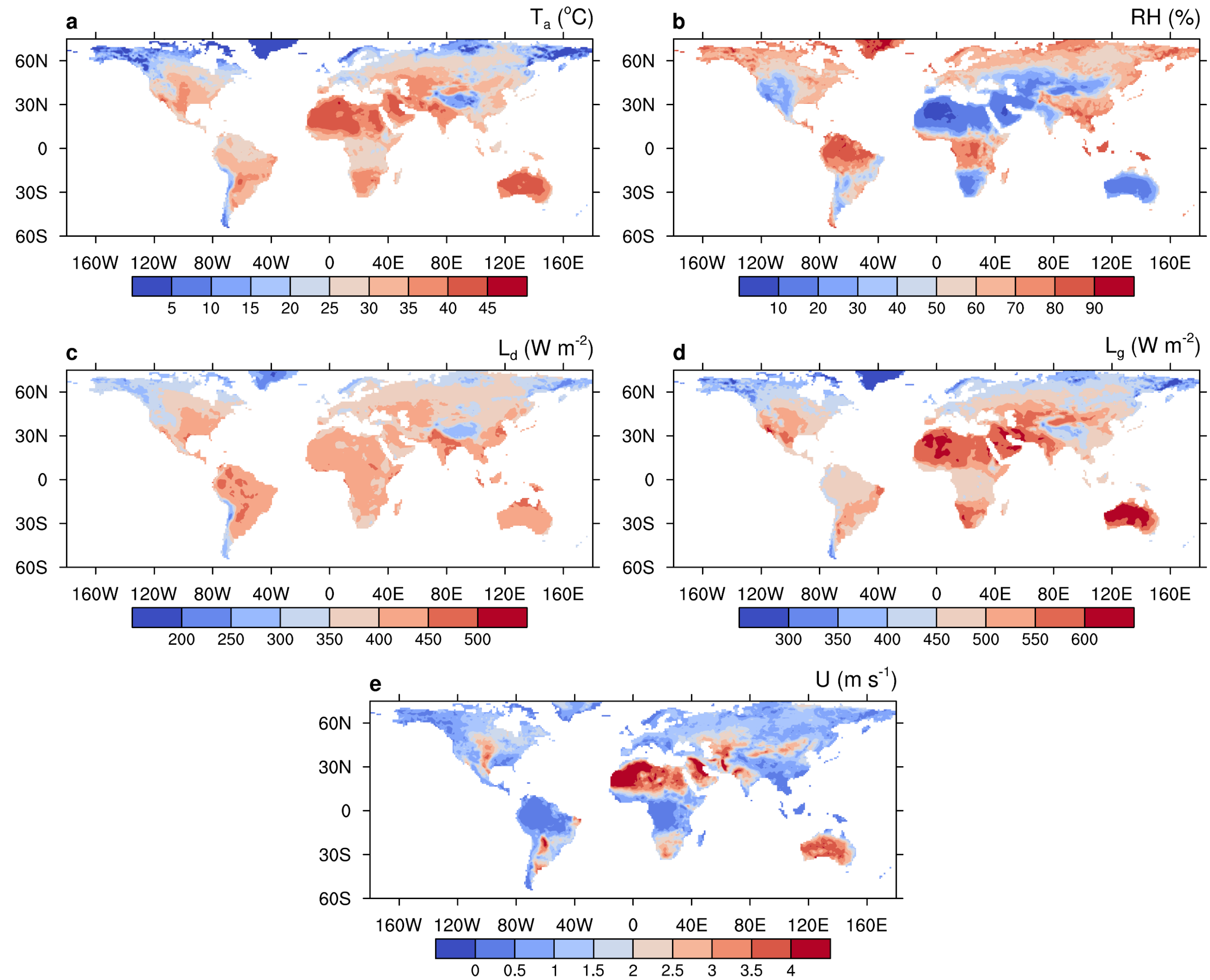

Supplementary Fig. 21: Same as Supplementary Fig. 19 but for the dark scenario, which uses only L_d and L_g for longwave radiation input. See main Table 1 for the definition of the dark scenario.

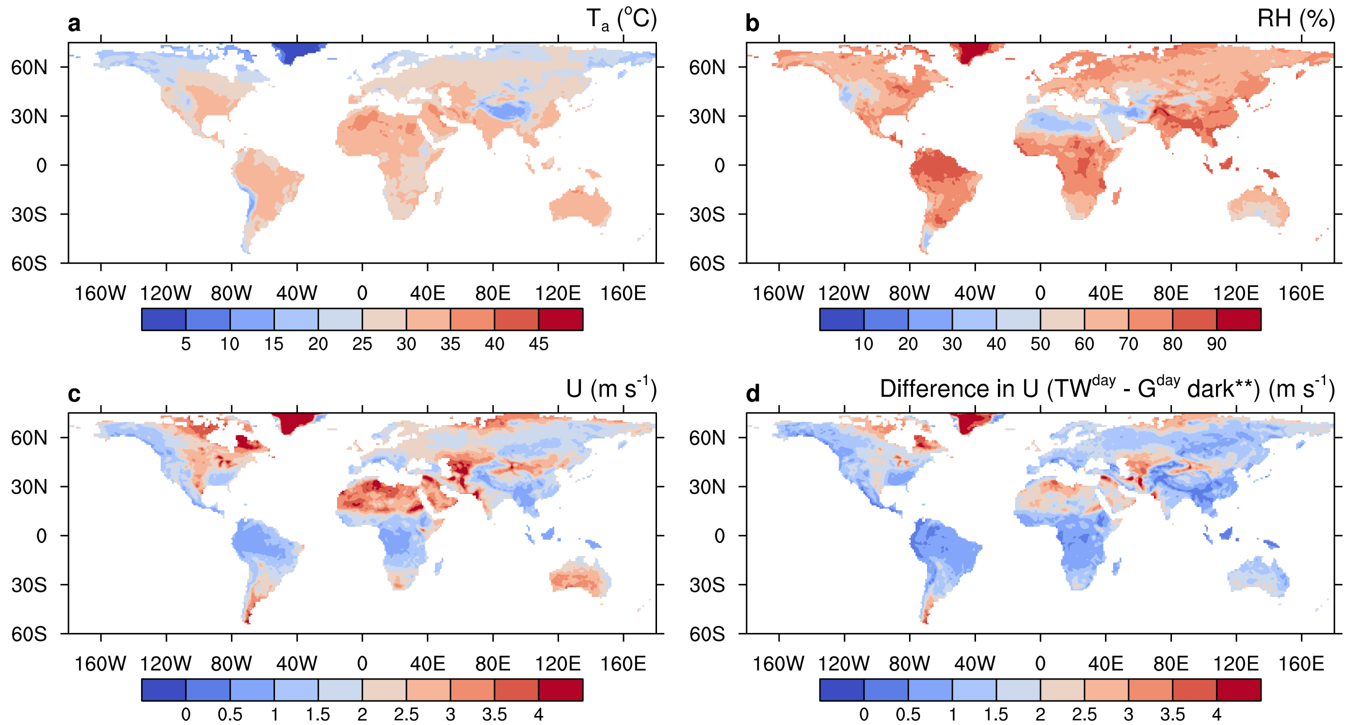

Supplementary Fig. 22: Same as Supplementary Fig. 19 but for climate variables concurrent with annual maximum $T_W$$^{\mathbf{day}}$. Although only T_a (**a**) and RH (**b**) are involved in the calculation of T_W, U (**c**) is used in Eq. 14 to convert T_W^{day} to G_{TW}^{day}. The difference between U concurrent with T_W^{day} and U concurrent with G^{day} (dark**) is shown in **d**. Wind speeds at the time of peak T_W are mostly higher than those of peak G under the dark** scenario. See main Table 1 for the definition of the dark** scenario.

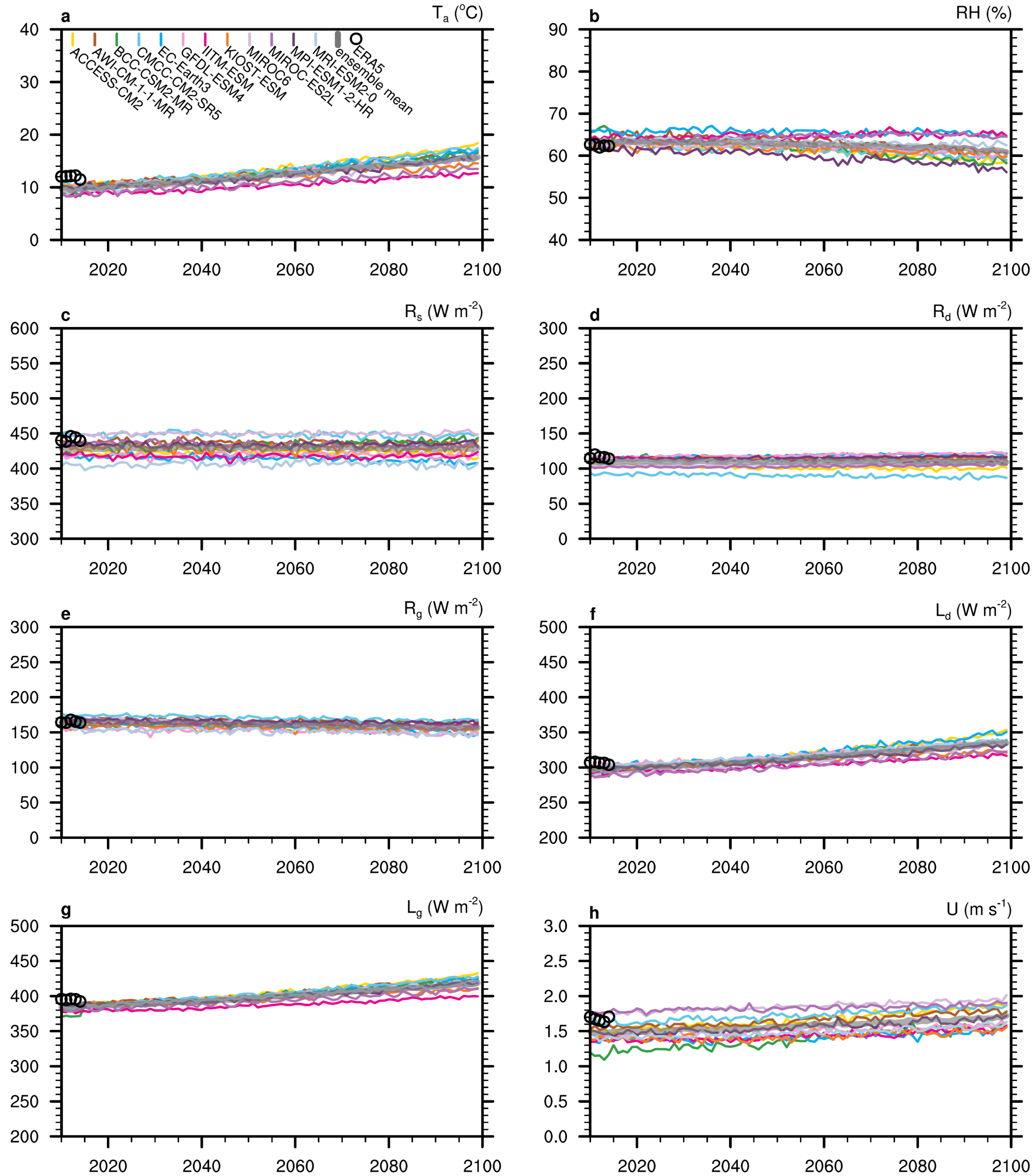

Supplementary Fig. 23: Same as Supplementary Fig. 19 but showing global land averages of daytime mean values of input variables concurrent with annual maximum G^{day} under the sun scenario. The thick grey line denotes the ensemble mean and the colour lines denote individual models. The black circles indicate the 2000-2014 averages of the ERA5 reanalysis data. Some spread among CMIP6 models and differences from ERA5 in these concurrent variables reflect the different dynamics and distributions in *G* determined by different inter-variable relationships of each model. The real inter-model spread of each input variable in the full period has been substantially reduced after bias and variance correction as shown in Supplementary Figs. 3-5 (both the climatological mean and interannual variance have been adjusted very closely to those of ERA5).

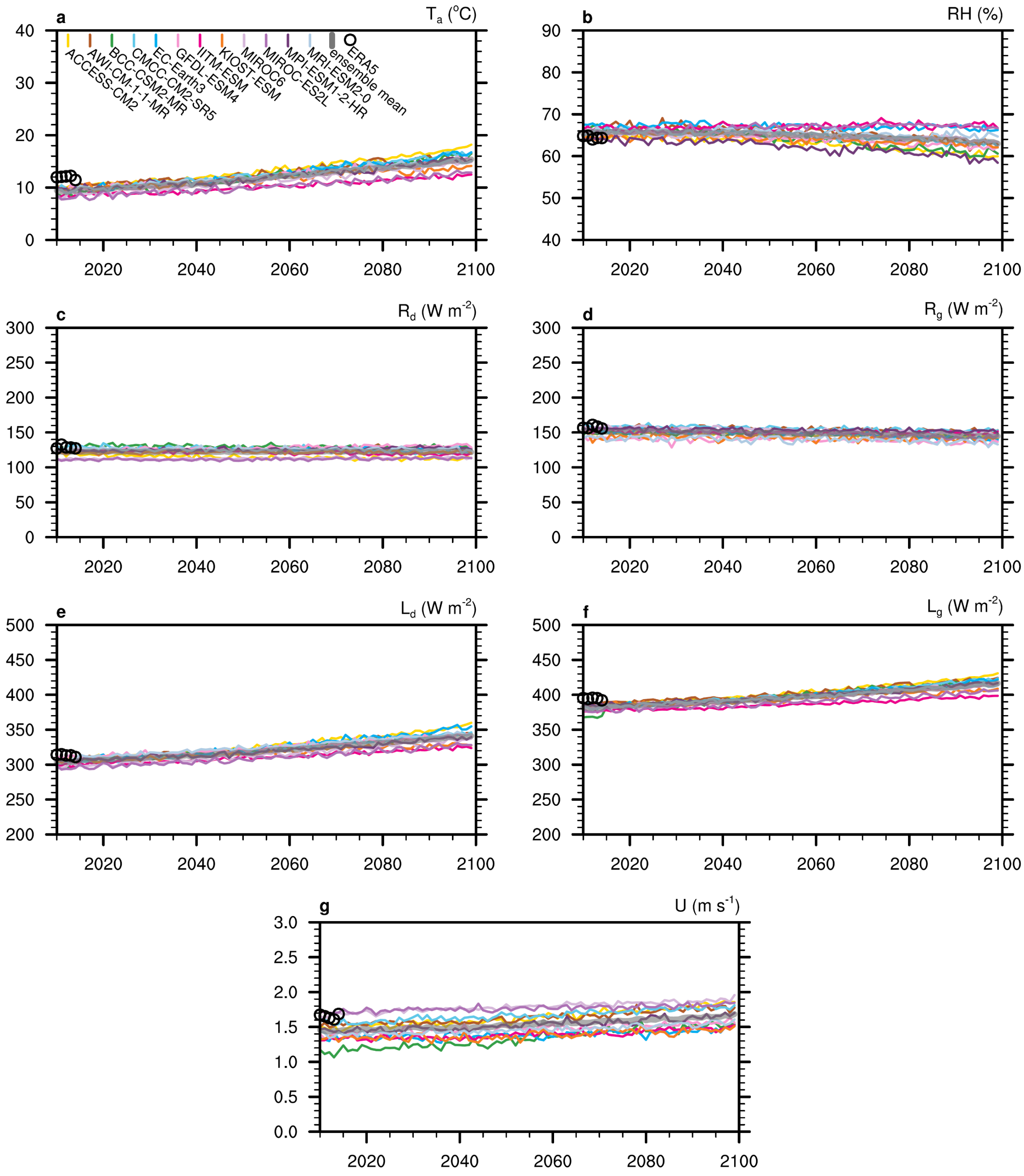

Supplementary Fig. 24: Same as Supplementary Fig. 23 but for the shade scenario, which uses only *R_d*, *R_g*, *L_d*, and *L_g* for radiation input.

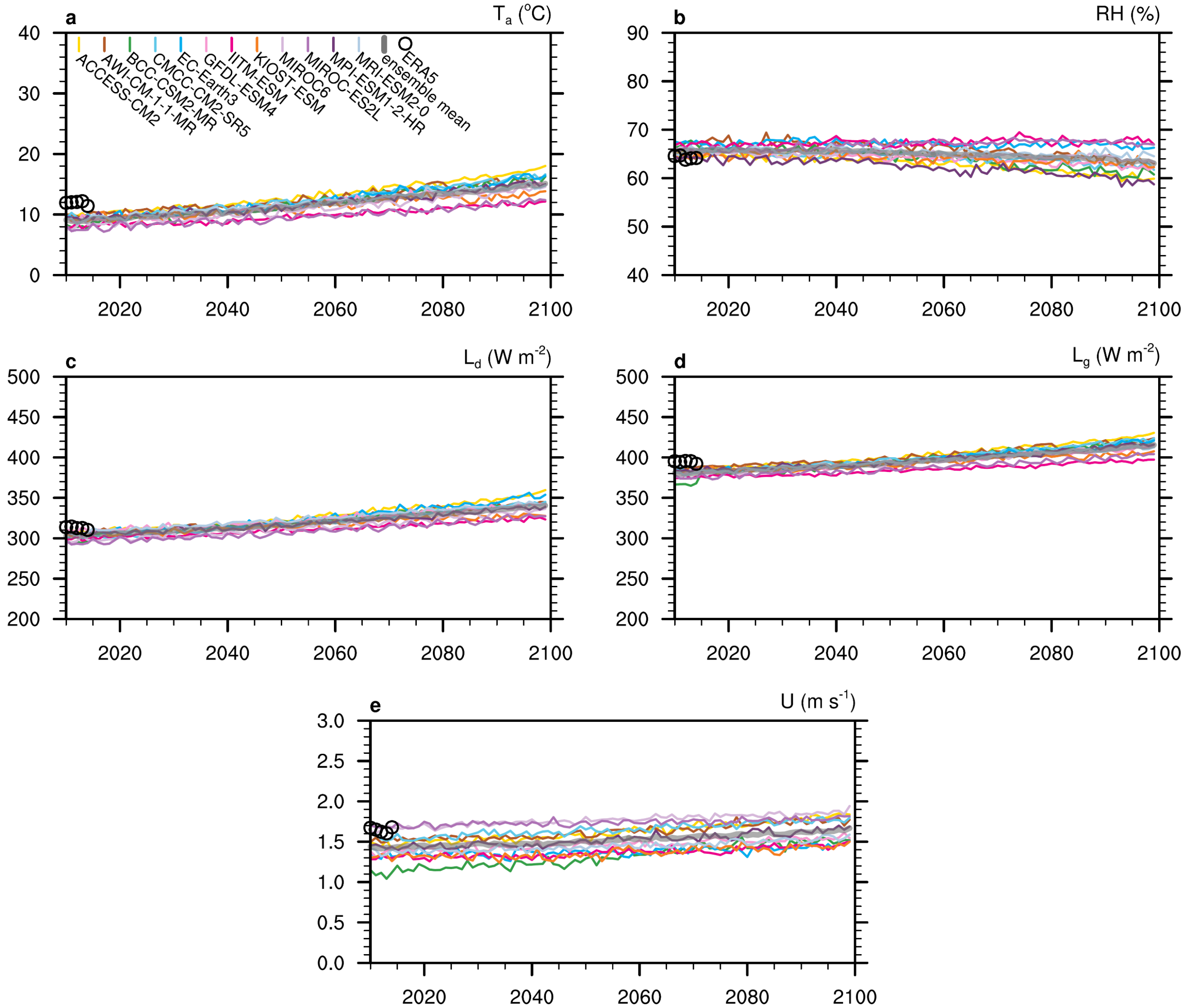

Supplementary Fig. 25: Same as Supplementary Fig. 23 but for the dark scenario, which uses only L_d and L_g for longwave radiation input.

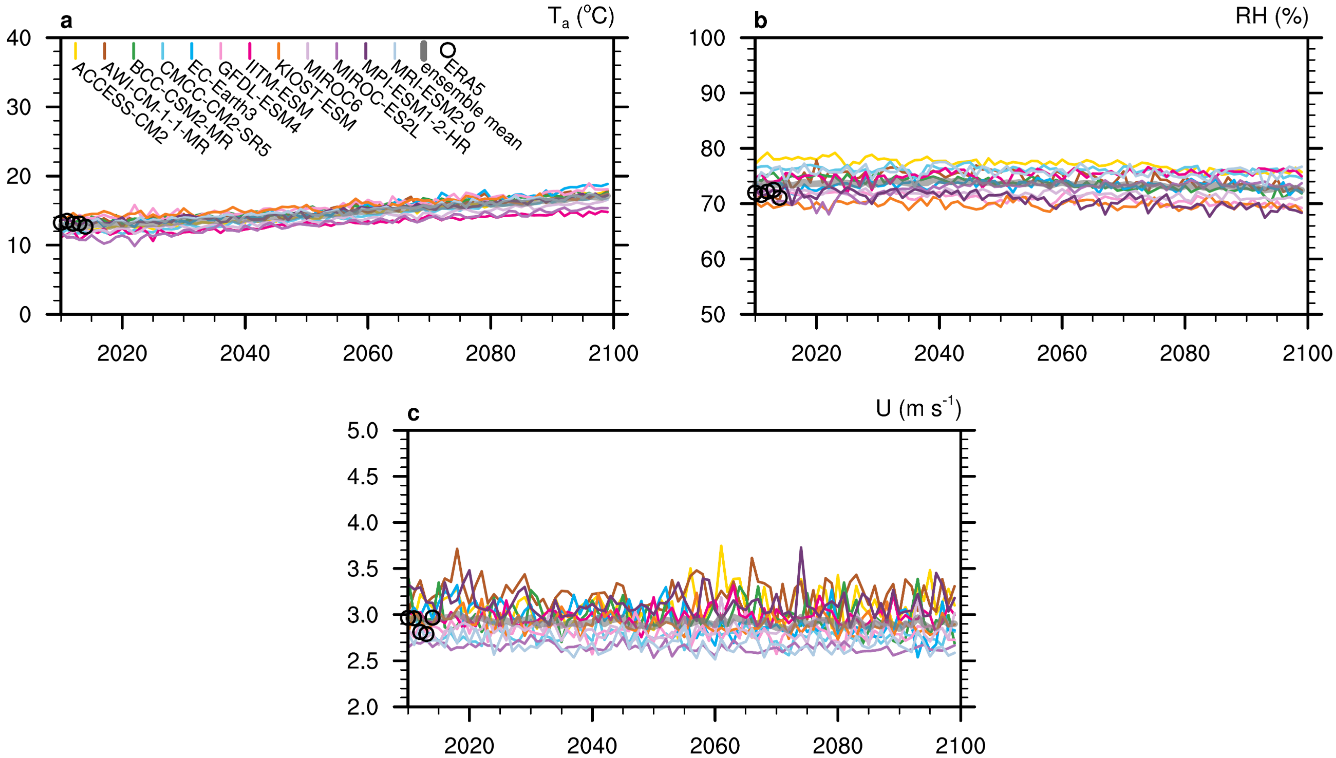

Supplementary Fig. 26: Same as Supplementary Fig. 23 but for the average values of input climate variables concurrent with annual maximum T_W^{day} of all land grid cells. Although only T_a (**a**) and RH (**b**) are involved in the calculation of T_W, U (**c**) is used in Eq. 14 to convert T_W^{day} to G_{TW}^{day}.

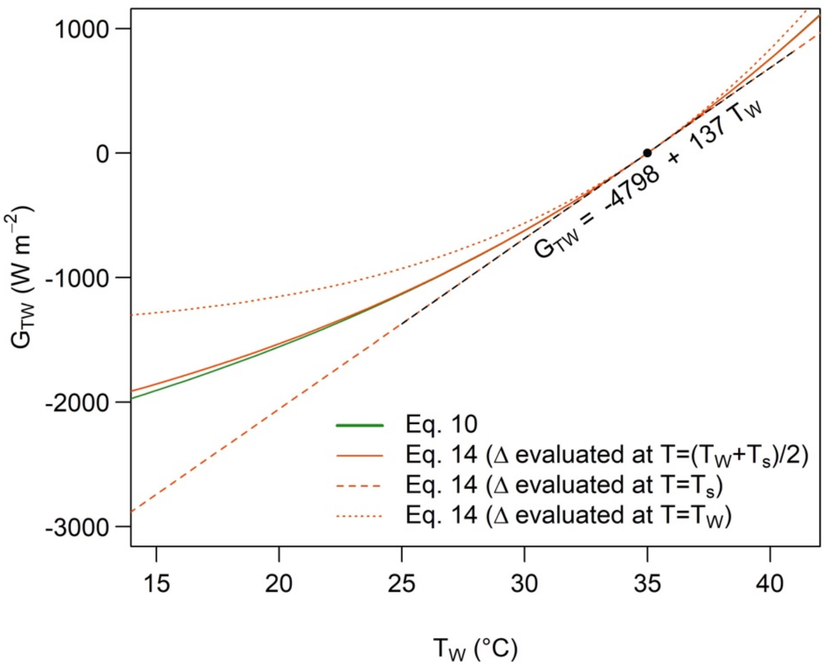

Supplementary Fig. 27: Conversion of T_W to effective energy flux G_{TW} by different functions (Eq. 10 or Eq. 14 in Methods). Eq. 14 is a linearization of Eq. 10 based on first-order Taylor approximations. The tangent line (dashed) at $T_W = 35$ °C shows the conversion rate of energy flux G_{TW} per unit increment of T_W around T_s. The slope 137 is the value of $-k = h_c(1 + \frac{\lambda}{c_p}\Delta)$ when Δ is evaluated at $T = T_W = T_s$ according to Eq. 14. When T_W departs from T_s, the conversion rate changes and there are three ways to estimate Δ for the coefficient k in Eq. 14. Evaluating Δ at $T = \frac{T_W + T_s}{2}$ yields more accurate k than evaluating Δ at either $T = T_s$ (underestimation) or $T = T_W$ (overestimation) with reference to Eq. 10. The ensemble mean wind speed $U = 3$ m s^{-1} of all land grid cells concurrent with T_W^{day} (Supplementary Fig. 26c) is used to calculate h_c in Eqs. 10 and 14.

Supplementary References

1. Di Napoli, C., Hogan, R. J. & Pappenberger, F. Mean radiant temperature from global-scale numerical weather prediction models. *Int J Biometeorol* **64**, 1233–1245 (2020).
2. Steadman, R. G. The Assessment of Sultriness. Part I: A Temperature-Humidity Index Based on Human Physiology and Clothing Science. *J. Appl. Meteor.* **18**, 861–873 (1979).
3. Cramer, M. N. & Jay, O. Partitional calorimetry. *Journal of Applied Physiology* **126**, 267–277 (2018).
4. Bonan, G. *Ecological Climatology: Concepts and Applications*. (Cambridge University Press, Cambridge, 2015). doi:10.1017/CBO9781107339200.
5. Bolton, D. The Computation of Equivalent Potential Temperature. *Monthly Weather Review* **108**, 1046–1053 (1980).
6. Schlatter, T. W. & Baker, D. V. *Algorithms for Thermodynamic Calculations*. 34 (1981).
7. Allen, R. G., Pereira, L. S., Raes, D. & Smith, M. *Crop Evapotranspiration-Guidelines for Computing Crop Water Requirements*. http://www.fao.org/3/x0490e/x0490e00.htm (1998).
8. Steadman, R. G. The Assessment of Sultriness. Part II: Effects of Wind, Extra Radiation and Barometric Pressure on Apparent Temperature. *J. Appl. Meteor.* **18**, 874–885 (1979).
9. Fiala, D., Lomas, K. J. & Stohrer, M. A computer model of human thermoregulation for a wide range of environmental conditions: the passive system. *J Appl Physiol (1985)* **87**, 1957–1972 (1999).
10. Fiala, D., Lomas, K. J. & Stohrer, M. Computer prediction of human thermoregulatory and temperature responses to a wide range of environmental conditions. *Int J Biometeorol* **45**, 143–159 (2001).
11. Cramer, M. N. & Jay, O. Biophysical aspects of human thermoregulation during heat stress. *Autonomic Neuroscience* **196**, 3–13 (2016).
12. Sherwood, S. C. & Huber, M. An adaptability limit to climate change due to heat stress. *Proceedings of the National Academy of Sciences* **107**, 9552–9555 (2010).

13. Kjellstrom, T., Lemke, B. & Otto, M. Mapping Occupational Heat Exposure and Effects in South-East Asia: Ongoing Time Trends 1980−2011 and Future Estimates to 2050. *Industrial Health* 12 (2013).

14. Parsons, K. C. International standards for the assessment of the risk of thermal strain on clothed workers in hot environments. *Ann Occup Hyg* **43**, 297–308 (1999).

15. ISO 7933. Ergonomics of the thermal environment — Analytical determination and interpretation of heat stress using calculation of the predicted heat strain. (2023).

16. Dix, M. *et al.* CSIRO-ARCCSS ACCESS-CM2 model output prepared for CMIP6 ScenarioMIP ssp585. Earth System Grid Federation https://doi.org/10.22033/ESGF/CMIP6.4332 (2019).

17. Semmler, T. *et al.* AWI AWI-CM1.1MR model output prepared for CMIP6 ScenarioMIP ssp585. Earth System Grid Federation https://doi.org/10.22033/ESGF/CMIP6.2817 (2019).

18. Xin, X. *et al.* BCC BCC-CSM2MR model output prepared for CMIP6 ScenarioMIP ssp585. Earth System Grid Federation https://doi.org/10.22033/ESGF/CMIP6.3050 (2019).

19. Lovato, T. & Peano, D. CMCC CMCC-CM2-SR5 model output prepared for CMIP6 ScenarioMIP ssp585. Earth System Grid Federation https://doi.org/10.22033/ESGF/CMIP6.3896 (2020).

20. Consortium (EC-Earth), E.-E. EC-Earth-Consortium EC-Earth3 model output prepared for CMIP6 ScenarioMIP ssp585. Earth System Grid Federation https://doi.org/10.22033/ESGF/CMIP6.4912 (2019).

21. John, J. G. *et al.* NOAA-GFDL GFDL-ESM4 model output prepared for CMIP6 ScenarioMIP ssp585. Earth System Grid Federation https://doi.org/10.22033/ESGF/CMIP6.8706 (2018).

22. Panickal, S. *et al.* CCCR-IITM IITM-ESM model output prepared for CMIP6 ScenarioMIP ssp585. Earth System Grid Federation https://doi.org/10.22033/ESGF/CMIP6.14753 (2020).

23. Kim, Y. *et al.* KIOST KIOST-ESM model output prepared for CMIP6 ScenarioMIP ssp585. Earth System Grid Federation https://doi.org/10.22033/ESGF/CMIP6.11249 (2019).

24. Shiogama, H., Abe, M. & Tatebe, H. MIROC MIROC6 model output prepared for CMIP6 ScenarioMIP ssp585. Earth System Grid Federation https://doi.org/10.22033/ESGF/CMIP6.5771 (2019).

25. Tachiiri, K. *et al.* MIROC MIROC-ES2L model output prepared for CMIP6 ScenarioMIP ssp585. Earth System Grid Federation https://doi.org/10.22033/ESGF/CMIP6.5770 (2019).

26. Wieners, K.-H. *et al.* MPI-M MPI-ESM1.2-LR model output prepared for CMIP6 ScenarioMIP ssp585. Earth System Grid Federation https://doi.org/10.22033/ESGF/CMIP6.6705 (2019).

27. Yukimoto, S. *et al.* MRI MRI-ESM2.0 model output prepared for CMIP6 ScenarioMIP ssp585. Earth System Grid Federation https://doi.org/10.22033/ESGF/CMIP6.6929 (2019).

28. Fiala, D., Havenith, G., Bröde, P., Kampmann, B. & Jendritzky, G. UTCI-Fiala multi-node model of human heat transfer and temperature regulation. *Int J Biometeorol* **56**, 429–441 (2012).

29. Erbs, D. G., Klein, S. A. & Duffie, J. A. Estimation of the diffuse radiation fraction for hourly, daily and monthly-average global radiation. *Solar Energy* **28**, 293–302 (1982).

30. Boland, J., Ridley, B. & Brown, B. Models of diffuse solar radiation. *Renewable Energy* **33**, 575–584 (2008).

31. Ridley, B., Boland, J. & Lauret, P. Modelling of diffuse solar fraction with multiple predictors. *Renewable Energy* **35**, 478–483 (2010).

32. Abreu, E. F. M., Canhoto, P. & Costa, M. J. Prediction of diffuse horizontal irradiance using a new climate zone model. *Renewable and Sustainable Energy Reviews* **110**, 28–42 (2019).

33. Yang, D. & Gueymard, C. A. Ensemble model output statistics for the separation of direct and diffuse components from 1-min global irradiance. *Solar Energy* **208**, 591–603 (2020).

34. Deshpande, A. *et al.* Mapping geographical inequalities in access to drinking water and sanitation facilities in low-income and middle-income countries, 2000–17. *The Lancet Global Health* **8**, e1162–e1185 (2020).

35. UNICEF, WHO. *Progress on Household Drinking Water, Sanitation and Hygiene 2000-2022: A Focus on Gender*. https://www.unicef.org/wca/media/9161/file/jmp-2023-wash-households-launch-version.pdf (2023).

36. European Commission. Joint Research Centre. *GHSL Data Package 2023*. (Publications Office of the European Union, LU, 2023).

37. Schiavina, M., Freire, S., Carioli, A. & MacManus, K. GHS-POP R2023A - GHS population grid multitemporal (1975-2030). (2023) doi:10.2905/2FF68A52-5B5B-4A22-8F40-C41DA8332CFE.

38. Schiavina, M., Melchiorri, M. & Pesaresi, M. GHS-SMOD R2023A - GHS settlement layers, application of the Degree of Urbanisation methodology (stage I) to GHS-POP R2023A and GHS-BUILT-S R2023A, multitemporal (1975-2030). (2023) doi:10.2905/A0DF7A6F-49DE-46EA-9BDE-563437A6E2BA.

39. Kjellstrom, T., Maître, N., Saget, C., Otto, M. & Karimova, T. *Working on a Warmer Planet: The Impact of Heat Stress on Labour Productivity and Decent Work*. (International Labour Organization, Geneva, Switzerland, 2019).

40. Ryder, G. & Director-General, I. World Employment and Social Outlook - Trends 2020. *World Employment and Social Outlook* (2020).

41. Cucchi, M. *et al.* WFDE5: bias-adjusted ERA5 reanalysis data for impact studies. *Earth System Science Data* **12**, 2097–2120 (2020).

42. Hoffmann, P., Katzfey, J. J., McGregor, J. L. & Thatcher, M. Bias and variance correction of sea surface temperatures used for dynamical downscaling. *J. Geophys. Res. Atmos.* **121**, 12,877-12,890 (2016).

43. Xu, Z., Han, Y., Tam, C.-Y., Yang, Z.-L. & Fu, C. Bias-corrected CMIP6 global dataset for dynamical downscaling of the historical and future climate (1979–2100). *Sci Data* **8**, 293 (2021).

44. Pal, J. S. & Eltahir, E. A. B. Future temperature in southwest Asia projected to exceed a threshold for human adaptability. *Nature Climate Change* **6**, 197–200 (2016).

45. Im, E.-S., Pal, J. S. & Eltahir, E. A. B. Deadly heat waves projected in the densely populated agricultural regions of South Asia. *Science Advances* **3**, e1603322 (2017).

46. de Dear, R. J., Arens, E., Hui, Z. & Oguro, M. Convective and radiative heat transfer coefficients for individual human body segments. *International Journal of Biometeorology* **40**, 141–156 (1997).

47. Kurazumi, Y. & Rezgals, L. Convective Heat Transfer Coefficients of the Human Body under Forced Convection from Ceiling. *J Ergonomics* **04**, (2014).

48. Nishi, Y. & Gagge, A. P. Direct evaluation of convective heat transfer coefficient by naphthalene sublimation. *Journal of Applied Physiology* **29**, 830–838 (1970).

49. Kurazumi, Y. *et al.* Radiative and convective heat transfer coefficients of the human body in natural convection. *Building and Environment* **43**, 2142–2153 (2008).

50. Gagge, A. P. & Nishi, Y. Heat Exchange Between Human Skin Surface and Thermal Environment. in *Comprehensive Physiology* 69–92 (American Cancer Society, 2011). doi:10.1002/cphy.cp090105.

51. Gagge, A. P., Stolwijk, J. A. J. & Hardy, J. D. Comfort and thermal sensations and associated physiological responses at various ambient temperatures. *Environmental Research* **1**, 1–20 (1967).

52. Kerslake, D. M. *The Stress of Hot Environments*. (CUP Archive, 1972).

53. Havenith, G. & Fiala, D. Thermal Indices and Thermophysiological Modeling for Heat Stress. in *Comprehensive Physiology* vol. 6 255–302 (John Wiley & Sons, Ltd, 2016).

54. Powis, C. M. *et al.* Observational and model evidence together support wide-spread exposure to noncompensable heat under continued global warming. *Science Advances* **9**, eadg9297 (2023).

55. Vecellio, D. J., Kong, Q., Kenney, W. L. & Huber, M. Greatly enhanced risk to humans as a consequence of empirically determined lower moist heat stress tolerance. *Proceedings of the National Academy of Sciences* **120**, e2305427120 (2023).

56. Guzman-Echavarria, G., Middel, A. & Vanos, J. Beyond heat exposure — new methods to quantify and link personal heat exposure, stress, and strain in diverse populations and climates: The journal Temperature toolbox. *Temperature* **10**, 358–378 (2023).

57. Vanos, J. *et al.* A physiological approach for assessing human survivability and liveability to heat in a changing climate. *Nat Commun* **14**, 1–14 (2023).